Geometric Distortion Correction in EPI at Ultra High Field

Dissertation

zur Erlangung des akademischen Grades

doctor rerum naturalium
(Dr. rer. nat.)

genehmigt durch die Fakultät für Naturwissenschaften
der Otto-von-Guericke-Universität Magdeburg

von **M. Eng. Myung-Ho In**

geb. am 26.08.1979 in Dangjin, Republic of Korea

Gutachter: **Prof. Dr. rer. nat. habil. Oliver Speck**

Gutachter: **Prof. Dr. phil. nat. habil. Stefan Posse**

eingereicht am: 12.01.2012

verteidigt am: 30.05.2012

To my parents, my wife (Hyemi), and my son (Sunghwan)

TABLE OF CONTENTS

ABSTRACT

Because of its high imaging efficiency, single-shot echo-planar imaging (EPI) has become a well established, unique technique that is used in various brain imaging applications such as functional MRI (fMRI) and diffusion tensor imaging (DTI). EPI, however, is very sensitive to inhomogeneities induced by the main magnetic field, as well as differences in the magnetic susceptibility of an object, leading to distortions in the image geometry and signal intensity. Since field inhomogeneities are directly proportional to the strength of the main magnetic field, the distortions are increased at high field strength of 3T, and become a significant obstacle for EPI-based applications at conditions of ultra high field (UHF) such as 7T and above.

The main objective of this study was to develop an optimal EPI distortion correction scheme with high robustness and fidelity, especially for UHF. Many approaches based on shift maps have been developed to date, in attempts to correct for geometric distortions in EPI. They can be categorized into shift maps in distorted and non-distorted phase-encoding coordinates. Since different sequences are generally used for determining the two types of shift maps, reliable comparisons of the measurement parameters are not easily reconciled. In order to evaluate the correction quality of geometric distortions in EPI, especially at UHF, shift maps within the same conditions are required, if a fair comparison study is to be achieved. The findings reported in this thesis indicate that both shift maps can be determined from 3D PSF data obtained by means of a point-spread-function (PSF) mapping method. In recognizing the limitations of a shift map-based correction through a comparison study, an improved PSF mapping-based distortion correction scheme was developed and is presented. This includes higher correction fidelity as well as highly accelerated PSF acquisition without any loss of quality compared to full PSF acquisition. All the development and evaluations were performed in phantoms and in *in vivo* measurements at 7T. The results show that the proposed method corrects for geometric distortions in EPI with a very high degree of accuracy and quality despite the very high PSF acceleration. Therefore, it can be concluded that it would be suitable to support advanced EPI-based application studies, especially at UHF.

ZUSAMMENFASSUNG

Single-Shot Echo-Planar Bildgebung (EPI) ist aufgrund seiner hohen Zeiteffizienz eine weit verbreitete Technik in der Magnetresonzbildgebung und wird für viele verschiedene Anwendungen, wie etwa funktionelle MRT (fMRT) und Diffusions-Tensor Bildgebung (DTI) genutzt. EPI ist jedoch sehr empfindlich für Inhomogenitäten des Magnetfeldes durch Unterschiede der magnetischen Eigenschaften (Suszeptibilität) innerhalb des Untersuchungsobjektes, was zu starken geometrischen Verzerrungen und Schwankungen in der Signalintensität der Abbildung führt. Die Feldstörungen sind proportional zur Stärke des Hauptmagnetfeldes, weshalb sich geometrische Verzerrungen bei hohen Feldstärken, wie etwa 3T, vergrößern und zur echten Herausforderung bei höchsten Feldstärken (UHF), wie etwa 7T und mehr, werden.

Das Hauptziel dieser Arbeit ist die Entwicklung einer optimierten, robusten und exakten Verzerrungskorrektur von EPI-Daten für UHF. Viele Methoden zur Verzerrungskorrektur von EPI-Daten basieren heutzutage auf so genannten Shift Maps. Diese kann man in zwei Kategorien einteilen, welche in unverzerrten oder in verzerrten Koordinaten in Phasenkodierrichtung dargestellt werden. Da für beide Typen in der Regel verschiedene Aufnahmeverfahren verwendet werden, ist es schwierig, diese anhand ihrer Messparameter zu vergleichen. Um die Qualität der Verzerrungskorrektur von EPI-Daten beider Verfahren zu erfassen und um einen quantitativen Vergleich zu ermöglichen, müssen die Shift-Maps mit gleichen Konditionen aufgenommen werden. In dieser Promotionsarbeit wird aufgezeigt, dass die Berechnung beider Shift-Map-Typen aus einem einzigen 3D Point-Spread-Function (PSF) Datensatz vorgenommen werden kann. Außerdem wird eine neue, verbesserte PSF-basierte Korrekturmethode zur Verzerrungskorrektur vorgestellt. Diese Methode erlaubt einerseits eine höhere Korrekturqualität und andererseits eine hohe beschleunigte PSF Akquisition ohne Qualitätsverlust gegenüber der unbeschleunigten PSF-Variante.

Alle entwickelten Methoden wurden mit Phantom- und in-vivo-Messungen in einem 7T Scanner getestet und evaluiert. Die Ergebnisse zeigen, dass die vorgestellte Methode zur geometrischen Verzerrungskorrektur von EPI Daten mit einer hohen Genauigkeit und Qualität, trotz hoher PSF-Beschleunigung durchgeführt werden kann. Dies wird zukünftige

EPI-basierte Projekte und Studien erheblich unterstützen.

LIST OF ABBREVIATIONS

Meaning	Abbreviation
Blood Oxygenation Level Dependent	BOLD
Diffusion Tensor Imaging	DTI
Diffusion Weight Imaging	DWI
Echo Time	TE
Echo-Planar Imaging	EPI
Field of View	FOV
Functional MRI	fMRI
Gradient Echo	GE
GeneRalized Autocalibrating Partially Parallel Acquisitions	GRAPPA
Institutional Review Board	IRB
Imaging FOV in the PSF dimension	PSF-FOV
Non-Uniform Fast Fourier Transform	NUFFT
Magnetic Resonance Imaging	MRI
Magnetic Resonance	MR
Point Spread Function	PSF
Perfusion MRI	pMRI
PSF mapped in the EPI phase-encoding coordinate	EPI-PSF
Repetition Time	TR
Radio Frequency	RF
Reduced Field of View	rFOV
Specific Absorption Rate	SAR
Signal to Noise Ratio	SNR
Standard Deviation	StdDev
Ultra High Field	UHF

1

INTRODUCTION

1.1 Motivation

The use of magnetic resonance imaging (MRI) has grown dramatically over the past few decades and has resulted in an extraordinary opportunity to look into the human body *in vivo*. A number of MRI applications for diagnostic and research purposes have been actively conducted in a wide spectrum of fields. At the same time, magnetic resonance (MR) devices at ultra high field (UHF) such as 7T and above are being continuously developed, in attempts to improve the sensitivity of MRI signal detection at higher magnetic field strengths. As shown in the example in Fig. 1, a comparison study has shown that significantly increased activations can be identified with a high resolution activation map at 7T compared to 3T and opens the possibility for developing a better understanding of brain functions [1]. Thus, more advanced applications promise to contribute to the ongoing attempts to further develop and employ human MR scanners at UHF. However, the applications have faced a number of problems such as increased tissue-specific absorption rates (SAR), inhomogeneity of the main magnetic field, and susceptibility-induced magnetic field variations within a region of interest. In particular the last issue has become a significant obstacle to the success of echo-planar imaging (EPI) application studies. Although increased field strength leads to higher signal-to-noise ratio (SNR), which can be translated into a higher image resolution and sensitivity, correspondingly

increased distortions result in a degraded image quality.

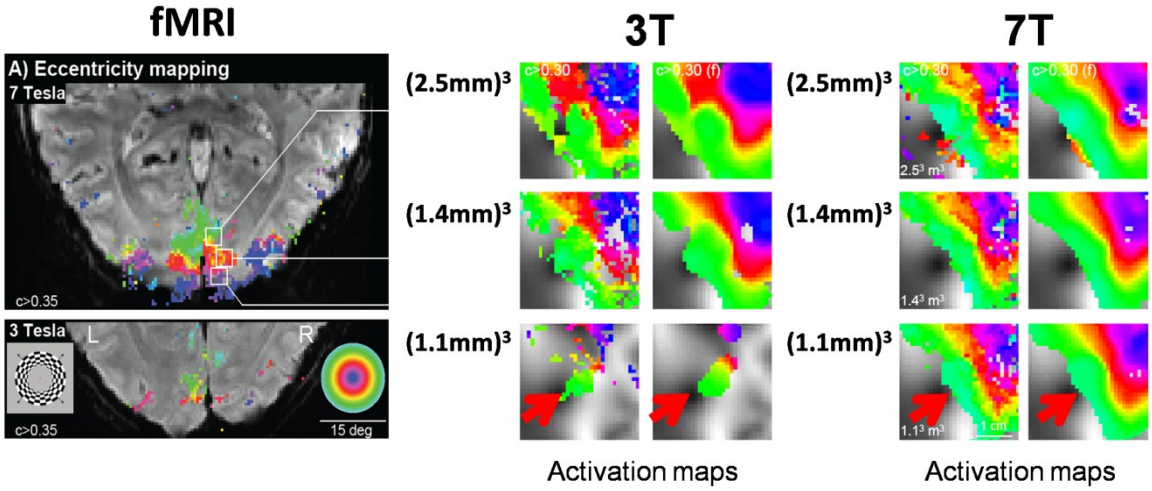

Figure 1: Potential advantage at UHF [1]. Significantly increased activations are identified with a high resolution activation map ($1.1mm^3$) in a retinotopic mapping experiment at 7T compared to 3T.

Single-shot EPI [2] allows the rapid acquisition of a two-dimensional (2D) image after a single radiofrequency (RF) excitation. Due to the high temporal resolution of EPI, it has been widely adapted for use in various applications of brain function mapping such as functional MRI (fMRI), perfusion MRI (pMRI) or diffusion tensor imaging (DTI). However, EPI is very sensitive to inhomogeneities induced by the main magnetic field as well as magnetic susceptibility differences within the regions of interest near tissue/bone or tissue/air interfaces for *in vivo* human imaging, which lead to distortions in image geometry and signal intensity (see Fig. 2). The distortions can be somewhat deceased using thinner slice acquisition [3], compensation gradients in combination with optimized slice orientation [4], and multi-channel coils with parallel imaging techniques [5-7]. An example of reducing distortions using a parallel imaging technique is shown in Fig. 3. However, there still exist distortions that need to be solved, especially for UHF such as 7T, where an additional procedure for the correction is generally required.

Currently, only static shim routines, which correct for overall field inhomogeneity, have been implemented into routine scanners. Shimming procedures typically require time in the order of 5-50 seconds, depending on the level of sophistication and are applied at the beginning of each examination [8-11]. The B_0 field distribution is then corrected using

available shim coils. This, however, eliminates only gross inhomogeneities, leaving remaining local field deviations practically unaffected.

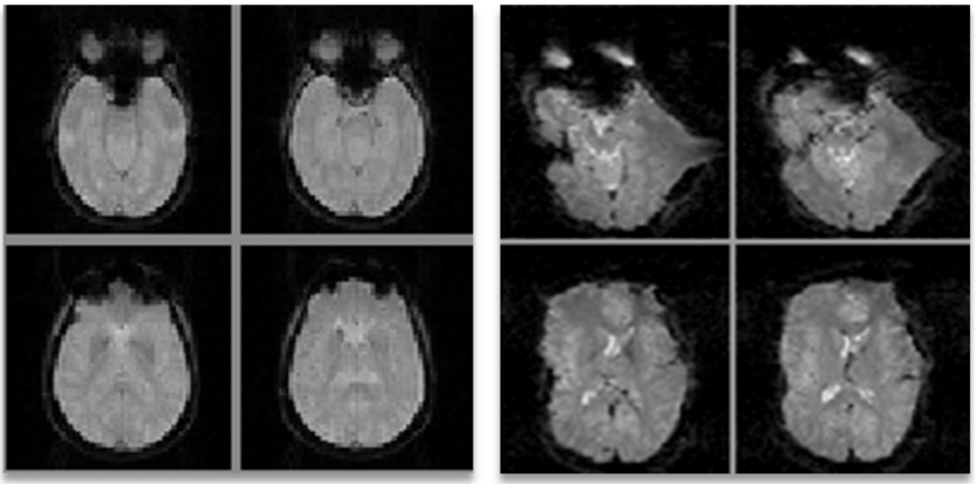

Figure 2: Geometric distortions in EPI at 1.5 (left) and 7T (right) [12].

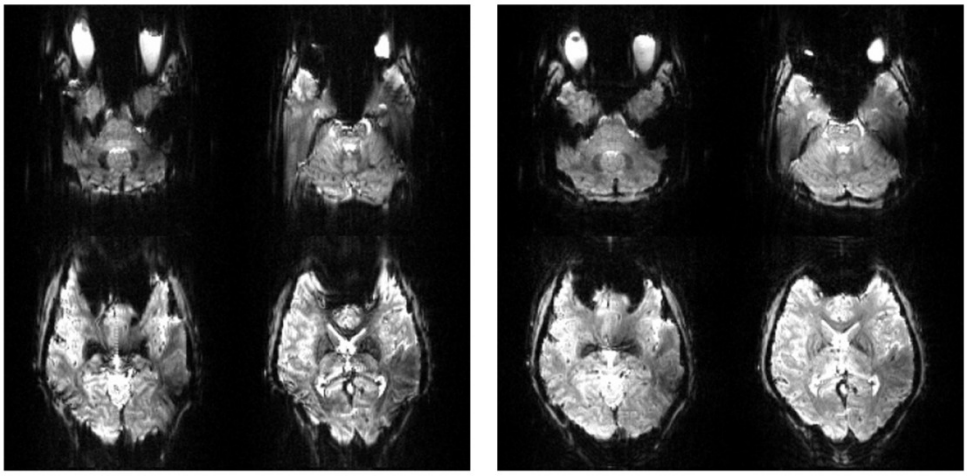

Figure 3: Geometric distortions can be reduced using a parallel imaging technique: (left) without acceleration and (right) with acceleration factor of 2 [12].

Many methods have shown that geometric distortions can be corrected by field maps determined in non-distorted [13] or distorted [14-16] phase-encoding coordinates. With different echo time (TE) offsets [13,15,16] or k_y-offsets [14,17], the phase differences between two or more reference images allow such field maps to be determined. After variations in the magnetic field are measured, these are transferred into local pixel shifts of

the image in order to correct distortions. However, such methods require a phase unwrapping process and are difficult to apply at object boundaries, for large field inhomogeneities, or for disconnected object regions.

Alternatively, multi-reference scan methods [18-21] have been proposed to avoid phase wraps in field maps. Using additional scan information, these approaches measure distortions arising from different off-resonance factors including chemical shifts, RF frequency offsets, and eddy currents effects. With the measured field maps, distortion correction is performed on magnitude data using interpolation methods [13,15-17] or on complex data using Fourier methods [14,18-21]. Compared to single-reference methods, better correction quality and more stable performance is achieved by multi-reference approaches due to the increased information concerning distortions. However, a major shortcoming of these techniques is a prolonged acquisition time. In the case of a matrix size of $Nx \times Ny$, Ny repetitions are required and this results in acquisition times ranging from 3 to nearly 10 minutes for typical applications, which appear to be exceedingly large if a separate reference scan is required for each acquisition. Nonetheless, in a number of applications a time overhead of several minutes is perfectly acceptable, e.g. in fMRI where the reference scan is only to be acquired once before the entire examination.

The point-spread-function (PSF) mapping method [22-28] has been adapted more recently to improve the robustness and quality of distortion correction. In this method, three-dimensional (3D) PSF data encode the phase-encoding direction of an object slice twice, once by EPI phase-encoding and once by spin-warp phase-encoding prior to the readout gradient. A 3D Fourier transformation generates the local PSF in the phase-encoding direction for each voxel. The PSFs are shifted along the distorted coordinates (corresponding to EPI phase-encoding) due to the field inhomogeneity and the deviations are commonly processed in the non-distorted coordinates (corresponding to spin-warp phase-encoding) [22-28]. Compared to the field map method, the PSF approach is unaffected by several factors including phase wraps, partial volume effects, and eddy current errors and can provide a more effective solution to the problems of distortions in EPI [23].

Although the PSF method is well-established to correct distortions at higher field strength such as 3T, it is difficult to reliably correct much stronger distortions at ultra high field (UHF) such as 7T. In general, strong local susceptibility effects in local areas resulting in

severe image stretching and compression lead to local broadening and distortions of the PSF peak itself, and it is often difficult to determine the shift (distortion) value of the distorted PSF peak accurately in such areas. Therefore, an accurate determination of the distortion should be carefully considered since it is the key for the successful application of distortion correction in EPI, especially for UHF.

1.2 Organization of the Thesis

The main aim of this thesis was to develop an optimal scheme for correcting geometric distortions in EPI, especially at UHF such as 7T. In this thesis, a comparison study was initially performed using the shift maps in non-distorted and distorted coordinates. In order to evaluate accuracy, the distortion corrected results are compared at 7T. It is demonstrated that the modified PSF approach allows a shift map in the distorted coordinate instead of a shift map in the non-distorted coordinate [22-28] as the original PSF method and a fair comparison is possible when both shift maps within identical conditions are used. In addition, a phase fitting method is newly adapted in the proposed shift map calculation scheme in order to determine the PSF peak more accurately. Based on the comparison study, a further improved PSF mapping scheme is presented to allow for optimal correction fidelity for geometric distortions in EPI at UHF.

The basic theory of two dimensional (2D) imaging is presented in Chapter 2.1. The general principles of the acquisition properties of conventional gradient-echo (GE) and gradient-echo EPI imaging are introduced. Distortions arising from field inhomogeneity are explained to provide an understanding of geometric distortions in GE and EPI. Based on this theory, three correction methods, the field map method, the reversed gradient method, and the PSF mapping method, are further introduced to explain how to measure and correct geometric distortions in EPI.

As described in Chapter 3, an EPI-based shift map calculated from 3D PSF data is newly suggested to accurately determine strong distortions in EPI at UHF such as 7T. An evaluation study was accomplished in a phantom and *in vivo* in the human brain through a fair comparison of correction performance using both shift maps in the distorted and non-distorted phase-encoding coordinates which are newly proposed and originally used to

correct for distortions, respectively. This research was supported by The Korean Ministry of Education, Science and Technology (MOEST) with grant numbers M10530010001-08N3001-00110 and M10862020005-08N6202-005100. Parts of the study were also supported by the BMBF funded via the INUMAC project (01EQ0603).

Chapter 4 introduces an optimal PSF mapping-based distortion correction method which allows higher correction fidelity and highly accelerated PSF acquisition. For a high quality correction, the measured PSF-based correction kernel is used as a convolution kernel for distortion correction. In addition, a non-equidistant sampling scheme is proposed to highly accelerate PSF acquisition without loss of correction quality. The distinct advantages of the proposed approach have been demonstrated in phantom and human *in vivo* experiments at 7T. This work was performed at Otto-von-Guericke-University Magdeburg and supported by a grant from NIDA (1R01DA021146) and DFG (SP632/3).

Finally, the above-mentioned works are summarized and recommendations made for future studies in Chapter 5.

2

BACKGROUND

This section briefly introduces conventional 2D MR imaging with the terminology of *k*-space introduced by Ljunggren [29]. Conventional GE and EPI imaging are introduced and the special features of geometric distortions in both methods are discussed based on imaging theory when field inhomogeneities exist. The findings indicate that it is reasonable to consider EPI distortions only in the phase-encoding direction and to neglect distortions in the readout direction. In order to correct for distortion, three methods for geometric distortion correction in EPI, the field map method, the reversed gradient polarity method, and the PSF mapping method are introduced and further discussed in detail.

2.1 2D Imaging, *k*-Space, and Geometric Distortion

2.1.1 Conventional GE imaging

Conventional 2D MR imaging is based on a 2D Fourier transform (FT) and the components of k_x, and k_y, are given by [29-33].

$$k_x(t) = \gamma \int_0^t G_x(t')\,dt' \tag{2.1}$$

and

$$k_y(t) = \gamma \int_0^t G_y(t')\,dt' \tag{2.2}$$

where γ is the gyromagnetic ratio (2.68×10^8 rad $s^{-1}T^{-1}$ for proton), and $G_x(t)$ and $G_y(t)$ describe the time varying gradient fields in the x and y direction, corresponding to readout (RO) and phase-encoding (PE) direction, respectively.

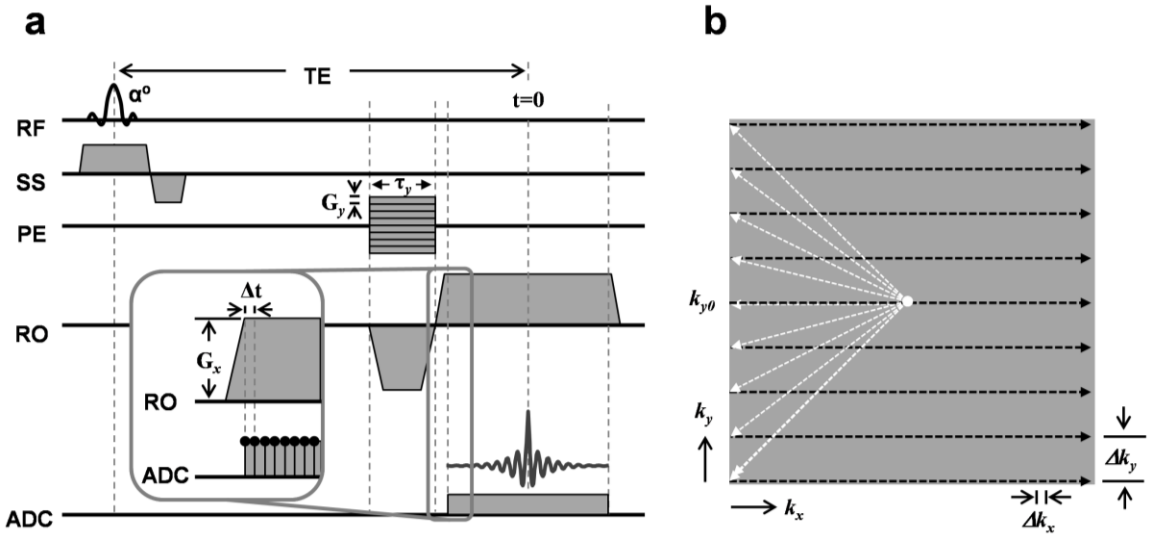

Figure 4: Conventional GE sequence diagram (a) and *k*-space (b)

As shown in Fig. 4a, the time t can be written as

$$t = TE \pm m\Delta t \tag{2.3}$$

where TE is the echo time, m is the m^{th} reading point in the x direction, and Δt is the dwell time, corresponding to the time between two adjacent samples in an analog-to-digital

converter (ADC) (see Fig. 4a). In GE imaging, radio frequency (RF) excitation is repeated after the repetition time (TR) to fill each *k*-space line. The amplitude of the phase-encoding gradient is uniformly increased to fill the second *k*-space line with an equidistant stepping along the phase-encoding direction. These repetitions are required until an n^{th} PE-gradient amplitude is reached and followed by acquisition of the n^{th} *k*-space line (see Fig. 4b). For the gradient and timing parameters defined in Eqs. 2.2 and 2.3 and Fig. 4a, the acquired signal $S(m\Delta k_x, n\Delta k_y)$ in GE imaging in the presence of magnetic field inhomogeneities can be expressed as

$$\begin{aligned} S(m\Delta k_x, n\Delta k_y) = \int_x \int_y \rho(x,y) \exp[i\gamma \Delta B(x,y)(TE \pm m\Delta t)] \\ \cdot \exp[i(m\Delta k_x x + n\Delta k_y y)] dxdy \end{aligned} \tag{2.4}$$

$$-N_x/2 \le m < N_x/2, \quad -N_y/2 \le n < N_y/2$$

where $k_x = m\Delta k_x$, $k_y = n\Delta k_y$, $\Delta B(x,y)$ is the filed inhomogeneity at the given position (x and y), N_x and N_y are the total number of points in the x and y direction, and Δk_x and Δk_y are a gradient increment in the x and y direction, respectively. In order to simplify the equation, an ideal slice-selective excitation oriented along the slice-selection (SS) gradient was assumed and the relaxation parameters such as the spin-lattice relaxation time (T1) and the spin-spin relaxation time (T2) were not explicitly considered in this equation. In *k*-space, the increment steps are defined as below:

$$\Delta k_x = \frac{2\pi}{FOV_x} = \gamma G_x \Delta t \tag{2.5}$$

and

$$\Delta k_y = \frac{2\pi}{FOV_y} = \gamma G_y \tau_y \tag{2.6}$$

where G_x is the amplitude of the readout gradient, G_y is the amplitude of the phase-encoding gradient increment, of duration τ_y. Using Eqs. 2.5 and 2.6, Eq 2.4 can be

expressed in terms of the signal at discrete times as

$$S(m\Delta k_x, n\Delta k_y) = \int_x \int_y \rho(x,y) \exp[i\gamma \Delta B(x,y) TE] \cdot \exp\left\{ i\left[m\Delta k_x (x \pm \frac{\Delta B(x,y)}{G_x}) + n\Delta k_y y \right] \right\} dxdy \tag{2.7}$$

or at continuous times as

$$S(k_x, k_y) = \int_x \int_y \rho(x,y) \exp[i\gamma \Delta B(x,y) TE] \exp\left\{ i\left[k_x (x \pm \frac{\Delta B(x,y)}{G_x}) + k_y y \right] \right\} dxdy \tag{2.8}$$

Now, we define a coordinate transformation operator [34]:

$$x_1 = x \pm \frac{\Delta B(x,y)}{G_x} = R[x] \tag{2.9}$$

where $R[x]$ is the operator that transforms from the non-distorted coordinate (x) to the distorted coordinate (x_1). If it is assumed that $R[x]$ increases or decreases monotonically in the x direction, the operator is invertible:

$$x = R^{-1}[x_1] \tag{2.10}$$

This assumption is met when the local field inhomogeneity $\Delta B(x,y)$ is smaller than the readout gradient strength G_x. When there exist the field inhomogeneities, these effects are accumulated along the readout direction during the acquisition time of each echo signal after every RF excitation and don't affect the acquisition of next k-space line, as shown in Fig. 4.

Thus it is reasonable to assume that the variables x and y are independent and the derivative of Eq. 2.9 is

$$dx_1 = (1 \pm \frac{\Delta B'(x)}{G_x})dx \tag{2.11}$$

Substituting x_1 for x and using Eqs. 2.9-11, we can rewrite the Eq. 2.8 as:

$$S(k_x, k_y) = \int_{x_1}\int_{y}\left[(1 \pm \frac{\Delta B'(R^{-1}[x_1])}{G_x})^{-1}\rho(R^{-1}[x_1], y)\exp[i\gamma\Delta B(R^{-1}[x_1], y)TE]\right] \cdot \exp\{i[k_x x_1 + k_y y]\}dx_1 dy \tag{2.12}$$

After 2D inverse Fourier transform of $S(k_x, k_y)$ in k_x and k_y, the measured GE image density $I_{GE}(x, y)$ is (substituting y with y'):

$$\begin{aligned} I_{GE}(x, y) &= \int_{k_x}\int_{k_y} S(k_x, k_y)\exp[-i(k_x x + k_y y)]dk_x dk_y \\ &= \int_{x_1}\int_{y'}\left\{\left[1 \pm \frac{\Delta B'(R^{-1}[x_1])}{G_x}\right]^{-1}\rho(R^{-1}[x_1], y')\exp[i\gamma\Delta B(R^{-1}[x_1], y')TE]\right\} \\ &\cdot \int_{k_x}\exp[ik_x(x_1 - x)]\int_{k_y}\exp[-ik_y(y' - y)]dx_1 dy' dk_x dk_y \\ &= \left[1 \pm \frac{\Delta B'(R^{-1}[x])}{G_x}\right]^{-1}\rho(R^{-1}[x], y)\exp[i\gamma\Delta B(R^{-1}[x], y)TE] \end{aligned} \tag{2.13}$$

$$I_{GE}(x, y) = \left[1 \pm \frac{\Delta B'(x_1)}{G_x}\right]^{-1}\rho(x_1, y)\exp[i\gamma\Delta B(x_1, y)TE] \tag{2.14}$$

The equation 2.14 demonstrates that the measured GE image is distorted only in the x direction (corresponding to the readout direction) due to field inhomogeneity. The distortion in the x direction includes both a geometric distortion (see Eq. 2.9) and an intensity distortion $[1 \pm \Delta B'(x_1)/G_x]^{-1}$ as shown in Eq. 2.14. Thus, the distortions arising from the field inhomogeneity appear not in the phase-encoding direction, but only in the readout direction of GE image. As shown in Eq. 2.9, the strength of the distortions is dependent on the field inhomogeneity terms and the amplitude of the readout gradient. In general, field inhomogeneity is proportional to the field strength and the distortions are

increased at higher field strength such as 7T and above. The effects are decreased only when a higher amplitude of the readout gradient is selected as the imaging parameter (e.g. to decrease TE or accelerate the imaging speed).

2.1.2 Gradient-echo EPI imaging

In contrast to the collection strategy of the single *k*-space line used in GE sequence, the conventional gradient-echo EPI sequence [2,35,36] acquires all lines of 2D *k*-space in a continuous trajectory after a single RF excitation (see Fig. 5). For the EPI imaging time, Eq. 2.3 can be rewritten as [18,21,23]

$$t = TE + nT \pm m\Delta t \tag{2.15}$$

where T is the time interval between adjacent k_y-lines, which is referred to as echo spacing (ES) time. Therefore, the acquired signal $S(m\Delta k_x, n\Delta k_y)$ in Eq. 2.4 can be rewritten as

$$\begin{aligned} &S(m\Delta k_x, n\Delta k_y) \\ &= \int_x \int_y \rho(x,y)\exp[i\gamma\Delta B(x,y)(TE + nT \pm m\Delta t)]\exp[i(m\Delta k_x x + n\Delta k_y y)]\,dxdy \end{aligned} \tag{2.16}$$

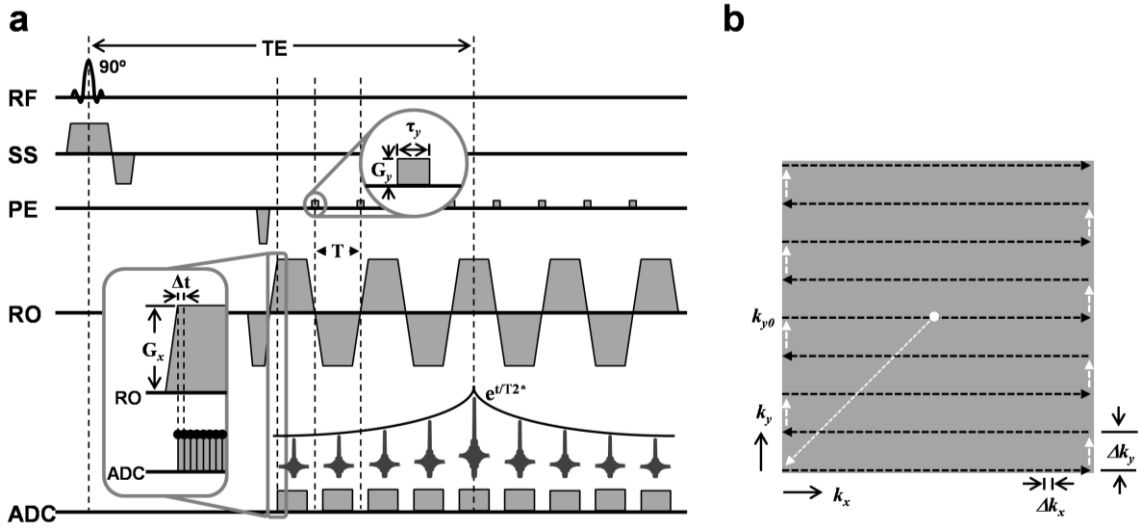

Figure 5: Conventional gradient-echo EPI sequence diagram (a) and *k*-space (b)

In EPI imaging, very high amplitude of the gradient G_x, which leads to a very high pixel bandwidth in the readout direction, is usually required to accelerate the imaging speed of the EPI acquisition. Thus, the distortion term $\Delta B(x,y)/G_x$ in the readout direction is relatively small in the case of EPI imaging. For example, if a readout bandwidth of 1000 (Hz/px) is used for EPI acquisition, the maximum strength of the distortion is 1/4 pixel shift when a maximum off-resonance frequency of 250 (Hz) appears within the imaging slice. Since the maximum geometric distortion in the readout direction is much less than 1 pixel, the distortions in the readout direction are negligible. In the following, we assume that there is no geometric distortion in the readout direction. Using the same spatial frequencies associated with the *x* and *y* directions in Eqs. 2.5 and 2.6, the measured signal in Eq. 2.16 can be simplified as:

$$S(m\Delta k_x, n\Delta k_y) = \int_x \int_y \rho(x,y)\exp[i\gamma\Delta B(x,y)TE] \cdot \exp\left\{i\left[m\Delta k_x x + n\Delta k_y\left(y + \frac{\Delta B(x,y)T}{G_y\tau_y}\right)\right]\right\}dxdy \tag{2.17}$$

or

$$S(k_x, k_y) = \int_x \int_y \rho(x,y)\exp[i\gamma\Delta B(x,y)TE]\exp\left\{i\left[k_x x + k_y\left(y + \frac{\Delta B(x,y)T}{G_y\tau_y}\right)\right]\right\}dxdy \tag{2.18}$$

In the same way as Eqs. 2.9-11, we can define as

$$y_1 = y + \frac{\Delta B(x,y)T}{G_y\tau_y} = R[y] \tag{2.19}$$

$$y = R^{-1}[y_1] \tag{2.20}$$

$$dy_1 = \left(1 + \frac{\Delta B'(y)T}{G_y\tau_y}\right)dy \tag{2.21}$$

Therefore, we can substitute Eq. 2.18 with y_1 as

$$S(k_x,k_y)=\int_x\int_{y_1}\left[(1+\frac{\Delta B'(R^{-1}[y_1])T}{G_y\tau_y})^{-1}\rho(x,R^{-1}[y_1])\exp[i\gamma\Delta B(x,R^{-1}[y_1])TE]\right] \cdot\exp\{i[k_x x+k_y y_1]\}dxdy_1 \tag{2.22}$$

After 2D inverse Fourier transform of $S(k_x,k_y)$, the measured EPI image density $I_{EPI}(x,y)$ is obtained (substituting x with x'):

$$\begin{aligned} I_{EPI}(x,y)&=\int_{k_x}\int_{k_y}S(k_x,k_y)\exp[-i(k_x x+k_y y)]dk_x dk_y \\ &=\int_{x'}\int_{y_1}\left\{\left[1+\frac{\Delta B'(R^{-1}[y_1])T}{G_y\tau_y}\right]^{-1}\rho(x',R^{-1}[y_1])\exp[i\gamma\Delta B(x',R^{-1}[y_1])TE]\right\} \\ &\cdot\int_{k_x}\exp[ik_x(x'-x)]\int_{k_y}\exp[-ik_y(y_1-y)]dx'dy_1dk_xdk_y \\ &=\left[1+\frac{\Delta B'(R^{-1}[y])T}{G_y\tau_y}\right]^{-1}\rho(x,R^{-1}[y])\exp[i\gamma\Delta B(x,R^{-1}[y])TE] \end{aligned} \tag{2.23}$$

$$I_{EPI}(x,y)=\left[1+\frac{\Delta B'(y_1)T}{G_y\tau_y}\right]^{-1}\rho(x,y_1)\exp[i\gamma\Delta B(x,y_1)TE] \tag{2.24}$$

In contrast to the GE image, the effects of field inhomogeneity accumulate during the acquisition of all lines of 2D *k*-space in EPI imaging and the measured EPI image becomes severely distorted in the phase-encoding direction. Since $\tau_y \ll$ T and the phase-encoding gradient blip G_y is usually small, as shown in Eq. 2.19, the term of geometric distortions is not negligible in the EPI phase-encoding direction. If an echo-spacing time of 0.8 (ms) and a matrix size of 160 in the phase-encoding direction are selected as the EPI acquisition parameters, large amounts of distortions occurred with up to 32 pixel shifts in the phase-encoding direction in the case of a maximum off-resonance frequency of 250 (Hz). In other words, severe geometric distortions, which are very relevant, are observed in the phase-encoding direction of EPI. Therefore, in the following studies described herein, EPI geometric distortions are considered only in the phase-encoding direction.

2.2 Geometric Distortion Correction in EPI

In this section, three methods for correcting for distortion, namely the field map method, the reversed polarity method, and the PSF mapping-based method, are introduced to provide a better understanding of how to calculate the shift (or distortion) maps in non-distorted and distorted phase-encoding coordinates and how to apply these maps to the correction of geometric distortions in EPI.

2.2.1 Field map method

As shown in Eqs. 2.14 and 2.24, the phase of the reconstructed image includes the field inhomogeneity term and can be used for calculating and correcting the geometric distortions in EPI. The distortion correction method based on the field map is typically referred to as the field map method [13-16]. Interestingly, information concerning geometric distortions caused by the field inhomogeneity is represented differently in the reconstructed images according to the acquisition strategy. The field inhomogeneity term in the non-distorted and distorted phase-encoding coordinate is obtained from GE and EPI images, respectively. Therefore, two different types of field maps can be determined from the two images and can be applied for distortion correction in EPI.

2.2.1.1 Field map in the non-distorted phase-encoding coordinate

As shown in Eq. 2.14, the accumulated phase of a GE image is represented by the multiplication of the gyromagnetic ratio, the local field inhomogeneity given in the x and y position, and the echo time. In terms of off-resonance frequency, it can be expressed as [37].

$$\begin{aligned}\varphi_{TE}(x,y) &= \gamma\Delta B(x,y)TE \\ &= 2\pi\omega_f(x,y)TE\end{aligned} \tag{2.25}$$

where $\varphi_{\mathrm{TE}}(x,y)$ is the phase at TE and $\omega_f(x,y)$ is the precession frequency shift. The off-

resonance frequency can be translated into a pixel shift value by dividing a pixel bandwidth value along the phase-encoding direction in EPI. The relation is

$$\Delta(x,y) = \omega_f(x,y) N_y T \tag{2.26}$$

Therefore, the final pixel shift map (or displacement map) can be obtained by the calculation shown below [38]:

$$\begin{aligned} \Delta(x,y) &= \frac{\varphi_{TE}(x,y) N_y T}{2\pi TE} \\ &= \frac{\gamma \Delta B(x,y) T}{\Delta k_y} \end{aligned} \tag{2.27}$$

where $\varphi_{\mathrm{TE}}(x,y)$ and TE are the values from the measured GE image, and N_y and T are the parameters of the distorted EPI image to be corrected. If a very high readout bandwidth is used in the GE imaging as in EPI imaging, we can assume a distortion free GE image in both the readout and phase-encoding directions. In this case, the field map obtained from the non-distorted GE image can be referred to as the field map in non-distorted coordinates (or space), especially in the phase-encoding coordinate. The location of a pixel in the geometrically distorted (EPI) phase-encoding coordinate (y_1) is related to the position of the pixel in the non-distorted (GE) phase-encoding coordinate (y) by the formula below

$$I(x,y_1) = I(x, y + \Delta(x,y)) \tag{2.28}$$

This equation shows that the shift map in the non-distorted coordinate $\Delta(x,y)$ includes a distortion term, which acts as a convolution product to generate geometric distortions in EPI. Thus, an appropriate deconvolution procedure is required to apply this map to the correction of geometric distortions in EPI. However, caution is needed here, due to the shift map obtained by the use of a different sequence. If the measurement parameters of a GE image, such as matrix size and FOV, are not matched with the EPI image, an additional postprocessing step should be considered to account for these parameter differences.

2.2.1.2 Field map in the distorted phase-encoding coordinate

In EPI imaging, severe geometric distortions usually appear along the phase-encoding coordinates due to the low effective bandwidth. Thus, the field map obtained from the EPI image is usually called the field map in the distorted phase-encoding coordinates (or space). Therefore, the final pixel shift map is obtained by

$$\begin{aligned}\Delta(x, y_1) &= \frac{\varphi_{TE}(x, y_1) N_y T}{2\pi TE} \\ &= \frac{\gamma \Delta B(x, y_1) T}{\Delta k_y}\end{aligned} \tag{2.29}$$

where all parameters from the distorted EPI image to be corrected are used. In this shift map, the relation of a pixel location in the phase-encoding direction between the geometrically distorted (EPI) image (y_1) and the distortion corrected image (y') is then

$$I(x, y') = I(x, y_1 - \Delta(x, y_1)) \tag{2.30}$$

In contrast to the shift map in the non-distorted coordinates $\Delta(x, y)$, the distortion term in the shift map in the distorted coordinate $\Delta(x, y_1)$ acts as a convolution product to correct geometric distortions in EPI. Thus, it is possible to correct geometric distortions in EPI directly using the shift map in the distorted coordinates.

2.2.1.3 Unwrapping process with multi-reference images

The findings here indicate that two different types of field maps can be obtained from GE or EPI images and be used to correct geometric distortions in EPI. In general, however, the phase image is wrapped when the phase accumulation is more than 2-pi and phase evolution over a long echo time produces severe phase wrap artifacts in the field maps, in particular near the interfaces of structures where strong susceptibility effects appear, as shown in Figs. 6c and 6d. To avoid these problems, two or several phase images with different TE offset [13,15,16] or k_y-offsets [14,17] are usually measured. If two phase images with different TEs, TE_1 and TE_2, are used to calculate a pixel shift (or displacement)

map, Eqs. 2.27 and 2.29 can be expressed as

$$\Delta(x,y) = \frac{\varphi_{TE_1}(x,y) - \varphi_{TE_2}(x,y)}{2\pi(TE_1 - TE_2)} N_y T = \frac{\Delta\varphi_{TE}(x,y) N_y T}{2\pi\Delta TE} \tag{2.31}$$

and

$$\Delta(x,y_1) = \frac{\Delta\varphi_{TE}(x,y_1) N_y T}{2\pi\Delta TE} \tag{2.32}$$

where ΔTE is the time difference between TE_1 and TE_2, $\Delta\varphi_{TE}(x,y)$ and $\Delta\varphi_{TE}(x,y_1)$ are the phase accumulation during the time of ΔTE in the non-distorted and distorted coordinate, respectively. The above equations assume that phase accumulation increases linearly over time. Since phase evolution over a short period of ΔTE is usually small, phase wrap artifacts in the shift map can be avoided by the calculation in Eqs. 2.31 and 2.32. However, since the phase image is very sensitive to noise, the errors are large in areas with a low SNR. The errors in the field map are translated into the shift map for distortion correction and directly produce errors in the distortion corrected image. In addition, few studies [23,39] have demonstrated that the phase does not evolve linearly with time, especially at the regions with strong field inhomogeneity and susceptibility effects. As an alternative to avoid the above problems, the PSF mapping method [22-27] as a multi-reference technique based on additional k_y-offsets has been proposed more recently.

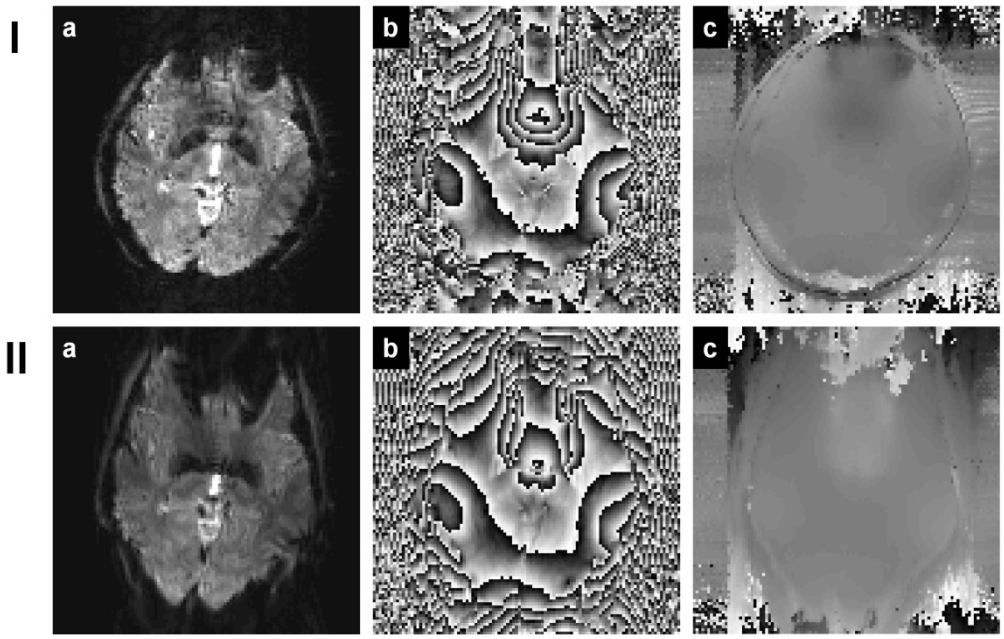

Figure 6: The field maps obtained from GE (I) and EPI (II) images are shown: the magnitude (a), phase (b), and phase unwrapped images (c)

2.2.2 The reversed gradient method

The reversed gradient method relies on the fact that if a second acquisition is performed under exactly the same conditions (except that the polarity of the gradient is reversed), the spatial shifting of signal in the second image will occur in the opposite direction along the corresponding coordinate [40]. Since it is generally considered that spatial distortion in the readout direction (x) is likely negligible in EPI acquisition, the reversed phase-encoding gradient is used for correction of EPI geometric distortions in the phase-encoding direction (y). If Eq. 2.30 represents the relation in the first image, the relation between the spatially corrected (y') and shifted coordinate (y_2) in the second image is then

$$I(x, y') = I(x, y_2 + \Delta(x, y_2)) \tag{2.33}$$

Therefore, it is clear that the geometrically corrected coordinate (y') can be calculated by combining Eqs. 2.30 and 2.33

$$I(x,y') = \frac{I(x,y_1) + I(x,y_2)}{2} \tag{2.34}$$

Since two images $I(x,y_1)$ and $I(x,y_2)$ have been acquired with the reversed phase-encoding gradients, these distorted images are related to the corrected image $I(x,y')$ by the expressions [40-42]

$$I(x,y') = I(x,y_1)\frac{dy_1}{dy'} \tag{2.35}$$

and

$$I(x,y') = I(x,y_2)\frac{dy_2}{dy'} \tag{2.36}$$

Combining Eqs. 2.35 and 2.36 and integrating from y_{10} to y_1 and y_{20} to y_2 (substituting y_1 and y_2 with y'_1 and y'_2) leads to the equation:

$$\int_{y_{10}}^{y_1} I(x,y'_1)dy'_1 = \int_{y_{20}}^{y_2} I(x,y'_2)dy'_2 \tag{2.37}$$

where a given initial pair of y_{10} and y_{20} is a suitable boundary condition in the two images to satisfy the above equation. Therefore, the corresponding points y_1 and y_2 can be found by calculating line integrals of the two images in the phase-encoding direction [42]. Although a distortion corrected image can be generated using either Eq. 2.35 or 2.36, a differentiation of Eq. 2.34 with respect to y' and substitution from Eqs. 2.35 and 2.36 allows the simplified equation below

$$I(x,y') = 2 \times \frac{I(x,y_1) \times I(x,y_2)}{I(x,y_1) + I(x,y_2)}. \tag{2.38}$$

Therefore, this equation can be used for accurately correcting geometric distortions in EPI. Although spatial information in strongly compressed regions has already been lost in the acquisition process, this method, which combines two images with reversed phase-encoding directions leading to opposite image distortions, potentially allows the loss of spatial resolution to be overcome, due to such compression. However, an accurate and robust masking process is usually required in order to avoid integrating background noise from outside of the object and a blurring effect in the distortion corrected image would be introduced by Eq. 2.38, since the calculation is based on intensities arising from two different anatomical positions. In addition, a loss of temporal resolution would be expected if this method were to be applied to correcting EPI geometric distortions in fMRI experiments, since a pair of two images with reversed phase-encoding gradients should be measured during the scan time. Thus, this approach is becoming more useful in clinical settings such as DTI applications rather than fMRI applications.

2.2.3 PSF mapping method

The basic theory of the PSF mapping-based distortion correction method [22-27] is introduced and discussed in more detail in this section. In the following, we assume that the effects of inhomogeneities in the readout direction are negligible with respect to geometric distortions in EPI, as shown in the section on EPI imaging. In the PSF mapping method, we also assume TE=0 since the reconstructed magnitude data is usually considered in the subsequent analysis. Therefore, the acquired signal in Eq. 2.18 for a standard EPI acquisition including inhomogeneity effects can be rewritten as:

$$S(k_x,k_y) = \int_x \int_y \rho(x,y) \exp\left\{ i\left[k_x x + k_y (y + \frac{\gamma \Delta B(x,y) T}{\Delta k_y}) \right] \right\} dxdy \tag{2.39}$$

An additional phase-encoding direction is added by the spin-warp phase-encoding

gradients, which is identical to conventional GE [43] as shown in the section on GE imaging, in order to obtain reference data for the correction of a distorted EPI image. The spin-warp phase-encoding coordinate of the conventional GE image is free from inhomogeneity effects as shown in Eq. 2.14 and thus, it could be considered as the non-distorted phase-encoding coordinate.

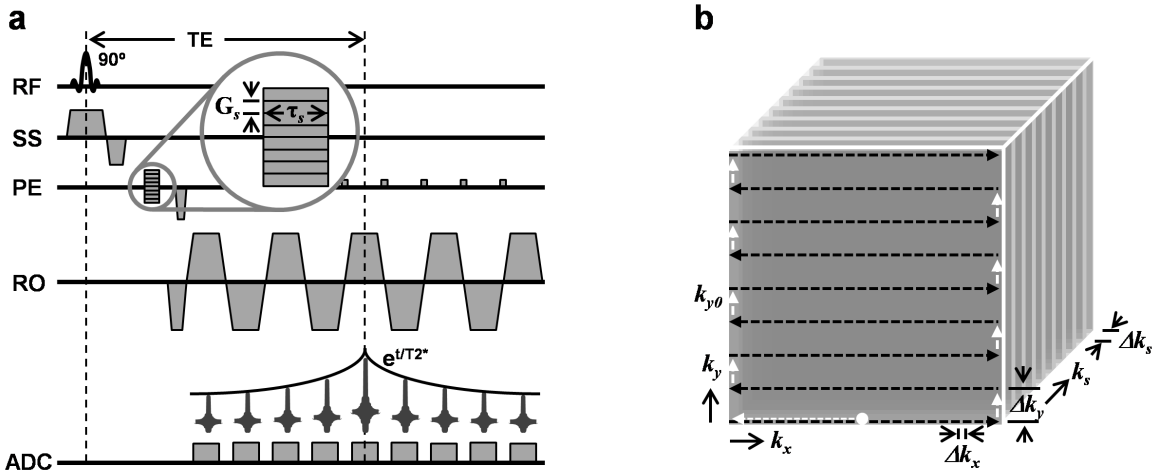

Figure 7: PSF mapping sequence diagram (a) and the corresponding 3D *k*-space (b).

The PSF mapping sequence is shown in Fig. 7a. Before the start of the echo train of the standard (product) EPI readout, the additional conventional gradient echo type phase-encoding gradients are added to fill the k_s-dimension, which result in 3D *k*-space data for each slice (see Fig. 7b). To keep an identical minimum echo time with the conventional EPI sequence, this additional phase-encoding gradient G_s can be combined with the EPI prephasing gradient. Since the same spatial information is encoded by two phase-encoding gradients, EPI and spin-warp phase-encoding gradients, these are linked with each other in the reconstructed 3D data and can be referred to as the distorted (EPI, *y*-coordinate) and the non-distorted spin-warp (GE, *s*-coordinate) phase-encoding coordinate, which correspond to the k_y and k_s dimension of the 3D *k*-space data set, respectively.

If the parameter for the PSF dimension is termed k_s, then the acquired signal becomes:

$$S(k_x,k_y,k_s)=\int_x\int_y \rho(x,y)\,\exp\left\{i\left[k_x x+k_s y+k_y\left(y+\frac{\gamma\Delta B(x,y)T}{\Delta k_y}\right)\right]\right\}dxdy \qquad (2.40)$$

where k_s is the k-space coordinate encoded by the spin-warp phase-encoding gradients. The increment step of the spin-warp phase-encoding gradient is defined as below (see Fig. 7a):

$$\Delta k_s = \frac{2\pi}{FOV_y} = \gamma G_s \tau_s \tag{2.41}$$

where τ_s is the time duration of the additional spin-warp phase-encoding gradient. In order to encode identical space with the same number of phase-encoding steps as in EPI imaging, the amount of the one increment step in k_s should be same as in k_y. To simplify the analysis, we assume that the total encoding step for the additional k_s-dimension is equal to the imaging dimension (k_y) although a larger or smaller step than the imaging resolution can be used. A 3D inverse Fourier transformation of the 3D k-space data in k_x, k_y, and k_s results in a image domain 3D data, which can be written as (substituting x and y with x' and y'):

$$\begin{aligned} & I(x,y,s) \\ & = \Im^{-3}[S(k_x,k_y,k_s)] \\ & = \int_{x'}\int_{y'} \rho(x',y') \int_{k_y} \exp\left\{ i\left[k_y (y' - y + \frac{\gamma \Delta B(x',y')T}{\Delta k_y} \right] \right\} \\ & \quad \cdot \int_{k_x} \exp[ik_x(x'-x)] \int_{k_s} \exp[ik_s(y'-s)] dk_s dk_x dk_y dx' dy' \end{aligned} \tag{2.42}$$

where $\Im^{-3}$ is the 3D inverse Fourier transform. The integration over above variables leads to:

$$I(x,y,s) = \rho(x,s) \int_{k_y} \exp\left\{ i\left[k_y (s - y + \frac{\gamma \Delta B(x,s)T}{\Delta k_y} \right] \right\} dk_y \tag{2.43}$$

In the reconstructed 3D image, the proton density $\rho(x,s)$ is multiplied with the PSF as the distortion term, which can now be defined as:

$$H(x,y,s) = \int_{k_y} \exp\left\{ i \left[k_y (s - y + \frac{\gamma \Delta B(x,s) T}{\Delta k_y} \right] \right\} dk_y \tag{2.44}$$

Under the condition that the field inhomogeneity is time-invariant during the acquisition, this equation can be further reduced to:

$$\begin{aligned} H(x,y,s) &= \delta(s + \Delta(x,s) - y) \\ \Delta(x,s) &= \frac{\gamma \Delta B(x,s) T}{\Delta k_y}. \end{aligned} \tag{2.45}$$

The more simplified form of the PSF is shown in Eq. 2.45. It demonstrates that the shift in PSF can be represented as a single delta function using the delta approximation to sample at the grid points given by the respective Cartesian coordinate system and thus, the magnitude PSF data can be considered in the subsequent analysis. The shifts are caused only along the *y*-direction in the *s*-cooridnates, integration of the 3D PSF image $I(x,y,s)$ along the distorted (y) and non-distorted phase-encoding direction (s) yields the non-distorted $I(x,s)$ and distorted image $I(x,y)$, respectively (see Fig. 8).

$$\begin{aligned} I(x,s) &= \int I(x,y,s) dy \\ &= \int \rho(x,s) H(x,y,s) dy \\ &= \rho(x,s) \int H(x,y,s) dy \\ &= \rho(x,s) \end{aligned} \tag{2.46}$$

$$\begin{aligned} I(x,y) &= \int I(x,y,s) ds \\ &= \int \rho(x,s) H(x,y,s) ds \\ &= \int \rho(x,s) \delta(s + \Delta(x,s) - y) ds \end{aligned} \tag{2.47}$$

This non-distorted image $I(x,s)$ has an identical echo time and thus, image contrast as the corresponding EPI image $I(x,y)$ and may be used to verify the quality of the correction or serve as a reference for amplitude correction [25]. A convolution of the proton density with the PSF results in geometric distortions in EPI as shown in Eq. 2.47 and PSF peak mapping

(along the distorted EPI phase-encoding coordinate y) in the non-distorted spin-warp phase-encoding coordinate (s) allows a shift map $\Delta(x,s)$ in the non-distorted coordinate (s). Interestingly, this determined shift map in the non-distorted phase-encoding coordinate corresponds to the shift map in the field map method, as shown in Eq. 2.27. However, the PSF mapping method usually allows a shift map with higher SNR due to its multi-shot nature. In addition, compared to the field map method that uses a different sequence to measure the field inhomogeneity term, an identical field inhomogeneity term, which acts as a convolution product to generate EPI distortions, can be measured by the PSF mapping method since the PSF mapping sequence is based on the conventional EPI sequence. Therefore, the PSF mapping method potentially measures a more accurate distortion term for EPI distortion correction, which leads to better correction quality.

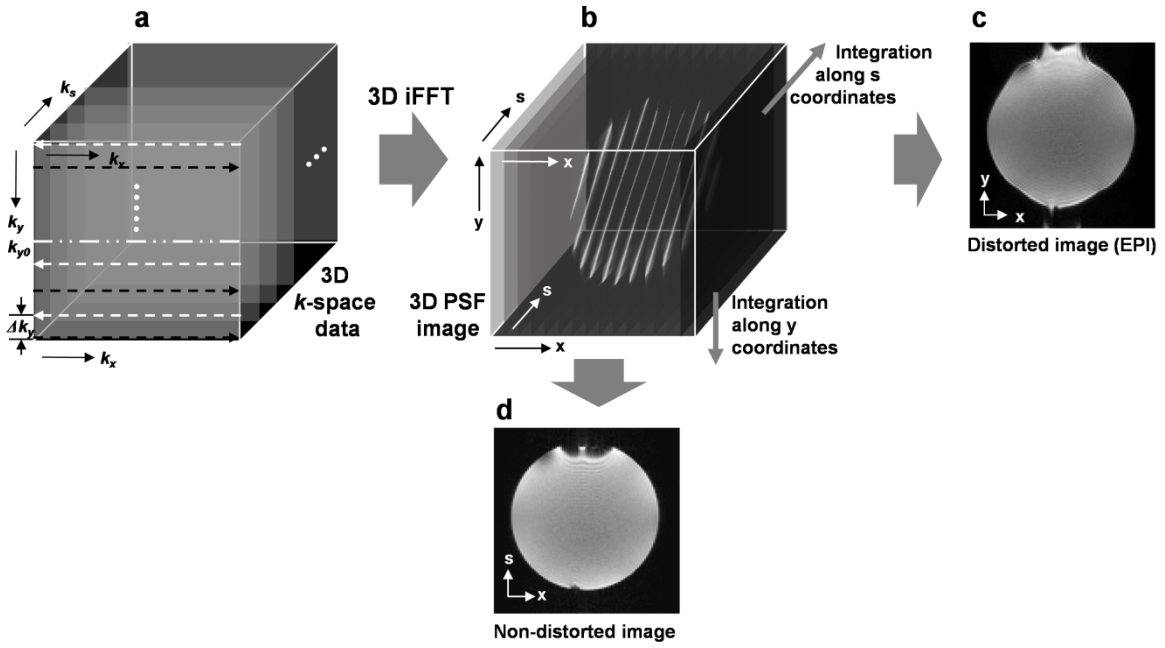

Figure 8: the property of the 3D k-space data set obtained by the PSF mapping sequence. After 3D inverse FFT of 3D k-space data set (a), a 3D PSF data set (b) is obtained and the distorted (c) and non-distorted (d) images can be calculated by integration of the 3D PSF data set along the s and y coordinates, respectively.

3

SHIFT MAPS IN NON-DISTORTED AND DISTORTED COORDINATES

To date, distortion correction performance has not been clearly compared with the shift maps in the non-distorted and distorted phase-encoding coordinates, although many studies [13,15,22,24-28,44,45] have shown that geometric distortions in EPI could be effectively corrected using either shift maps in non-distorted or distorted coordinates. This can be attributed to the fact that it is not possible to determine the shift maps in the non-distorted and distorted coordinates easily under the same conditions, since different types of sequences are generally required to measure a GE or EPI image, which leads to different distortion properties in the reconstructed images as explained in the previous chapter. In this chapter, we demonstrate that a modified PSF mapping method can permit shift maps in the distorted coordinate to be obtained, instead of a shift map in the non-distorted coordinate, as shown in the original method [22-27]. Thus, a fair comparison between the shift maps in the non-distorted and distorted coordinate can be achieved using the modified and original PSF mapping method. The distortion corrected results demonstrate that the modified PSF mapping method can be used to correct strong EPI distortions more accurately than in the original method, especially at UHF such as 7T.

3.1 Preface

In the field map method, the term for field inhomogeneity is calculated from the phase of the reconstructed image and transformed into a pixel shift map (or displacement map) in order to correct for geometric distortions in EPI. It is possible to calculate two different types of shift maps in non-distorted and distorted phase-encoding coordinates from the GE and EPI images, respectively. Although a previous study [39] demonstrated the correction difference and quality using shift maps in the non-distorted and distorted coordinates at 3T, it has not yet been fully evaluated at UHF where strong geometric distortions are seen in EPI.

For a reliable comparison and evaluation, shift maps in the non-distorted and distorted coordinates should be determined under identical conditions. Furthermore, a robust method for calculating the shift map is important due to its high sensitivity to noise in regions with low SNR. Multi-reference scan methods [6-9] have been proposed without the need to unwrap ambiguous phase maps and to accurately calculate either the shift map in non-distorted or distorted coordinates. However, the measurement parameters cannot be easily reconciled with each other due to the fact that a different sequence for measuring the corresponding image of GE or EPI is required, since it contributes different sources for geometric distortions to the reconstructed images. Therefore, it is difficult to obtain a fair comparison for distortion correction using shift maps in the non-distorted and distorted phase-encoding coordinates.

In the PSF mapping method [22-27], only the shift map in the non-distorted coordinate is generally calculated from the reconstructed 3D PSF. However, integration of the 3D PSF data set along the distorted and non-distorted phase-encoding direction yields both non-distorted and distorted images, respectively. Thus, it is possible to calculate both the shift maps in distorted and non-distorted coordinates if the distortion terms are extracted from the phase information in the non-distorted (GE) and distorted (EPI) image similar to the field map method. Since the shift maps in the distorted and non-distorted coordinates are acquired with identical measurement parameters, a fair comparison for EPI distortion correction can be performed with the shift maps obtained by the PSF mapping method.

In this chapter, a modified PSF approach is proposed to determine a shift map in the distorted phase-encoding coordinate and is compared with the original PSF method, which

allows the shift map in the non-distorted coordinate to be obtained [22-27]. Additionally, in order to measure the PSF peak more accurately without the need of an interpolation method, a phase fitting method proposed by Ahn et al. [46] is adapted to the proposed shift map calculation scheme. The correction performance of the modified and original method is compared for phantom and *in vivo* data at 7T.

3.2 Theory

In chapter 2, Eq. 2.45 shows that the PSF can be replaced by a single delta function and an interpolation method is required to find the center of the PSF peak. Only the real part of the complex PSF data was considered to search the maximum and for interpolation of the peak position in Zaitsev et al.'s study [25] and two interpolation approaches, a three-point Lorenz and a three-point parabolic interpolation, were applied in the process. As an alternative, a Gaussian process modelling algorithm has been applied to the magnitude of the PSF data in order to allow the qualities of smoothness, sensitivity to various scales of the PSF distortions and a trend toward linearity in the measured shift map [26]. In the proposed method, phase images instead of the magnitude are used in the subsequent analysis to more accurately determine the shift in the PSF peak. Furthermore, it is demonstrated that both the shift maps in non-distorted and distorted phase-encoding coordinates can be derived from the 3D *k*-space data set obtained by the PSF mapping sequence.

3.2.1 Shift map in the non-distorted phase-encoding coordinate

Using Eq. 2.4 in the chapter 2, the acquired signal of the 3D *k*-space data set at a discrete time is given by

$$S(m\Delta k_x, n\Delta k_y, l\Delta k_s) = \int_x \int_y \rho(x,y)\exp[i\gamma\Delta B(x,y)(nT \pm m\Delta t + TE)] \cdot \exp[i(m\Delta k_x x + (n\Delta k_y + l\Delta k_s)y)]dxdy \quad (3.1)$$

$$-N_x/2 \le m < N_x/2, \quad -N_y/2 \le n < N_y/2, \quad -N_s/2 \le l < N_s/2$$

where the l^{th} spin-warp phase-encoding gradients are additionally encoded after repetitions and N_s is the total number of the additional encoding step. If the effects of the field inhomogeneity are negligible in the readout direction, the equation can be reduced to:

$$S(k_x, n\Delta k_y, k_s) = \int_x \int_y \rho(x,y) \exp\{i[\gamma \Delta B(x,y) TE + n\Delta k_y (y + \frac{\gamma \Delta B(x,y) T}{\Delta k_y})]\} \cdot \exp\{i[k_x x + k_s y]\} dx dy \tag{3.2}$$

After 2D inverse FT of the 3D *k*-space data set in k_x and k_s, a series of 2D images can be obtained along the k_y-dimension (corresponding to the EPI phase-encoding direction) and the image densities are (substituting *x* and *y* with *x'* and *y'*)

$$\begin{aligned} I_{GE}(x, s, n\Delta k_y) &= \int_{k_x} \int_{k_s} S(k_x, k_s, k_y) \exp[-i(k_x x + k_s s)] dk_x dk_s \\ &= \int_{x'} \int_{y'} \rho(x', y') \exp\{i[\gamma \Delta B(x', y') TE + n\Delta k_y (y' + \frac{\gamma \Delta B(x', y') T}{\Delta k_y})]\} \\ &\cdot \int_{k_x} \exp[ik_x (x' - x)] \int_{k_s} \exp[ik_s (y' - s)] dk_x dk_s dx' dy' \end{aligned} \tag{3.3}$$

$$I_{GE}(x, s, n\Delta k_y) = \exp\left\{ i \left[\gamma \Delta B(x,s) TE + n\Delta k_y (s + \frac{\gamma \Delta B(x,s) T}{\Delta k_y}) \right] \right\} \rho(x,s) \tag{3.4}$$

This equation shows that a series of geometrically non-distorted images can be obtained along the k_y-direction and the phase for the n^{th} measurement image is then

$$\Phi(x, s, n\Delta k_y) = \gamma \Delta B(x,s) TE + n\Delta k_y (s + \frac{\gamma \Delta B(x,s) T}{\Delta k_y}) \tag{3.5}$$

To calculate the pixel shift value of the PSF, the estimation of the first-order phase term along the k_y-direction is performed in the proposed calculation. An autocorrelation [46] between adjacent pixels is taken in the series of non-distorted images along the k_y-direction, which is given by

$$
\begin{aligned}
&angle\{E[I_{GE}(x,s,(n+1)\Delta k_y)I^*_{GE}(x,s,n\Delta k_y)]\} \\
&= \gamma\Delta B(x,s)TE + (n+1)\Delta k_y(s+\frac{\gamma\Delta B(x,s)T}{\Delta k_y}) - \left[\gamma\Delta B(x,s)TE + n\Delta k_y(s+\frac{\gamma\Delta B(x,s)T}{\Delta k_y})\right] \\
&= \Delta k_y(s+\frac{\gamma\Delta B(x,s)T}{\Delta k_y}) \\
&= \Delta k_y(s+\Delta(x,s))
\end{aligned}
\tag{3.6}
$$

where *E* denotes the statistical expectation, I^*_{GE} is the complex conjugate of the image I_{GE}. The additional first-order phase term represents the pixel shift (or the shift of the PSF peak) along the *s*-direction due to the field inhomogeneity. Therefore, the final shift map can be calculated by the formula:

$$
\Delta(x,s) = \frac{angle\{E[I_{GE}(x,s,(n+1)\Delta k_y)I^*_{GE}(x,s,n\Delta k_y)]\}}{\Delta k_y} - s \tag{3.7}
$$

which is the original form of the shift map in the non-distorted coordinate, corresponding to Eq. 2.45, as shown in the original PSF mapping method [22-27]. Thus, the proposed calculation can permit the shift map to measure the shift value of the PSF peak with no need for an interpolation step. As shown in Eq. 3.7, a statistical characteristic based on the series of non-distorted images is used in the calculation process and an accurate shift map with a high SNR can be obtained by the proposed method. Unlike the field map method that calculates the phase offset representing the phase evolution over the echo time in a reconstructed image, the shift value is directly obtained by calculating the additional first-order phase term in the proposed method.

3.2.2 Shift map in the distorted phase-encoding coordinate

Similarly, the shift map in a distorted phase-encoding coordinate (*y*) can also be obtained from the 3D *k*-space data set, which is newly suggested by the proposed method. Since the *s*-coordinate could be considered as a geometrically non-distorted phase-encoding coordinate as shown in Eq. 3.4, Eq. 3.2 can be rewritten as

$$S(m\Delta k_x, n\Delta k_y, l\Delta k_s) = \int_x \int_s \rho(x,s) \exp\{i[\gamma \Delta B(x,s) TE + l\Delta k_s s]\} \cdot \exp\left\{ i \left[m\Delta k_x x + n\Delta k_y \left(s + \frac{\gamma \Delta B(x,s) T}{\Delta k_y} \right) \right] \right\} dx ds \tag{3.8}$$

Similar to Eqs. 2.19-21 of the chapter 2, we can define the relation between the non-distorted (s) and distorted phase-encoding coordinate (y) as

$$y = s + \frac{\gamma \Delta B(x,s) T}{\Delta k_y} = R[s] \tag{3.9}$$

$$s = R^{-1}[y] \tag{3.10}$$

$$dy = \left(1 + \frac{\gamma \Delta B'(s) T}{\Delta k_y}\right) ds \tag{3.11}$$

Using the Eqs. 3.9-11, s in Eq. 3.8 can be substituted with y as

$$S(k_x, k_y, l\Delta k_s) = \int_x \int_y \left(1 + \frac{\gamma \Delta B'(R^{-1}[y]) T}{\Delta k_y}\right)^{-1} \rho(x, R^{-1}[y]) \cdot \exp\left\{ i \left[\gamma \Delta B(x, R^{-1}[y]) TE + l\Delta k_s \left(y - \frac{\gamma \Delta B(x, R^{-1}[y]) T}{\Delta k_y} \right) \right] \right\} \cdot \exp\{i[k_x x + k_y y]\} dx dy \tag{3.12}$$

After 2D inverse Fourier transform of $S(k_x, k_y, l\Delta k_s)$ in k_x and k_y, the reconstructed 2D image densities along the k_s-dimension are obtained (substituting x and y with x' and y'):

$$
\begin{aligned}
I_{EPI}(x,y,l\Delta k_s) &= \int_{k_x}\int_{k_y} S(k_x,k_y,l\Delta k_s)\exp[-i(k_x x+k_y y)]dk_x dk_y \\
&= \int_{x'}\int_{y}(1+\frac{\gamma\Delta B'(R^{-1}[y'])T}{\Delta k_y})^{-1}\rho(x',R^{-1}[y']) \\
&\cdot\exp\left\{i\left[\gamma\Delta B(x',R^{-1}[y'])TE+l\Delta k_s(y-\frac{\gamma\Delta B(x',R^{-1}[y'])T}{\Delta k_y})\right]\right\} \\
&\cdot\int_{k_x}\exp[ik_x(x'-x)]\int_{k_y}\exp[-ik_y(y'-y)]dx'dy'dk_x dk_y \\
&= (1+\frac{\gamma\Delta B'(R^{-1}[s])T}{\Delta k_y})^{-1}\rho(x,R^{-1}[s]) \\
&\cdot\exp\left\{i\left[\gamma\Delta B(x,R^{-1}[s])TE+l\Delta k_s(y-\frac{\gamma\Delta B(x,R^{-1}[s])T}{\Delta k_y})\right]\right\}
\end{aligned}
\tag{3.13}
$$

$$
\begin{aligned}
I_{EPI}(x,y,l\Delta k_s) &= (1+\frac{\gamma\Delta B'(y)T}{\Delta k_y})^{-1}\rho(x,y) \\
&\cdot\exp\left\{i\left[\gamma\Delta B(x,y)TE+l\Delta k_s(y-\frac{\gamma\Delta B(x,y)T}{\Delta k_y})\right]\right\}
\end{aligned}
\tag{3.14}
$$

This equation shows that all reconstructed 2D images are distorted in the phase-encoding direction (y) due to the field inhomogeneity. The phase for the l^{th} measurement image is then

$$
\Phi(x,y,l\Delta k_s) = \gamma\Delta B(x,y)TE+l\Delta k_s(y-\frac{\gamma\Delta B(x,y)T}{\Delta k_y})
\tag{3.15}
$$

An autocorrelation between adjacent pixels is taken in the series of distorted images [46] along the k_s-direction, which is given by

$$
\begin{aligned}
&angle\{E[I_{EPI}(x,y,(l+1)\Delta k_s)I^*_{EPI}(x,y,l\Delta k_s)]\} \\
&= \Delta k_s(y-\frac{\gamma\Delta B(x,y)T}{\Delta k_y}) \\
&= \Delta k_s(y-\Delta(x,y))
\end{aligned}
\tag{3.16}
$$

Therefore, the proposed shift map in the distorted phase-encoding coordinate is finally obtained by

$$\Delta(x,y) = -\frac{angle\{E[I_{EPI}(x,y,(l+1)\Delta k_s)I^*_{EPI}(x,y,l\Delta k_s)]\}}{\Delta k_s} + y \tag{3.17}$$

which is the simplified form of the proposed PSF and thus, it is a mapping result of the PSF peak position by a single delta approximation in the distorted EPI phase-encoding coordinate (y) instead of the non-distorted spin-warp phase-encoding coordinate (s) [22-27]. The proposed calculation thus allows an EPI-based shift map based on the series of distorted images.

As shown in Eqs. 3.7 and 3.17, both of the shift maps in the non-distorted and distorted phase-encoding coordinates can be obtained from a 3D k-space data set obtained by the PSF mapping method. The calculated shift map $\Delta(x,s)$ indicates the vertical deviation for the PSF peak from the diagonal line in y-s space, whereas shift map $\Delta(x,y)$ is the horizontal deviation from this diagonal line. While the shift (peak of the PSF) $\Delta(x,s)$ is identical for both methods, this may not fully generalize to the shape of a realistically broadened PSF. Due to this transformation, a shift map based on the distorted EPI image is obtained in the proposed method as opposed to the shift map in non-distorted coordinates, as previously suggested [22-27]. Under realistic conditions, signal decay during the echo train and eddy current effects cause the shifts as well as broadening of the PSF peak from the ideal δ function. In practice, the PSF broadening can exceed many pixels due to susceptibility effects, especially at UHF.

Therefore, the shift maps in distorted and non-distorted phase-encoding coordinates can be obviously different. In particular, while the broadening of the PSF may be represented in several pixels in the distorted coordinate (y), PSF mapping in the non-distorted coordinates (s) results in a single shift value for the PSF peak. Consequently, PSF mapping in the distorted coordinates can determine shift values for each pixel of the original EPI image. If the shift is determined in the non-distorted coordinates, the same shift value must be applied to multiple original voxels or missing support points to be interpolated. Therefore, the proposed shift map $\Delta(x,y)$ allows mapping the shifted PSF as well as the broadened

PSF. As a result, EPI distortions are mapped with more support points, which allows a higher spatial accuracy in the correction. However, the opposite would be expected in a compressed region where several PSFs originating from different positions *s* are aligned along the same *y*-coordinate in the different *s*-coordinates. In this case, PSF mapping in the distorted phase-encoding coordinates (*y*) results in a single shift value for the several PSFs whereas PSF mapping in the non-distorted phase-encoding coordinate (*s*) can determine all shift values for each PSF in the region. In order to demonstrate the performance of the correction using the two different types of shift maps with identical measurement parameters, a fair comparison study is required, especially for UHF.

3.3 Materials and Methods

3.3.1 Experimental parameters

The performance for the distortion correction using both shift maps in the non-distorted and distorted coordinates was evaluated in phantoms and in *in vivo* measurements of a human brain on a 7T whole body MRI (Siemens Healthcare, Erlangen, Germany) using an eight channel head array coil (Rapid Biomedical, Würzburg, Germany). In the phantom experiment, a spherical oil phantom (diameter 17cm) was used to avoid strong B1+-inhomogeneities and was partially filled to increase large susceptibility effects. In order to access correction fidelity more clearly in the case of strong geometric distortions, a longer TE value was used in both the phantom and human experiments.

Imaging parameters in a phantom experiment were FOV = 256×256 mm^2, slice thickness = 4 mm, matrix = 128×128, TR/TE = 500/52 ms, bandwidth = 1500 Hz/px, echo spacing = 730 µs. The human experiments were performed with two different parameter sets: (I) FOV = 224×224 mm^2, slice thickness = 1.4 mm, matrix = 160×160, TR/TE = 3000/58 ms, bandwidth = 1360 Hz/px, echo spacing = 860 µs, and (II) FOV = 212×212 mm^2, slice thickness = 2 mm, matrix = 106×106, partial Fourier = 6/8, TR/TE = 3000/29 ms, bandwidth = 1360 Hz/px, echo spacing = 700 µs were used.

The proposed study was evaluated in conventional gradient-echo EPI and the corresponding PSF data acquired using the PSF sequence developed by Zaitsev et al. [25].

The methods were applied to healthy volunteers with IRB approval after receiving informed written consent. The results of this modified method are compared with the results of the method originally implemented by Zaitsev et al. [25].

3.3.2 Processing procedure

Figure 9 shows the proposed processing procedure for calculating the shift maps in non-distorted and distorted coordinates for a comparison of the correction performance. To calculate an optimal shift map in the non-distorted and distorted coordinates, the processing procedure proposed by Zaitsev et al. [25] was basically used. In addition, four modifications were added to the procedure to calculate a proposed shift map in the distorted coordinate.

(I) After 3D PSF data are obtained by 3D inverse FFT of the 3D *k*-space data (Fig. 1b) acquired by the PSF mapping sequence, an image mask is created to limit the calculation to areas with sufficient signals inside the object. In contrast to the original implementation [25], which calculates the non-distorted standard deviation (GE-StdDev) image along the distorted phase-encoding direction (in the non-distorted spin-warp phase-encoding coordinates), the distorted EPI StdDev (EPI-StdDev) image was calculated from the 3D PSF data along the non-distorted spin-warp phase-encoding direction (in the distorted phase-encoding coordinates). Simple thresholding leads to the image mask.

(II) Phase correction of the 3D PSF data to avoid the appearance of step-like patterns in the proposed shift map was applied to the EPI image, which can be obtained by integration along the non-distorted spin-warp phase-encoding direction, instead of the GE image as used in the original implementation.

(III) As explained in the theory section, the calculation of first-order phase evolution was performed after a 1D Fourier transformation of the single voxel PSF back into k_s and k_y space to measure the shifts of each PSF's peak in non-distorted spin-warp (s) and distorted EPI phase-encoding coordinates (y), respectively. To accurately determine subvoxel shifts corresponding to the shift of the PSF peak from the diagonal line (as shown in Fig. 10d) without any interpolation step, an autocorrelation method proposed by Ahn et al. [46] was used. After weighted linear extrapolation of the shift map into the areas outside of the mask, a 2D three-pixel median filter is applied to smooth the raw shift map, which results in the

final shift map.

(IV) In the image space, EPI distortion correction is performed by a standard convolution kernel estimated by the *b*-spline interpolation method [47,48]. An estimation of the convolution kernel for each pixel in the distorted image including the effects of finite sampling is important to permit an efficient distortion correction, since pixels in the compressed and stretched regions from the distorted image should be distributed differently. A 1D 2^{nd} order *b*-spline interpolation with 3 support points, which includes a pixel shift value and the differences between two adjacent pixel shift values (left and right positions) along the phase-encoding direction, is used for high estimation accuracy with acceptable calculation times.

An amplitude correction procedure is added in the original method to restore the image intensity of the distortion corrected EPI. The spatial derivatives in the shift map in the phase-encoding direction were calculated as scaling factors for the amplitude correction. Such amplitude correction is only applied to the original method, not the proposed modified method, in which the intensity is intrinsically corrected, since all original EPI voxels are corrected by the proposed convolution kernel with their corresponding shift values. All procedures were implemented using the Matlab (MathWorks, Natick, MA) environment and were used to reconstruct the data shown in this comparison study.

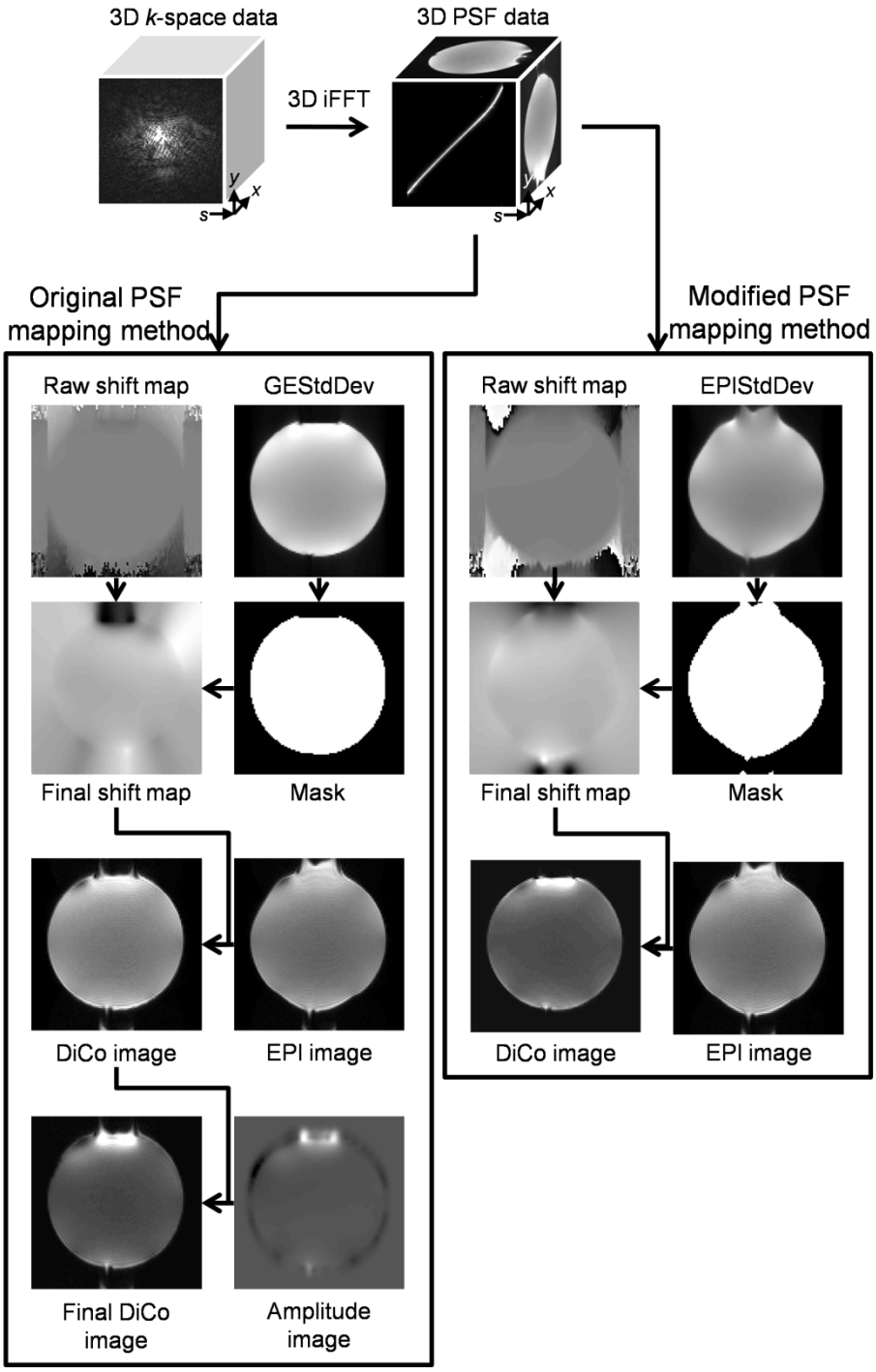

Figure 9: The processing procedure resulting in shift map in the distorted and non-distorted coordinate. To additionally calculate a shift map in the distorted coordinates, a modified PSF mapping procedure is proposed based on the original PSF mapping procedure.

3.4 Results

3.4.1 Difference between two shift maps

Figure 10 illustrates the determination of the shift map along the two phase-encoding directions and the differences in a stretched region. In all images in Fig. 10, *x*, *y*, and *s* indicate the readout (frequency-encoding), distorted (EPI) phase-encoding, and non-distorted (spin-warp) phase-encoding direction, respectively. In Fig. 10I-b, a 3D PSF data set and the relation between the non-distorted image in the *x*-*s* plane (top), distorted image in the *x*-*y* plane (right) and the 2D PSF in the *y*-*s* plane at the center of the *x* position (front) are shown. Different types of the shift maps in the distorted (10I-a) and non-distorted phase-encoding coordinate (10I-c) are calculated from the 3D PSF data set due to the PSF distortions as shown in an example of the further expansion of the 2D PSF image (10I-d). In Fig. 10I-d, both the ideal correlation line and the experimentally obtained (distorted PSF data) correlation line are displayed in detail. As shown in this figure, the experimental correlation line is shifted upward and broadened due to B_0 field inhomogeneity and susceptibility effects. Therefore, the experimental correlation line (peaks of single voxel PSF) is usually not aligned along the diagonal direction due to distortions and the deviation from the diagonal means an estimation of the PSF's shift or distortion. Fig. 10II illustrates the difference in shift determinations along the two possible coordinates (*y* and *s*) in an area of strongly stretched distortions. The 6 simplified data points of PSFs with the width of the PSFs corresponding to 1, 2, or 3 pixels in the *y*-direction are shown as colored dots in Fig. 10II-b. The corresponding shift maps in the distorted EPI phase-encoding coordinate (*x*-*y*) and non-distorted spin-warp phase-encoding coordinate (*x*-*s*) [22-27] are shown in Fig. 10II-a and 10II-d, respectively. Only one shift value (the peak) for each PSF in *y*-direction was measured using the original PSF mapping method in the non-distorted spin-warp phase-encoding coordinates. Therefore, figure 10II-d shows that only 6 shift values are obtained for 6 voxels at the corrected positions. In contrast, PSF mapping in the distorted EPI phase-encoding coordinates allows the shift to be determined and the broadening of the PSF, which results in the shift values for all 9 original EPI voxels in the distorted EPI phase-encoding coordinates, as shown in Fig. 10II-a.

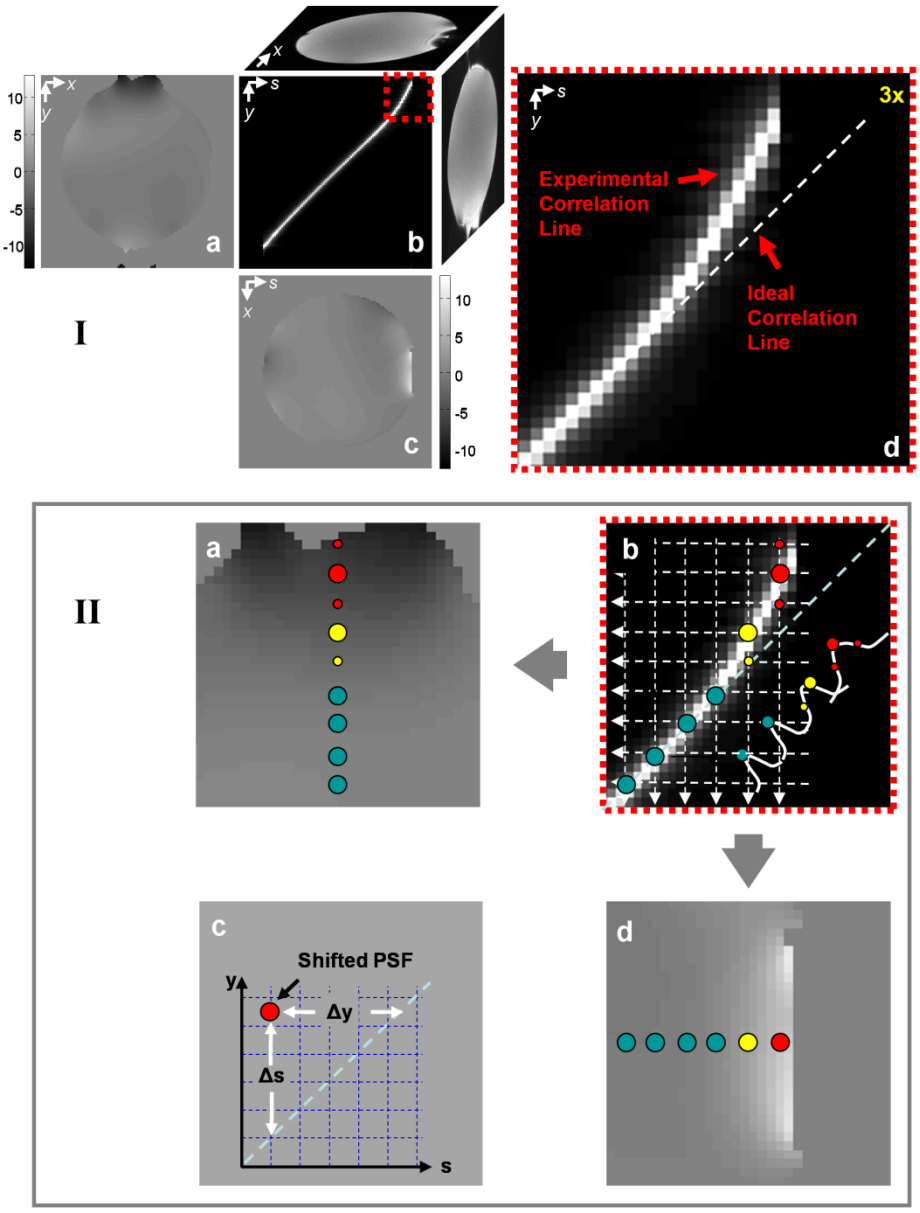

Figure 10: The right image in (I) shows an example of PSF data where the experimental correlation line deviates from the diagonal indicating susceptibility dependent distortion (see text for more detail). (II) displays the PSF mapping results calculated in the non-distorted spin-warp phase-encoding coordinate (*s*) and the distorted phase-encoding coordinate (*y*): (II-a) illustrated the mapping result obtained by PSF mapping in the distorted phase-encoding coordinate (proposed method), (II-b) shows a 2D plane of the 3D PSF data with highlighted example voxels, (II-c) indicates the identity of the shift values when calculated in the distorted phase-encoding coordinate (*y*) instead of the non-distorted spin-warp phase-encoding coordinate (*s*), (II-d) depicts the result obtained by PSF mapping in the non-distorted spin-warp phase-encoding coordinate (as previously proposed).

Figure 11 shows data for the shift map determination along the two phase-encoding directions and the differences in a strongly compressed region. As shown in an example of a further expansion of the 2D PSF image (11I-d), the experimental correlation line is shifted downward and broadened due to B_0 field inhomogeneity and susceptibility effects and leads to compressed distortions in the EPI image. As shown in this figure, the distorted PSF data are aligned along almost the same *y* position (parallel to the *s*-direction), especially in strongly compressed regions. As illustrated in Fig. 11II, large differences of the shift map determination along the two possible coordinates (*y*, *s*) can be seen in such areas. In Fig. 11II-b, the simplified 10 data points of PSFs are shown as the colored dots. In contrast to the stretched region, only one shift value (the peak) for 4 PSFs in *s*-direction was measured by the modified PSF mapping method in the distorted phase-encoding coordinates (11II-a). In contrast, all distortions of the simplified 4 PSFs in the strongly compressed area are measured by the original PSF mapping in the non-distorted spin-warp phase-encoding coordinates (11II-d). Therefore, 10 shift values are obtained for 10 voxels at the corrected positions and a shift value is missed in the slightly stretched area (see the blue dot in Fig. 11II-d). In contrast, the modified PSF mapping in the distorted EPI phase-encoding coordinates allows only 8 EPI voxels and 3 shift values and a shift value is, respectively, missed in the compressed area and added in the stretched area (see Fig. 11II-a). The distortion information of the proposed shift map for distortion correction is increased or decreased depending on whether the region of the EPI image is bulged and shrunken. The opposite occurs in the shift map in the original method. Complementary information about image distortions is measured with both the shift maps in non-distorted and distorted coordinates.

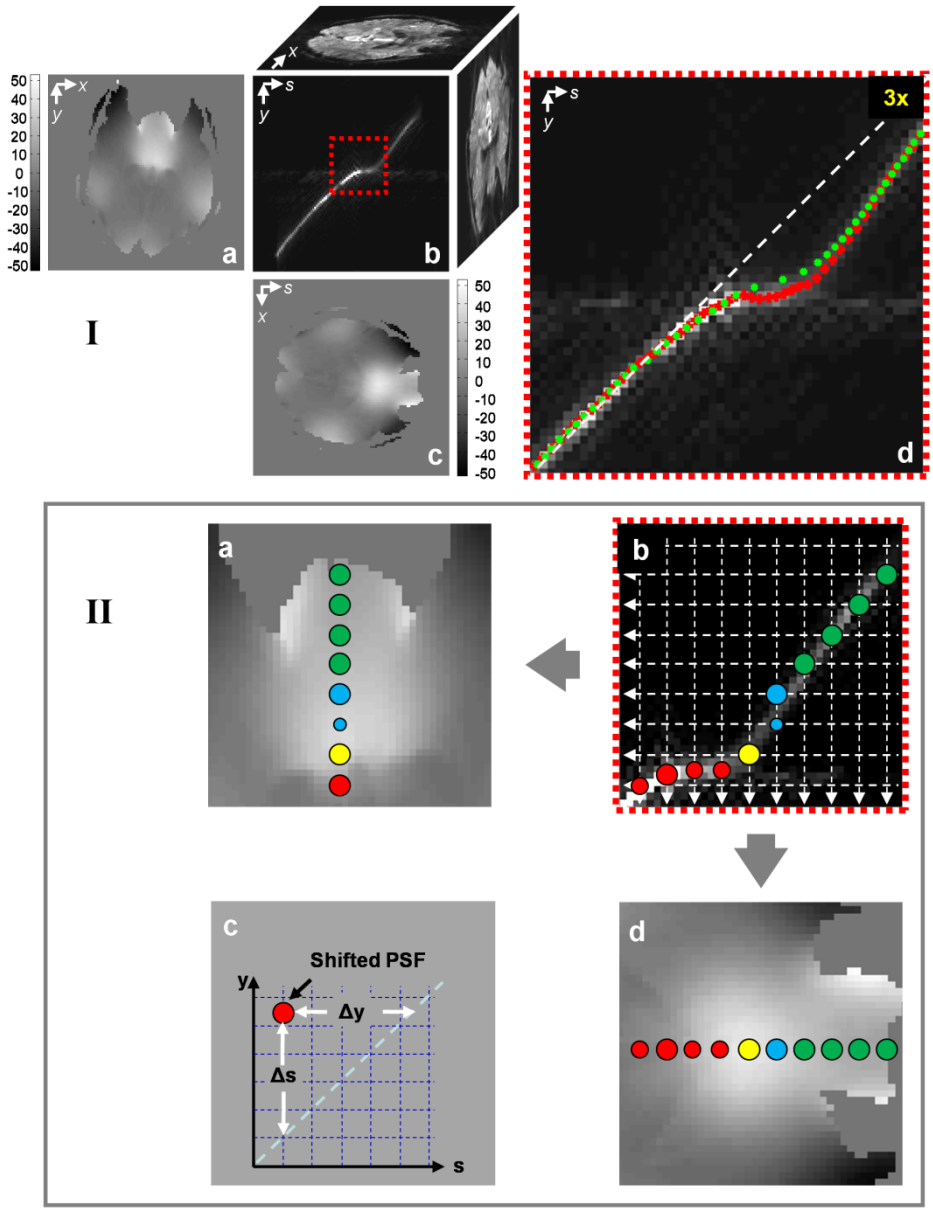

Figure 11: The difference of PSF mapping in the distorted phase-encoding coordinate (*y*) and the non-distorted spin-warp phase-encoding coordinate (*s*) in strongly compressed regions. An identical processing is used as described in Fig. 10. In the compressed regions, the original PSF mapping technique in the non-distorted spin-warp phase-encoding coordinate (the *x*-*s* plane) allows more information concerning image compression to be obtained, compared to the PSF mapping in the distorted phase-encoding coordinate (in the *x*-*y* plane).

3.4.2 Geometric distortion correction

Figure 12 shows phantom results. In the distorted EPI image (Fig. 12I-a), stretching effects are clearly visible due to distortions. The proposed method calculates a shift map based on the distorted EPI image (Fig. 12I-b) while a shift map based on the non-distorted image (Fig. 12I-c) is obtained by the original method. The shifts partially remain when corrected using the original method (Fig. 12I-g and I-i). A significantly improved geometry correction was achieved using the proposed shift map (Fig. 12I-f) due to the fact that more information was available regarding image stretching. In the case of shrunken regions, the original method provides a slightly better or similar correction result (Fig. 12I-g) compared to the proposed method (Fig. 12I-f) although it allows potentially more information to be obtained about the image compression.

Figure 13 shows the distortion corrected results of the human brain in the stretched (Fig. 13I) and compressed region (Fig. 13II). While it was not possible to eliminate significant edge blurring by the original method (Fig. 13I-g), a markedly better delineation of the brain outline, i.e. in the occipital region, was obtained with the distortion corrected image resulting from the proposed method (Fig. 13I-f) and the geometry agrees very well with the non-distorted reference (GE-StdDev) image (Fig. 13I-h). The amplitude corrected result in the original method (Fig. 13I-i) shows an increase in signal intensity i.e. in the posterior region that is intrinsically included in the proposed method. Interestingly, although the original shift map includes more information related to compressed distortions as shown in Fig. 11, severe errors are caused by the information in the corrected EPI image and this usually occurred near the boundary of the brain in the center of the slice where strong susceptibility effects come into play (Fig. 13II-g). Most of the false, high signal due to the strong stretching of this region can be reduced by the amplitude correction of the distortion corrected image, but residual errors continue to remain there. (Fig. 13II-i). Compared to the original method, the geometric distortions are corrected well by the proposed method, even with less information regarding distortions being available for the compressed region. In addition, intensity correction is intrinsically done in the proposed method and an extra step as in the original method, is not required.

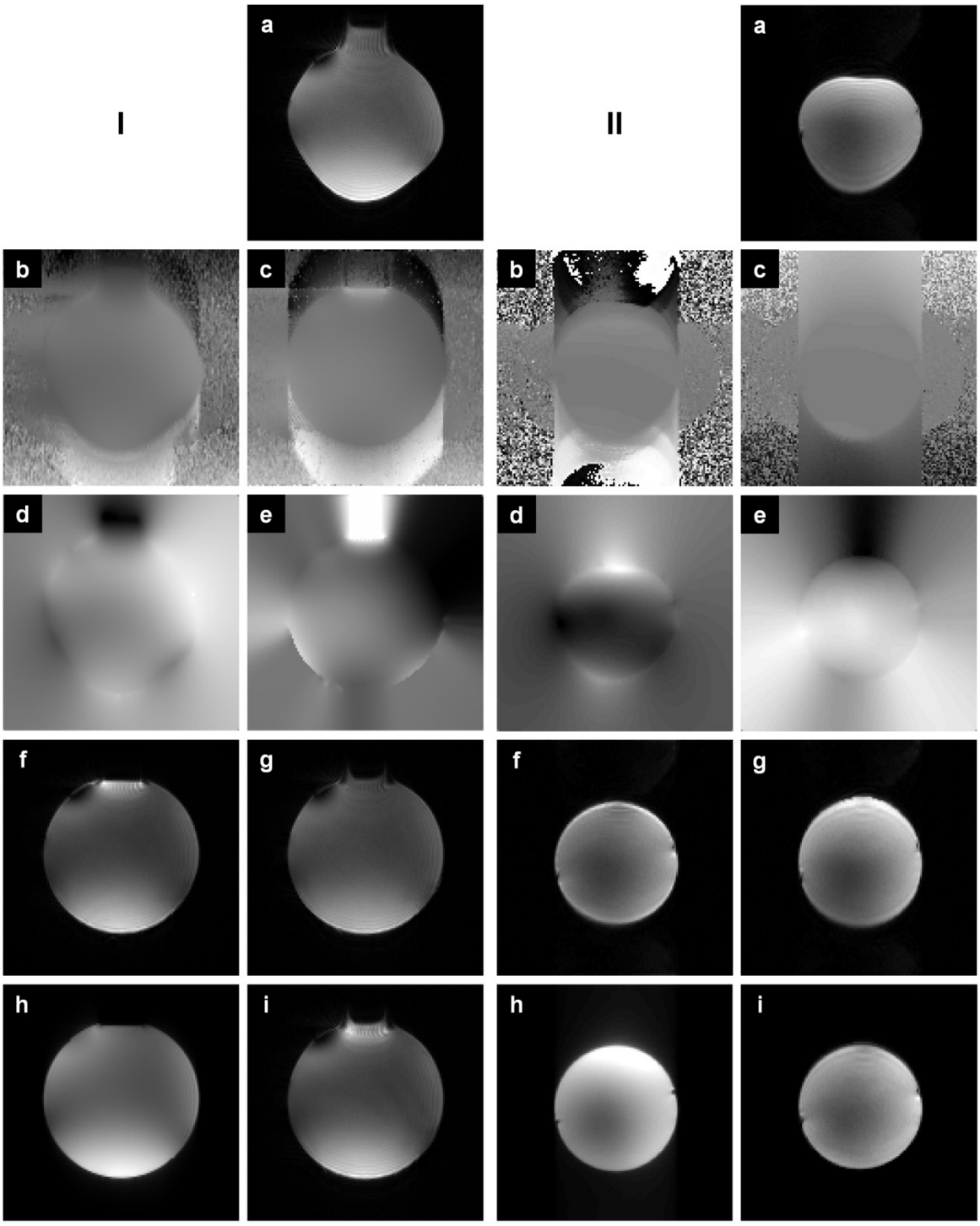

Figure 12: The phantom results in the stretched (I) and compressed region (II): (a) Distorted EPI image, (b) proposed shift map using PSF mapping in the distorted EPI phase-encoding coordinate, (c) shift map in the non-distorted spin-warp phase-encoding coordinate, (d) and (e) extrapolated final shift maps of (b) and (c), (f) and (g) EPI image corrected by the shift maps (d) and (e), respectively. (h) non-distorted image (GE-StdDev) for reference, (i) EPI image after amplitude correction of the distortion corrected EPI image (g).

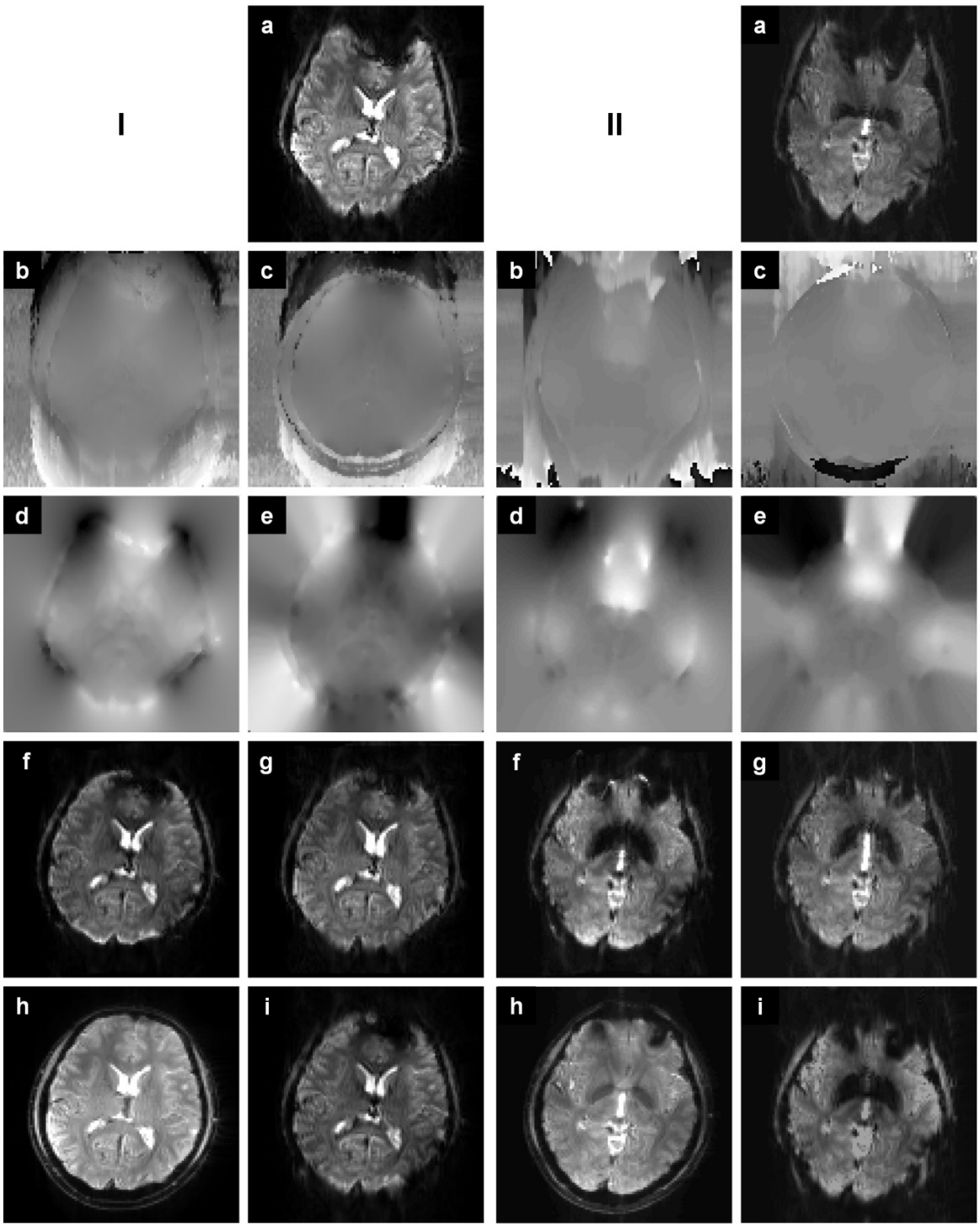

Figure 13: In vivo example with identical processing as described in Fig. 12. The proposed processing result (f) shows fewer remaining artifacts and a clearer brain and skull depiction than the original PSF method (i).

3.4.3 PSF-ghost artifacts

In the case of *in vivo* imaging, distortion detection can be strongly affected by potential PSF-ghost artifacts. This phenomenon, as illustrated in Fig. 14, is caused by echo center shifts along the *s*-direction and the multi-shot nature of the PSF scan. Here, a strong PSF-ghost artifact along the *s*-direction appears in the 3D PSF data, especially in the ventricle region of the human data. Both the PSF-ghost and the original PSF are simultaneously contained (see Fig. 14c). Compared to the original PSF in the artifact-free region, the PSF-ghost can have a higher intensity when PSF peak mapping is performed along the *y*-direction in the non-distorted spin-warp phase-encoding coordinates (*x*-*s* plane). In this case, the shift value of the PSF-ghost can be designated as its original shift value instead of the shift value for the original PSF. As shown in the further enlarged 2D PSF image (Fig. 14d), a red line is not located on the original PSF data due to the PSF-ghost artifacts. In contrast, the shift value of the original PSF is assigned despite the existence of strong PSF-ghosts if the PSF peak mapping is carried out along the *s*-direction in the distorted EPI phase-encoding coordinates. Firstly, both the original PSF and the PSF-ghost are placed on the same horizontal line (*s*-direction). Secondly, the original PSF typically has a higher intensity than the corresponding PSF-ghost along the *s*-direction. Therefore, even in the presence of strong PSF-ghost artifacts, the PSF peak can be measured more robustly in the distorted coordinates (see the green line in Fig. 14d). Thus, PSF mapping in the distorted EPI phase-encoding coordinates is able to accurately correct geometric distortions and it is possible to eliminate the shift map assignment errors induced by the PSF-ghosts (see Fig. 14a).

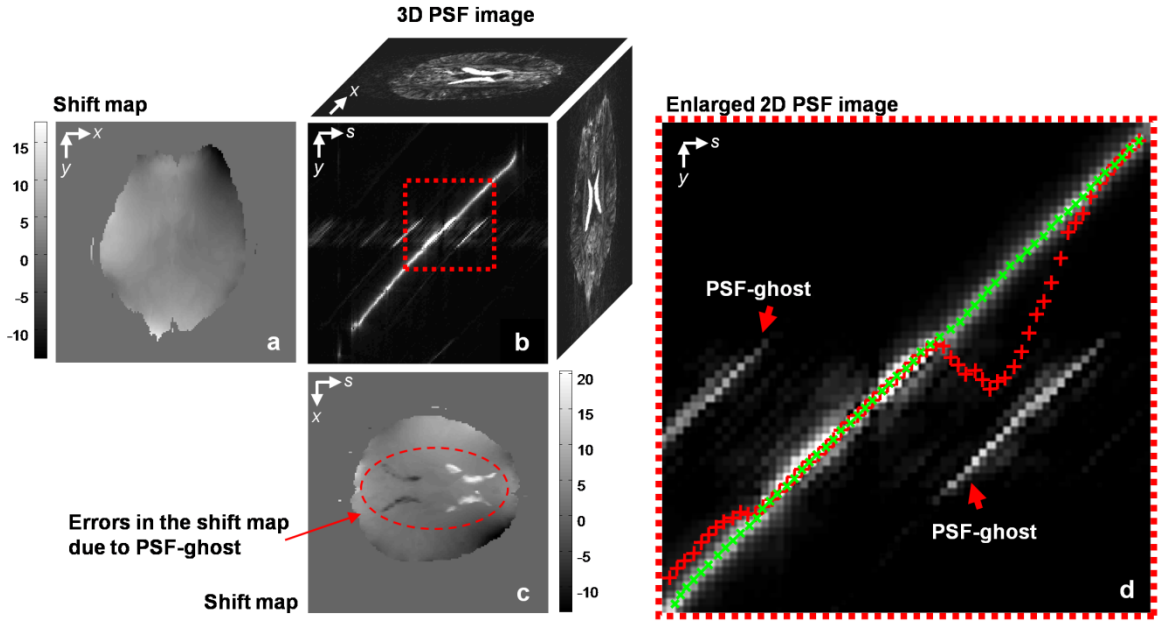

Figure 14: Difference in PSF mapping in a distorted phase-encoding coordinate (*y*) and a non-distorted spin-warp phase-encoding coordinate (*s*) in an in vivo human brain data set. For the PSF mapping technique in the non-distorted spin-warp phase-encoding coordinate (in the *x*-*s* plane), distortions as well as PSF-ghosts can be identified. However, an artifact free distortion map is calculated with PSF mapping in the distorted phase-encoding coordinate (in the *x*-*y* plane).

Figure 15 shows the errors induced by the PSF-ghost in the measured shift map and the effects of the correction in human brain imaging. The PSF-ghost errors in the ventricle regions are clearly visible in the shift map of the original method (Fig. 15a). In this case, severe errors are caused by the PSF-ghost artifacts in the corrected EPI image (Fig. 15e). Figure 15d demonstrates that the geometric distortions are corrected well by the proposed method since the shift map is not vitiated by the PSF-ghost artifacts in the proposed calculation process as shown in Fig. 15b. The correction differences between the proposed and original method are clearly seen in Fig. 15 (see arrows). In addition, a much improved correction is obvious near the edges of the brain (frontal and occipital).

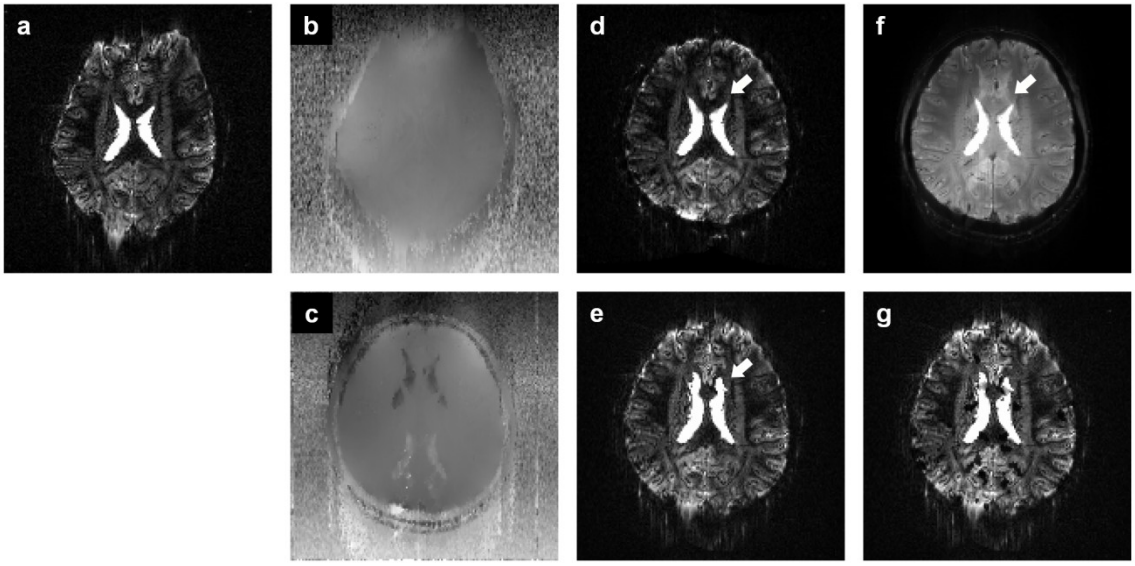

Figure 15: Shift map errors caused by the PSF-ghost and the distortion corrected results of the human brain *in vivo*. The ventricle signal is originally higher than the tissue signal in the case of long TE: (a) distorted EPI image, (b) raw shift map calculated by the proposed method, (c) raw shift map obtained by the original method, (d) correction results by the proposed method, (e) correction results by the original method, (f) non-distorted reference image (GE-StdDev), (g) original method including amplitude correction.

3.5 Discussion

In this chapter, an EPI-based shift map was newly determined using the modified PSF mapping method and the correction performance was then compared with the original method at 7T. The calculation of the shift map in the distorted EPI phase-encoding coordinates, which results in a more precise localization of the PSF peak for a more accurate determination of the PSF shift, is proposed. The results demonstrate that the proposed method allows a high-accuracy correction performance compared to the originally proposed method, especially in regions with strong field inhomogeneities. Due to the accuracy of the method, the correction differences are prominent as shown in Figs. 12, 13, and 15. In the proposed method, many structures are delineated more clearly and with reduced blurring than in the originally proposed method due to the increased information about distortion in such areas. Therefore, the improved correction accuracy and decreased blurring provides a benefit in studies of structures close to the brain surface

(i.e. retinotopic mapping of the foveal area represented at the occipital pole). In addition, correction accuracy is also valuable for the corregistration of anatomical and functional data and for spatial normalization of brain images to a standard template as is used in fMRI data analysis with automated image-matching algorithms [49-52]. In the original method, the segmented brain mask calculated from a GE-StdDev image typically excludes the low signal regions of the skin [25]. To minimize masking errors in these peripheral regions, an adequate extrapolation process is usually necessary to take into account the correction for residual distortion. Unfortunately, it is impossible to accurately determine the distortions in areas with low or no signal intensity. In the proposed method, the EPI-StdDev image is used for mask generation and this allows a segmentation mask including areas of the skin signal. Since the image segmentation mask significantly affects the final appearance of the distortion corrected results, accuracy is very important. To further yield a more robust segmentation mask, a method (e.g., including the complete 3D PSF data) will be a subject of future study.

In human brain imaging, the pronounced PSF-ghost artifacts appear as shifted signals of the PSF data along the *s*-direction mainly in the ventricles. We may conclude that the artifacts are caused by a combination of local phase errors and a large *k*-space shift in the low and high k_s-encoding steps due to the fact that images are reconstructed from different k_s-encoding steps before a fast Fourier transformation in the k_s-dimension (data not shown – see [53]), Namely, the amount of phase-encoding in the k_s-dimension is limited by the encoding in the k_y-dimension and the original PSF mapping method needs to cover the center line of *k*-space sufficiently. Otherwise, with a large *k*-space shift in the k_s-direction, strong artifacts can appear in the reconstructed images, since a shift or dispersion of the signal in *k*-space can cause artifacts. This is similar to asymmetric (half Fourier) sampling in the *k*-space, where phase estimation from low resolution data is required in order to minimize signal reductions and the generation of strong artifacts. In general, most of these artifacts occur in regions with strong phase differences induced by pulsatile flow, motion, or local field inhomogeneities. In addition, the multi-shot nature of PSF mapping to fill the k_s-dimension enhances the sensitivity. From such PSF-ghost signals, the potentially false shift determination can be avoided by the proposed shift calculation along the *s*-direction. Due to large k_s-shifts in *k*-space, the effects of CSF motion are strongly enhanced in the *in vivo* PSF data. Strong differences in the signal can be caused by even small phase changes if the echo center is substantially shifted. A shift in the echo center alone will not lead to a

strong error, provided the phase dispersion is fixed and temporally constant. Since minor errors arise from head motion with complete coverage of *k*-space in GE images, the oscillatory motion of CSF in the brain is driven by brain expansion and contraction during the cardiac cycle, cardiac motion, and respiratory motion [54-57]. However, these artifacts appear more significantly in the case of combinations of effects, both signal variations and large k_s-shifts (relative to the k_y-encoding).

The measurement parameters of the PSF mapping sequence such as TE and TR also affect the shift map errors induced by PSF-ghost artifacts. In the case of long TE at higher magnetic field, the signal intensity of the PSF-ghosts is relatively increased due to longer T2 value of CSF compared to brain tissue (see Fig. 15). Furthermore, signal intensity differences between ventricle and brain tissue are often increased in areas near the air/tissue interface around the cervical carotid artery, especially in the case of UHF. Since susceptibility effects induce local phase gradients around these structures, differences in the effective TE cause these intensity differences. Thus, PSF-ghost artifacts become more conspicuous as the source of the shift map errors in the original method. Only the shift map calculation in the distorted EPI phase-encoding coordinates (y) can eliminate such PSF-ghost errors in the shift map.

Although not explicitly shown here, reductions in the field of view (rFOV) [58] and parallel imaging techniques [5-7] along the PSF dimension, as introduced previously [25], are compatible with the proposed PSF mapping method. In these experiments, EPI and corresponding PSF acquisitions were achieved without the use of parallel imaging techniques in order to validate the correction performance of the modified and original methods, even for severe distortions. Additional benefits are accrued if the strength of the distortions is decreased by a parallel imaging technique to further improve image quality.

A shift map $\Delta(x, y)$ in the distorted EPI phase-encoding coordinates was also applied to correct the distortions in the method by Stevick et al. [26]. However, the shift map was obtained by remapping of the shift map $\Delta(x, s)$ determined in the non-distorted spin-warp phase-encoding coordinates. In this process, compared to the proposed method, an additional interpolation is needed to produce a precise and smoothly varying shift map. In addition, no benefit regarding distortion information is gained and potential PSF-ghost artifacts are unaddressed in this method [26].

The distortion correction is performed via a deconvolution and convolution procedure

using the shift map in the non-distorted and distorted phase-encoding coordinate, respectively and the difference is illustrated in Fig. 16. Using the original shift map $\Delta(x,s)$, an interpolated value from the distorted image fills a pixel of the corrected image in the original method. Due to lost information of the blurring effects of the PSF in the stretched area, some residual errors still remain near the boundary of the mask area, as shown in Fig. 16I-e. In the proposed method, the correction is performed by redistributing the pixels of the distorted image using the *b*-spline interpolation method. All of the distortion information in the stretched region is measured in the proposed shift map $\Delta(x,y)$ and blurring effects of the distorted image can be corrected by the proposed method, as shown in Fig. 16I-f. In strongly compressed regions, the original shift map (Fig. 16II-a) includes more information regarding such distortions than the proposed shift map (Fig. 16II-b). However, an erroneous stretched image is obtained as the result of the correction, since several pixels in the corrected image are filled with an interpolation value from the distorted image (see Fig. 16II-e). Namely, additional correction errors are produced by the original method although more information concerning distortions is contained in the shift map, especially in strongly compressed regions where several pixels are compressed into one pixel. In contrast, a pixel is split into two or three pixels for the correction of compressed distortions in the proposed method. Since the width of the distribution is determined by the difference between two adjacent shift values (left and right), an effective correction can be performed with the proposed shift map, despite less information regarding distortions is available. In addition, the image intensity is consequently increased in stretched regions (Fig. 16I-f) and reduced in compressed areas (Fig. 16II-f) after the distortion correction. Thus, amplitude correction is inherently carried out and an extra calculation step is not required in the proposed method. In the original method, however, since the same image intensity as in the distorted image is maintained by the correction process even in stretched (Fig. 16I-e) or compressed regions (Fig. 16II-e), amplitude correction as an additional procedure needs to be considered to restore the image intensity after geometric distortion correction.

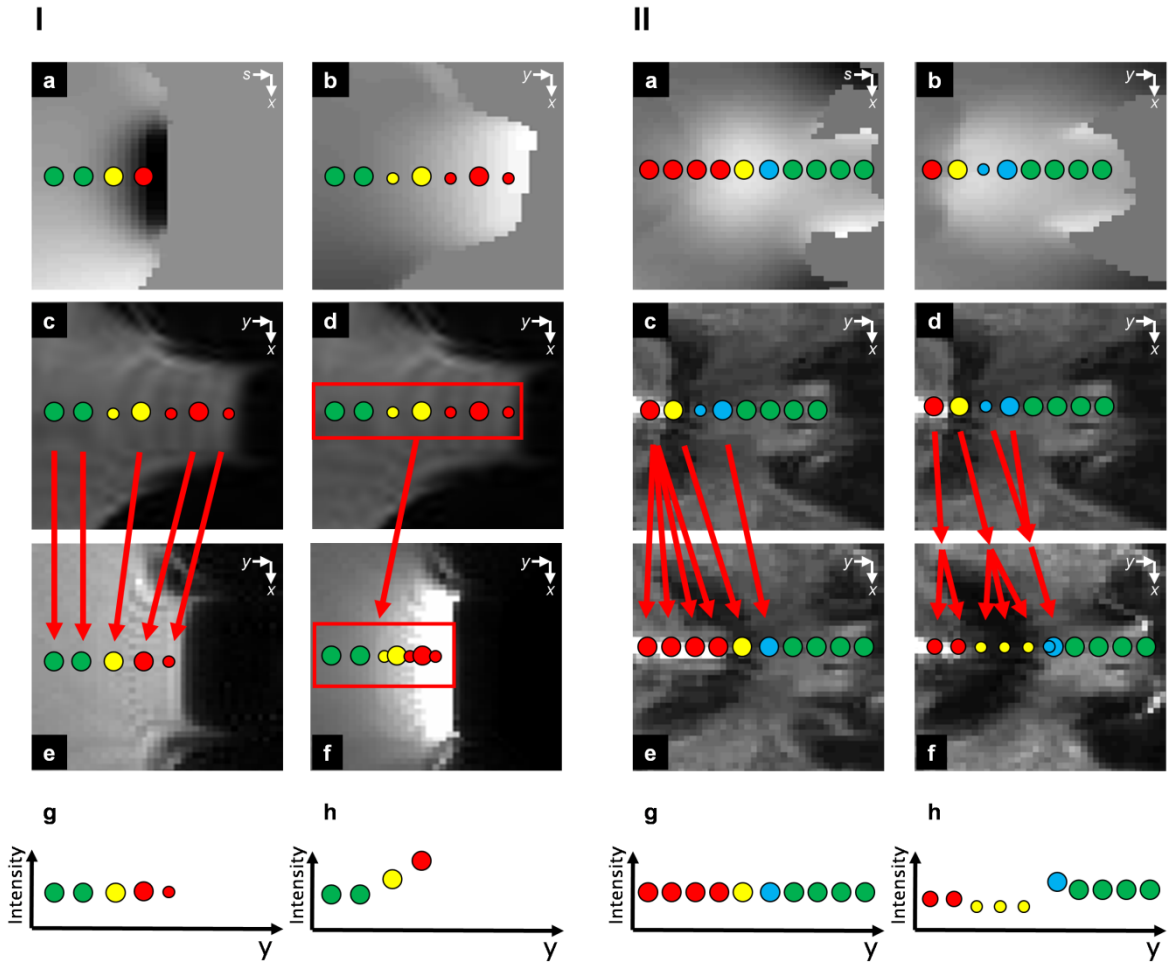

Figure 16: In the stretched (I) and compressed area (II), the correction process using the original (left column) and proposed method (right column) is illustrated: (a) the original shift map, (b) the proposed shift map, (c-d) distorted EPI image, (e) distortion corrected EPI image by the original method, (f) distortion corrected EPI image by the proposed method, and (g) and (h) show the image intensity after correction by the original and proposed method, respectively.

Local susceptibility gradients in the phase-encoding direction cause geometric distortions as well as shift the *k*-space center to shorter or longer effective echo times when the phase-encoding direction is chosen. Due to the effects of echo times shifts, hyperintensities and hypointensities, respectively, can be observed in the stretched and compressed regions in the corrected images (see Figs. 12f, 13f, and 15d). Consequently, the hyperintensities in such areas do not indicate a false high signal, but a shorter effective echo time. Since the BOLD signal is sensitive to this effect, caution should be exercised in the interpretation of activation in such areas. In areas with hypointensities, the proposed distortion couldn't

correct for the additional signal and sensitivity loss due to phase incoherence within a voxel. However, this method can be combined with other methods, which minimize signal dropouts due to field gradients in the slice selection direction [59,44] or the readout direction [60].

In stretched regions, the current approach is able to determine the PSF shifts with a significantly higher degree of spatial accuracy due to distribution of the PSF across multiple voxels. In the case of compressed regions, a loss of spatial information has already occurred during the EPI measurement and cannot be recovered, even with higher accuracy mapping as previously suggested by PSF mapping in non-distorted spin-warp phase-encoding coordinates [22-27]. Due to strong field inhomogeneity effects, the smoothly varying condition as assumed in Eq. 3.10 is violated in such an area and no unique solution (or no inversion) is available. However, a combined method, which uses both shift maps in the PSF mapping method for distortion correction, can further improve the quality of the correction [61].

The determination of the shift map from PSF acquisitions was discussed in the proposed study. The advantages of the proposed modification were evaluated at a field strength of 7T. In general, distortions are reduced at lower field strength and differences in the correction may be less evident compared to the previously proposed method. It is expected that there are no disadvantages at such lower field strengths.

This approach requires the need for caution in its application in terms of subject motion during the measurements of the PSF data and the EPI scan or time series. As noted by Zaitsev et al. [25], interactions between motion and distortion would be expected. Before distortion correction, motion correction should be accomplished on a simplified assumption that the field inhomogeneity moves with the object. For the correction of motion with higher order effects that changes local distortions, a dynamic update in shift information is required. In the current modification, the correction of static distortions is considered for all images and is accomplished with identical transformations (after motion correction). Therefore, no systematic influences regarding sensitivity and temporal SNR would be expected in fMRI, pMRI and DWI experiments.

3.6 Conclusions

In conclusion, an improved method was developed and tested for accurately determining a shift map from PSF data for use in EPI distortion correction. Instead of the shift map in the non-distorted spin-wrap phase-encoding coordinate, the shift map in the distorted EPI phase-encoding coordinate was newly calculated from the 3D PSF data for a fair comparison of correction performance. Especially, for reducing residual blurring, particularly at the edges of the brain in EPI images, a highly accurate method for the measurement and correction of geometric distortions is proposed. Additionally, the proposed method can be used to remove shift map errors induced by PSF-ghost artifacts. Distortion correction under fully automatic conditions and with a high degree of fidelity was evaluated using phantoms and *in vivo* at 7T. However, a combination study of both shift maps in the PSF mapping method for distortion correction can further improve the quality of the correction [62,61].

4

HIGHLY ACCELERATED EPI-PSF-BASED EPI DISTORTION CORRECTION

In this chapter, an optimal PSF mapping-based distortion correction scheme is introduced which allows higher correction fidelity as well as highly accelerated PSF acquisition. For higher correction quality, a measured PSF-based correction kernel is used directly as a convolution kernel for distortion correction. A non-equidistant sampling scheme is also proposed to greatly accelerate the PSF acquisition without loss of correction quality. The distinct advantages of the proposed approach were demonstrated in phantom and *in vivo* human experiments at 7T.

4.1 Preface

In the previous chapter, it was shown that the PSF mapping method is able to accurately determine both shift maps in non-distorted and distorted phase-encoding coordinates. In 3D *k*-space data obtained from this method, the phase-encoding direction of an object slice is encoded by both conventional EPI and additional spin-warp phase-encoding gradients, which are correspondingly assumed as the distorted and non-distorted coordinates (after 3D Fourier transformation). In general, the PSFs are shifted along the EPI phase-encoding

direction in the spin-warp phase-encoding coordinate due to field inhomogeneity and the deviations are mapped in the non-distorted spin-warp phase-encoding coordinates [22-27]. In the previous chapter, it was demonstrated that an improved correction of geometric distortions in EPI can be achieved with the shift map obtained by PSF mapping in the distorted EPI phase-encoding coordinates.

The single delta approximation of the PSF for calculation of the shift maps in the non-distorted spin-warp [22-27] or distorted EPI phase-encoding coordinates causes differences between two shift maps in the non-distorted and distorted coordinates. Without considering broadening effects of the PSF, only the shifts are measured in these processes and a loss of information about distortion is caused by the delta approximation as shown in Fig. 17. In order to retrieve lost information or improve the correction quality, several interpolation methods such as a sinc interpolation [27], Gaussian process modeling [26] or *b*-spline interpolation [25,45] were proposed previously.

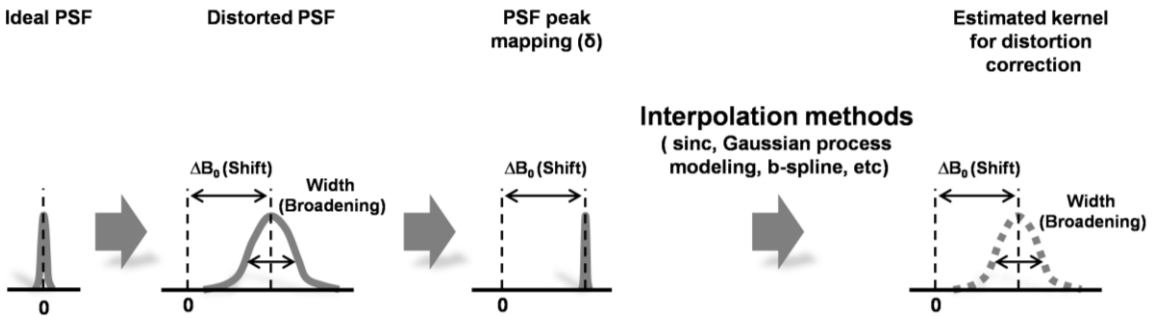

Figure 17: A loss of distortion information due to the single delta approximation of the PSF

The PSF acquisition as a reference scan is very time consuming due to the multi shot nature, in particular for high resolution EPI at UHF. A reduced field of view method combined with partial parallel imaging in the PSF dimension was proposed to minimize the scan time [25]. The acceleration of the PSF acquisition can be carried out by skipping the additional spin-warp phase-encoding gradient step in the PSF dimension whereas the imaging FOV in the PSF dimension (PSF-FOV) is reduced by the acceleration, as show in Fig. 18. Thus, the magnitude of local distortions limited the maximum PSF-FOV reduction due to fold-over artifacts in the shift map. Furthermore, geometric distortions in EPI increase proportional to the strength of the main magnetic field and the maximum

acceleration is generally restricted by a factor of 4 at 7T [44].

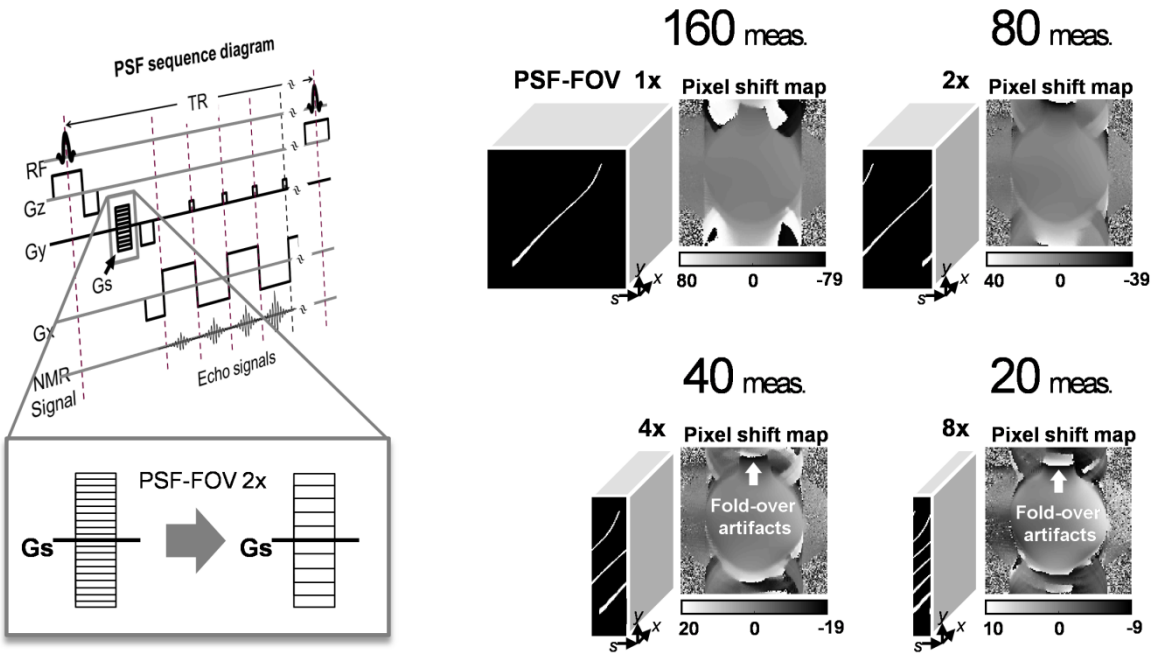

Figure 18: Fold-over artifacts in the shift map due to the PSF-FOV reduction by accelerations.

In this thesis, a method with further improved correction fidelity and highly accelerated PSF acquisition is proposed in order to take the above mentioned considerations into account. (I) In order to improve the distortion correction fidelity, the PSFs are measured in the distorted EPI phase-encoding coordinates and directly used as convolution kernels for distortion correction. Using the convolution kernel, an optimal correction of geometric distortion is achieved, since all information about distortions in a given voxel is represented in the measured PSF data. (II) higher FOV reduction in the PSF dimension is used to acquire the proposed kernel more quickly. Since severe fold-over artifacts in the PSF data is caused by the higher FOV reduction, we propose a new spin-warp phase-encoding and processing scheme for fast PSF acquisition. The proposed results demonstrate the accuracy and efficiency of the proposed method in correcting EPI geometric distortions and in reducing the PSF acquisition and reconstruction time.

4.2 Theory

4.2.1 PSF in the EPI phase-encoding coordinate (EPI-PSF)

A brief repetition of the PSF-based distortion correction theory is followed to derive the proposed PSF. Since it is reasonable to neglect EPI geometric distortions in the readout direction due to its much higher bandwidth than the effects of inhomogeneities in an EPI image, we assume that EPI geometric distortions occur only in the phase-encoding direction. Using Eq. 2.23 in chapter 2 based on the above assumption, the acquired signal of a single shot EPI acquisition including the field inhomogeneity can be summarized as:

$$S(k_y) = \int \rho(r) O(k_y) \exp\left\{ i \left[k_y (r + \frac{\gamma \Delta B(r) T}{\Delta k_y}) \right] \right\} dr \tag{4.1}$$

where $O(k_y)$ is the effective optical transfer function including T2 and T2* relaxation mechanisms and finite sampling [27]. In PSF mapping, a distortion-free phase-encoding direction is added with the additional spin-warp phase-encoding gradients such as the conventional GE imaging. If the PSF dimension is termed as k_s, the signal acquired becomes:

$$S(k_y, k_s) = \int \rho(r) O(k_y) \exp\left\{ i k_y \left[r + \frac{\gamma \Delta B(r) T}{\Delta k_y} \right] \right\} \exp(i k_s r)\, dr. \tag{4.2}$$

Performing inverse Fourier transform of the above equation [22-27] leads to

$$I(y,s) = \rho(s) H(y,s). \tag{4.3}$$

The proton density $\rho(s)$ multiplied with the position-dependent point spread function $H(s,y)$ yields the reconstructed image $I(y,s)$.

$$H(y,s) = \int_{k_y} O(k_y)\exp[ik_y(s-y)]\exp\left\{i\left[\frac{\gamma\Delta B(r)T}{\Delta k_y}\right]\right\}dk_y \quad (4.4)$$

It can be seen from Eq. 4.4 that distortions in the PSF appear as shifts and broadening effects due to the field inhomogeneity. Since the distortions are dependent on *s*, the effects appear along the *s*-direction in the *y*-coordinates. From Eq. 4.3, integration along the *y* and *s* direction yields a non-distorted $I(s)$ and distorted image $I(y)$, respectively.

$$I(s) = \int \rho(s)H(y,s)dy = \rho(s)\int H(y,s)dy \quad (4.5)$$

and

$$I(y) = \int \rho(s)H(y,s)ds = \int I(y,s)ds \quad (4.6)$$

In Eq. 4.2, two dimensions (k_s and k_y) of the 3D *k*-space data set encode the same spatial space and the corresponding coordinates (*s* and *y*) of the 3D PSF data set in Eqs. 4.5 and 4.6 can be referred to as the spin-warp phase-encoding (non-distorted coordinate *s*) and the EPI phase-encoding (distorted coordinate *y*). In an ideal situation without distortions, T2* signal decay, and off-resonance effects, the PSF values would be identical to each other or the delta function in both the spin-warp and EPI phase-encoding coordinates. Given the geometrically correct spin-warp phase-encoding coordinates (*s*) as given in Eq. 4.4, shifts (distortion, off-resonance) and broadening (T2* decay) of the PSF are represented along the EPI phase-encoding coordinates (*y*) given in the spin-warp phase-encoding direction (*s*). This can be transformed into a PSF along the spin-warp phase-encoding direction (*s*) in distorted EPI phase-encoding coordinates (*y*). Namely, the PSF in the spin-warp phase-encoding coordinate acts as a convolution kernel for transforming the GE (non-distorted) image into EPI (distorted) coordinates whereas the corresponding PSF given in EPI phase-encoding coordinates can represent the geometric correction of the distorted EPI. Therefore, the PSF of the EPI image can be derived from Eq. 4.6 based on the hypothesis of time invariance of distortions during the EPI scan time or series.

$$I(y) = \int \left[\int I(y,s)ds \frac{I(y,s)}{\int I(y,s)ds} \right] ds = I(y) \int H_c(y,s)ds \tag{4.7}$$

$$H_c(y,s) = \frac{I(y,s)}{\int I(y,s)ds} \tag{4.8}$$

which is the newly proposed form $H_c(y,s)$, which is calculated by normalization along the spin-warp phase-encoding direction (s) and given in the distorted EPI phase-encoding coordinates (y) as shown in Eq. 4.8. In the following study, it is referred to as EPI-PSF. According to Eq. 4.5, the corrected image $I_c(s)$ is

$$I_c(s) = \int I(y)H_c(y,s)dy = \int I_c(y,s)dy \quad . \tag{4.9}$$

Equation 4.9 indicates that the proposed EPI-PSF $H_c(y,s)$ acts as convolution kernel for un-distortion and can be used directly as a convolution kernel for distortion correction. In contrast, the PSF $H(y,s)$, which was previously proposed [22-27], is considered as a convolution kernel for image distortion as shown in Eq. 4.6. Therefore, unlike the proposed EPI-PSF, the original PSF cannot be directly applied to distortion correction. Also of note is the fact that the shift map in the distorted EPI phase-encoding coordinates [45] can be calculated from the proposed kernel when the center position of the EPI-PSF's peak is considered using the delta-peak approximation. In other words, the interpolation step can be avoided in estimating the correction kernel, since it already contains the entire information about local distortions.

4.2.2 Acceleration of EPI-PSF mapping

The PSF mapping sequence and the acceleration scheme along the k_s-direction are shown in Figs. 19a and 19b, respectively. A linear phase ramp is produced in the k-space data along the PSF dimension (k_s) since the additional gradient G_s for each repetition is linearly altered for PSF encoding. In an image space with a fully encoded k_s-dimension, an

increment of the phase difference across the full FOV for one PSF encoding step is 2 pi. By increasing the spacing for each PSF encoding step, the corresponding PSF-FOV in the *s*-direction is effectively reduced (see Fig. 18b). Since the entire FOV of the object is typically lager than the maximum distortion, the total PSF encoding steps in k_s can be reduced by increasing the sampling distance [25]. However, if the reduced PSF-FOV is smaller than the distortion strength, a reconstructed PSF data with severe fold-over artifacts can be generated due to higher PSF-FOV reduction corresponding to wider k_s-spacing in the PSF dimension. Furthermore, these artifacts are typically increased at UHF. An unfolding procedure is required to use the measured EPI-PSF samples as a convolution kernel for distortion correction (see Fig. 20). A non-equidistant PSF encoding scheme is newly proposed to calculate a shift map without folding effects in the EPI-PSF. As shown in Fig. 19b, a severely wrapped line is obtained by a linear fit of the phase along the PSF dimension due to higher PSF-FOV reduction. This corresponds to the highly reduced PSF-FOV in the *s*-coordinate which potentially generates a shift map with severe fold-over artifacts. By adding a few additional closely spaced PSF samples around the k_s-space center, a linear fit of the phase along the PSF dimension allows calculation of a non-wrapped line corresponding to the shift map without fold-over artifacts, since the additional closely spaced samples resolve phase ambiguities. In order to select the correct replica of the folded EPI-PSF, the shift map without fold-over artifacts is applied in the proposed method.

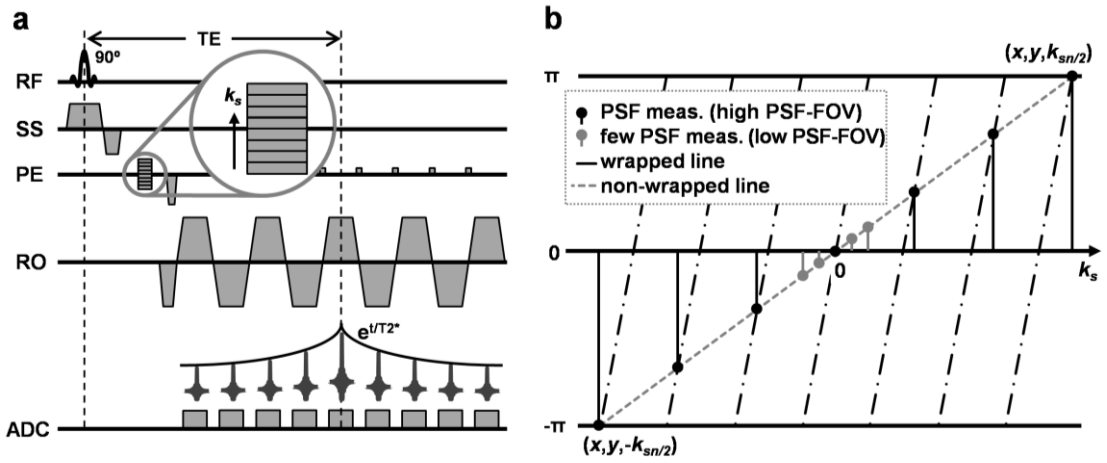

Figure 19: PSF mapping sequence (a) and the accelerated sampling scheme along the k_s-dimension (b). The few extra closely spaced PSF samples around the k_s-space center supplement the widely spaced PSF samples (corresponding to a reduced PSF-FOV in the *s*-coordinate).

4.3 Materials and Methods

4.3.1 Experimental parameters

Phantom and human *in vivo* experiments were carried out on a 7T whole body MRI (Siemens Healthcare, Erlangen, Germany) using an 8 channel head coil (RAPID Biomedical, Würzburg, Germany) or a 24 element phase array coil (Nova Medical, Wilmington MA, USA), respectively. In both experiments, 12 axial slices were acquired. As described by Zaitsev et al. [25], conventional gradient-echo EPI and corresponding PSF sequences were applied for data acquisition. The following experimental parameters were applied for phantom data acquisition: TR/TE = 1000/26 ms, matrix = 160×160, FOV = 224×224 mm^2, slice thickness = 1.4 mm, Grappa factor = 2, partial Fourier = 6/8, and echo spacing = 0.76 ms. In *in vivo* human imaging, the same parameters except echo spacing = 1.0 ms were used. The PSF data with full PSF encoding steps (160 k_s-lines in the PSF dimension) were measured to test the proposed accelerations of the PSF acquisition.

4.3.2 Processing procedures

Figure 20 shows the proposed reconstruction flowchart for obtaining the distortion correction kernel and correcting geometric distortions in EPI using the distortion correction kernel. A 3D inverse FFT of the PSF raw data subset with high FOV reduction is employed to measure the EPI-PSF $H_c(y,s)$ with potential fold-over artifacts in the 3D PSF space. Separately, after 2D inverse FFT in k_x and k_y of the complete non-equidistant PSF acquisition data, phase fitting along the k_s dimension is followed in order to obtain a shift value of the EPI-PSF without fold-over artifacts in the EPI phase-encoding coordinates (y). A phase fitting method proposed by Ahn et al. [15] was used to determine accurate subvoxel shifts as described in the previous chapter 3. Since only the peak positions of the EPI-PSF are contained in this shift map, it is possible to collect the EPI-PSF samples without the fold-over effects. As a convolution kernel for distortion correction in a given voxel, the six magnitude EPI-PSF samples closest to the position of the EPI-PSF peak are selected along the spin-warp phase-encoding direction in the distorted EPI phase-encoding coordinates. The EPI-PSF information is not available outside of the brain mask. Therefore,

a weighted linear extrapolation is performed using the peak position information from the shift map at the boundary of the mask areas. As mentioned in the chapter 3, the *b*-spline interpolation method is used to estimate the EPI-PSF (or the convolution kernel) in these areas outside the mask. According to Eq. 4.8, the collected and estimated EPI-PSF samples are normalized and finally form the proposed kernel for un-distortion. Using the kernel, distortion correction is accomplished by one-dimensional resampling (along the phase-encoding coordinate *y*) as given in Eq. 4.9. All reconstruction processes are implemented in the Matlab (Mathworks, Natick, MA) environment.

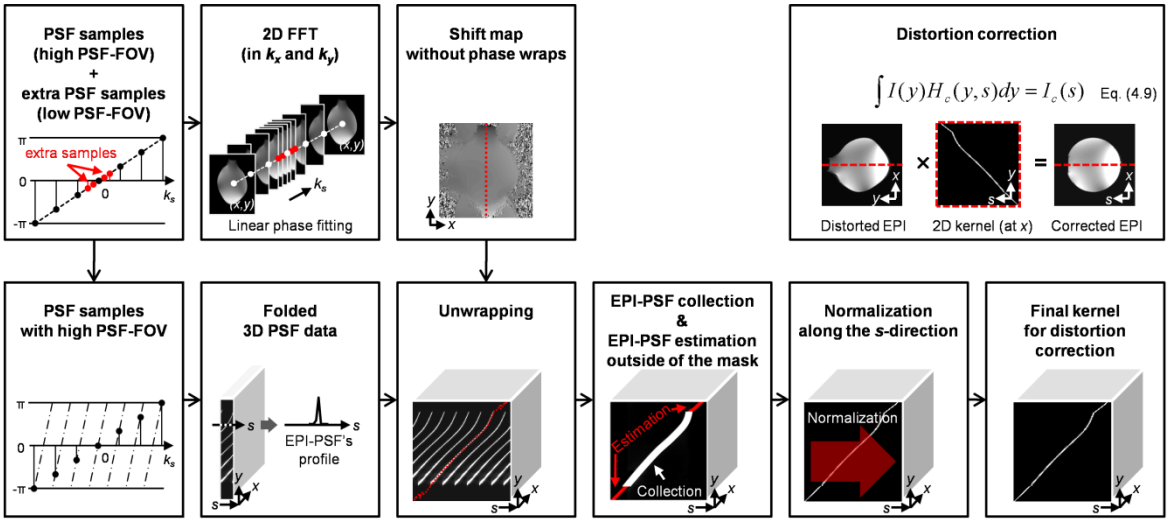

Figure 20: The proposed reconstruction flowchart resulting in a convolution kernel for distortion correction and the distortion correction scheme by the convolution kernel. The single steps are illustrated with a graphical example from a phantom data set.

4.3.3 Additional measurements for robust unwrapping

For robust unwrapping of the folded 3D PSF data as the result of higher acceleration, a reliable shift map without fold-over artifacts is required in the proposed method. In order to search for the minimum requirement for the number of additional PSF samples, two reductions are combined into the proposed shift map calculation. PSF-FOV reductions are first applied with acceleration factors of 1, 2, 4, 8, 16, and 32. The remaining PSF samples

by PSF-FOV reductions are further eliminated from outer PSF samples up to the final 2 PSF samples in the center of the k_s-dimension. With the corresponding PSF samples extracted from the full PSF data, the shift map calculation is performed in order to evaluate the reliability of the shift maps with reductions. The shift maps with reductions are compared with the shift map with full PSF acquisition. Three differences including the mean, standard deviation, and maximum are calculated in the mask areas. Since severe fold-over artifacts are measured for higher PSF-FOV reduction, the differences are calculated after unwrapping using the shift map with full PSF acquisition.

4.3.4 Comparison of correction quality between accelerations

In order to compare the correction quality of the distortion corrected results with the proposed accelerations, the proposed kernel was calculated based on the corresponding PSF encoding steps extracted from the full PSF data. Acceleration factors of 1, 2, 4, 8, and 16 were tested for the PSF-FOV reduction. Fold-over artifacts were not visible with a PSF-FOV reduction of 2. For more than factors of 2, only four dense center *k*-space PSF encoding steps with a *k*-space line spacing factor of 2 were used to resolve the fold-over artifacts, as shown in Fig. 22b. To evaluate the distortion corrected results with the proposed accelerations, the result without acceleration or a reference image were used as a standard for comparison. According to Eq. 4.5, a non-distorted image was obtained as the reference image. In order to avoid signal dropouts caused by the integration due to intravoxel dephasing, the calculation was applied to the magnitude instead of the complex 3D PSF data. Additionally, a partial Fourier PSF data set was extracted with factors of 5/8, 6/8, 7/8, and 8/8 in order to access the further acceleration effects caused by asymmetric sampling in the PSF dimension. The missing *k*-space data were filled with zeros prior to the reconstruction.

4.3.5 Comparison of correction quality between interpolation methods

Interpolation methods based on the shift map, a *b*-spline interpolation method [45] and a Fourier method [63], were applied for distortion correction and compared with the proposed method. In the *b*-spline interpolation and Fourier methods, the shift map in the

EPI phase-encoding coordinates, which was calculated from a full PSF acquisition, was used for the correction. For the Fourier method [63], a non-uniform fast Fourier transform (NUFFT) algorithm implemented by Ferrara et al. [64] in Matlab was applied as an interpolation method. All methods were performed using both phantom and *in vivo* data.

4.4 Results

Figure 21 provides information on the differences between the shift maps with full and accelerated PSF acquisitions in phantom (I) and *in vivo* human experiments (II). Three difference values in the mask regions, indicate difference (top), standard deviation (middle), and maximum difference (bottom). In the phantom results, compared to full PSF samples, very small mean differences were detected, even for 2 PSF samples, as shown in Fig 21I. In addition, the standard deviation shows that the differences in the mask areas are very homogeneous. Compared to the phantom results, relatively larger differences were observed with the reductions in the human experiment (Fig 21II). In both phantom and human results, the differences caused by PSF-FOV reductions are usually very small, even for a very high PSF-FOV reduction factor of 32 when the difference is calculated after resolving the fold-over artifacts in the shift map. In further reductions eliminating the outer PSF samples, the differences are maintained up to almost half the elimination of the outer PSF samples. The differences increase progressively in accordance with the reduction of the PSF samples by more than half and then rapidly increase when the PSF samples are less than 5 in the center of the k_s-dimension. These results demonstrate that more than 4 additional PSF samples in the center of the k_s-dimension and a maximum PSF-FOV reduction are needed to produce a shift map without the fold-over artifacts, to achieve a robust unfolding process in the proposed scheme.

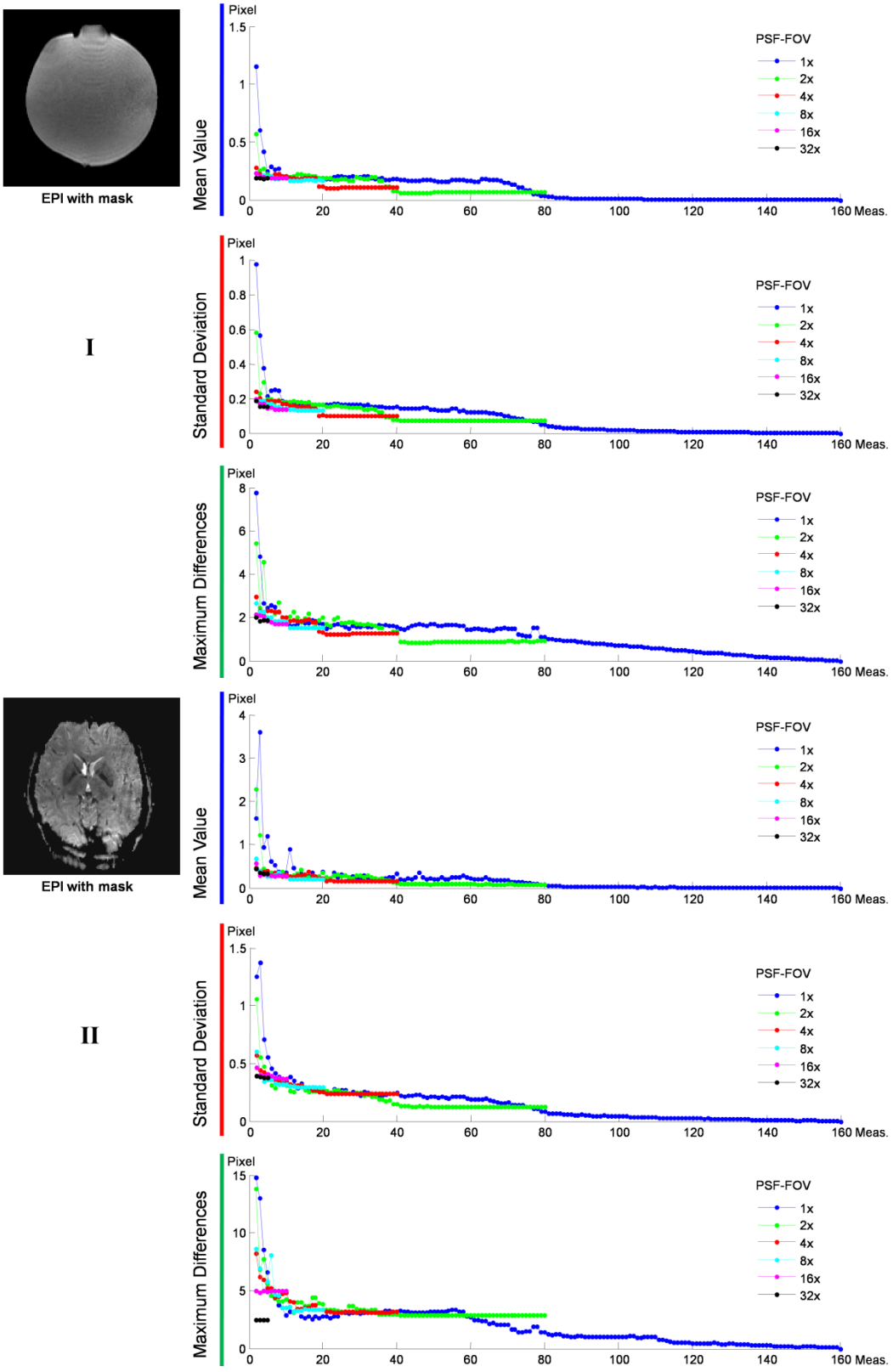

Figure 21: Shift map differences between the shift maps with accelerations and full acquisition in the mask region. In the mask region, three types of differences (mean, standard deviation, and maximum differences) were calculated in phantom (I) and human brain (II) experiments.

Figure 22 shows that a shift map with severe fold-over artifacts can be resolved by the proposed method, even at the high PSF-FOV reduction. A PSF-FOV reduction of 8 was used for the PSF acquisition and severe fold-over artifacts in the shift map can be seen in Fig. 22a. The EPI-PSF peak with severe fold-over artifacts is represented as the shift map. The proposed PSF acquisition scheme was obtained by adding four extra PSF acquisitions with a PSF-FOV reduction of 2 and yielded a shift map that contained no fold-over artifacts (Fig. 22b). In Fig. 22b, strong geometric distortions between -26.76 and 19.04 pixel shifts (corresponding to -3.75 and 2.67 cm) were observed within the mask areas of the brain. This indicates that a PSF-FOV reduction of 2 can be used as a standard for the extra PSF acquisitions while still covering the strength of distortions.

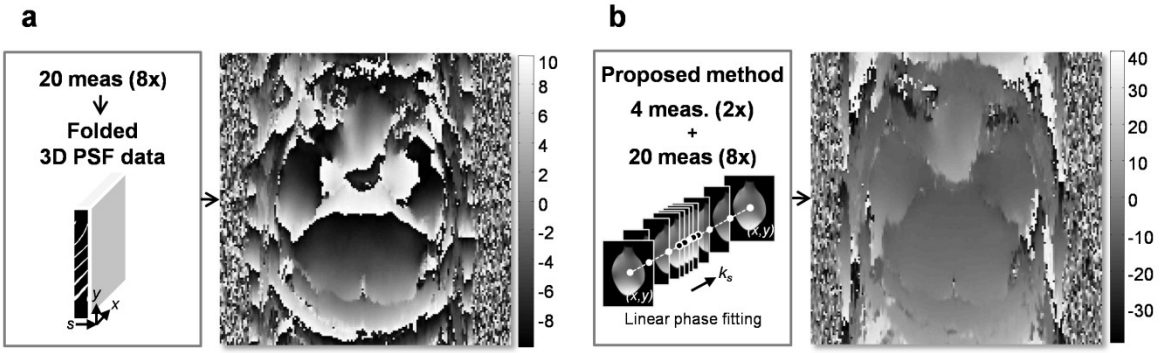

Figure 22: The shift map with (a) and without (b) fold-over artifacts calculated from the PSF acquisition with a PSF-FOV reduction of 8 and the proposed non-equidistant PSF acquisition, respectively.

Figure 23 demonstrates that the PSF-FOV reductions result in no noticeable change in the proposed EPI-PSF profile. In the 3D PSF space, the EPI-PSF profiles along the spin-warp phase-encoding direction (*s*) were measured with different PSF-FOV reductions and compared at three different positions in the distorted EPI image of a phantom (Fig. 23I) a human brain (Fig. 23II) with stretched (Fig. 23i), compressed (Fig. 23ii), and non-distorted voxles (Fig. 23iii). To access the differences visually, the measured profiles were normalized by their largest value. In the stretched and non-distorted regions, the PSF-FOV reductions result in no detectable degradation of the EPI-PSF profile (Figs. 23i and Fig. 23iii). Only in the strongly compressed region of the human brain, high factors of the PSF-FOV reduction increase slight degradations of the profile of the EPI-PSF (Fig. 23II-ii).

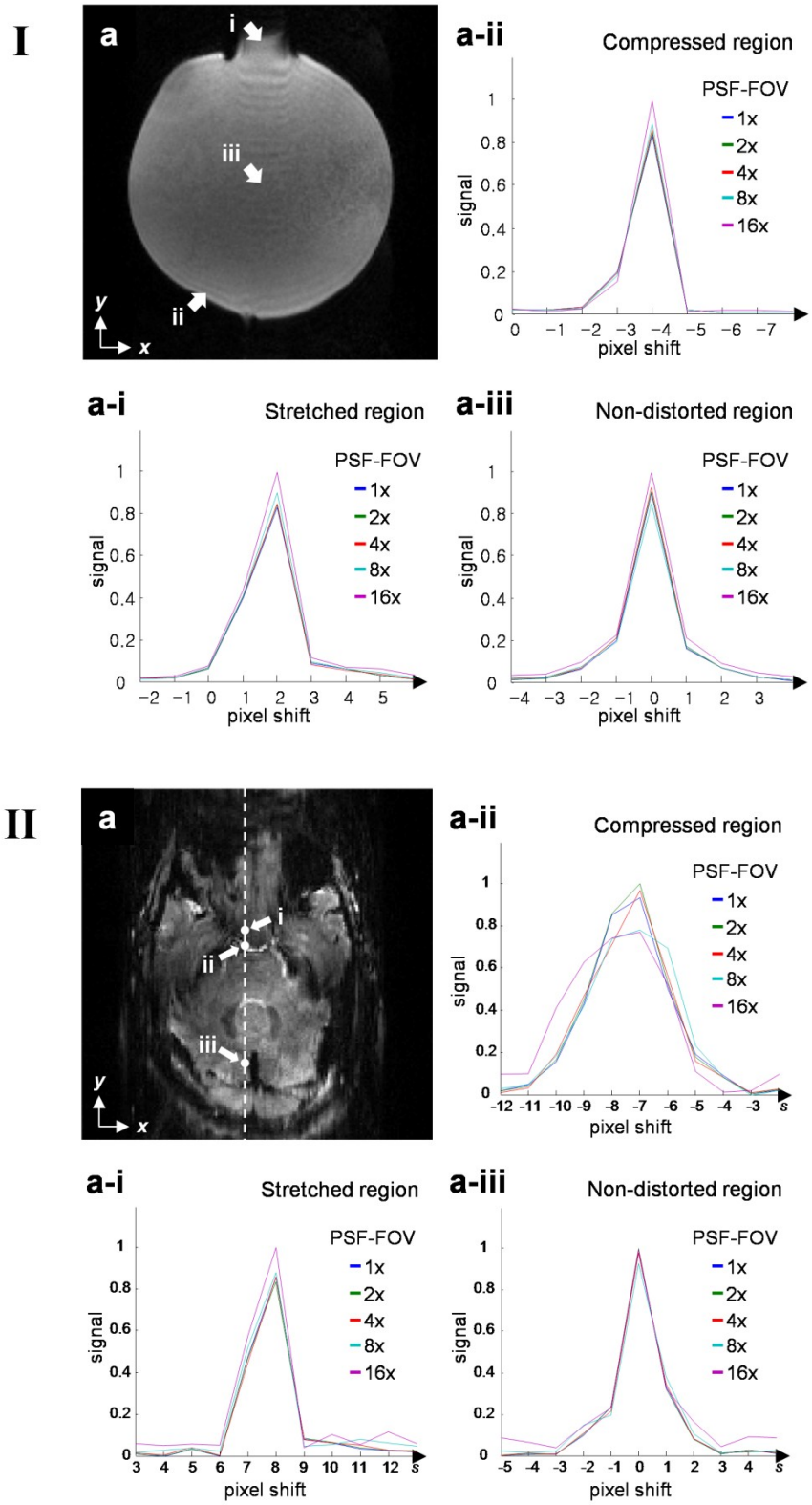

Figure 23: EPI-PSF profiles with different PSF-FOV reductions in the 3D PSF space (x,y,s) corresponding to three different regions: stretched (a-i), compressed (a-ii), and non-distorted region (a-iii), in a distorted EPI image (a) of the phantom (I) and a human brain (II).

Figure 24 presents the distortion corrected results with different PSF-FOV accelerations in a phantom (Fig. 24I) and a human brain (Fig. 24II). All distortion corrected images with PSF-FOV reductions of 2 (Fig. 24d), 4 (Fig. 24e), 8 (Fig. 24f), and 16 (Fig. 24g) are nearly equivalent to the results obtained with full PSF acquisition (Fig. 24c). The geometry of all distortion corrected results is in good agreement with the non-distorted reference image (Fig. 24b). This demonstrates that the proposed distortion corrections perform very well despite the very high PSF-FOV acceleration of up to 16 as well as even in the case of strong geometric distortions in a human brain image.

Geometric agreement with the geometrically correct reference image before and after geometric distortion correction is presented in Fig. 25. A very high PSF-FOV reduction of 16 was used for this correction. As shown in Figs. 25b-i and 25b-ii, significant improvements were achieved at the boundary of the brain. In particular, the geometry of the distortion corrected images is almost identical to the reference image (Figs. 25c-i and 25c-ii). The proposed method failed to recover only the effect of either distortion or signal dropout due to intravoxel dephasing within a voxel (see arrow in Fig 25b-ii).

Figure 26 shows a comparison of the results corrected by three different interpolation methods, the Fourier method (Fig. 26e), the *b*-spline interpolation method (Fig. 26f), and the proposed method (Figs. 26c and 26d). In order to focus on the quality of the correction, a slice containing largest brain region was selected for comparison. Geometric distortions can be corrected by all methods effectively. However, rippling artifacts [27] yielded by the Fourier method were seen at the boundary region of the brain (Fig. 26II-e) and some image blurring was introduced by the *b*-spline interpolation method (Fig. 26II-f). It was not possible to eliminate these artifacts, even with the shift map with full PSF encodings along the PSF dimension. In contrast, accurate geometric correction without suffering these drawbacks was achieved using the proposed method with a PSF-FOV reduction of 16 plus 4 additional center k_s-lines and resulted in the appearance of a visually sharper image (Fig. 26II-c). A slight reduction in resolution is produced with an asymmetric PSF acquisition of 6/8 applied in the PSF dimension (Fig. 26II-d).

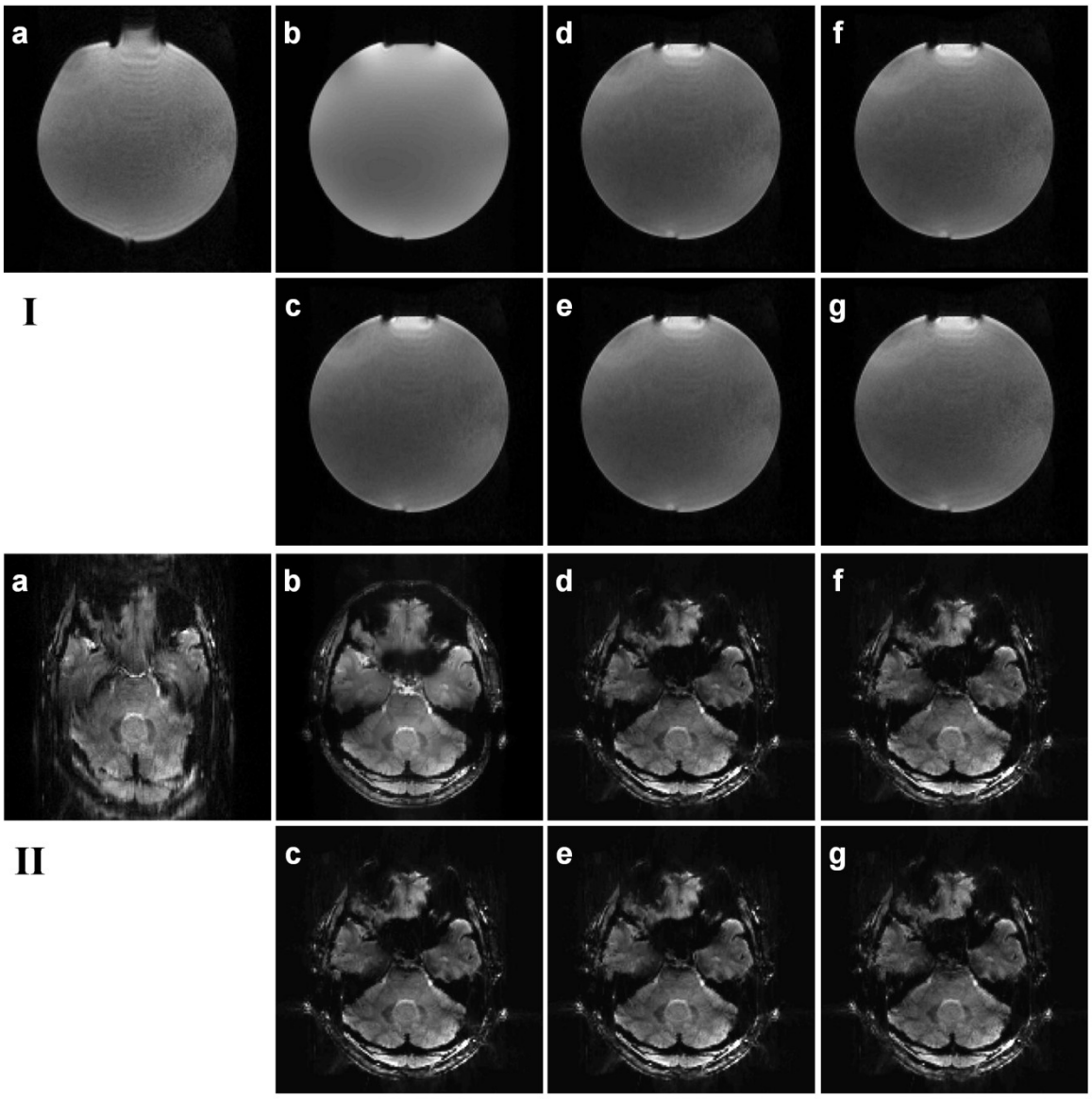

Figure 24: The distortion corrected results with different FOV reductions in a phantom (I) and an *in vivo* example (II): (a) Distorted EPI image, (b) reference image, and distortion corrected results without reduction (c) and with the FOV reductions of 2 (d), 4 (e), 8 (f), and 16 (g) are shown. All results with reductions (d-g) are identical to the result without reduction (c) and a clear brain and skull depiction with equal quality even for very high acceleration is achieved.

Figure 25: The geometric agreement of the distortion corrected image of the human brain: (a) Distorted EPI image, (b) corrected EPI image, and (c) reference image. To access the geometric fidelity more clearly, two enlarged sections of the anterior (middle column) and posterior regions (right column) of the full FOV image (left column) are shown. The red contours calculated from the reference image (c) were overlaid onto the enlarged EPI images (middle and right column).

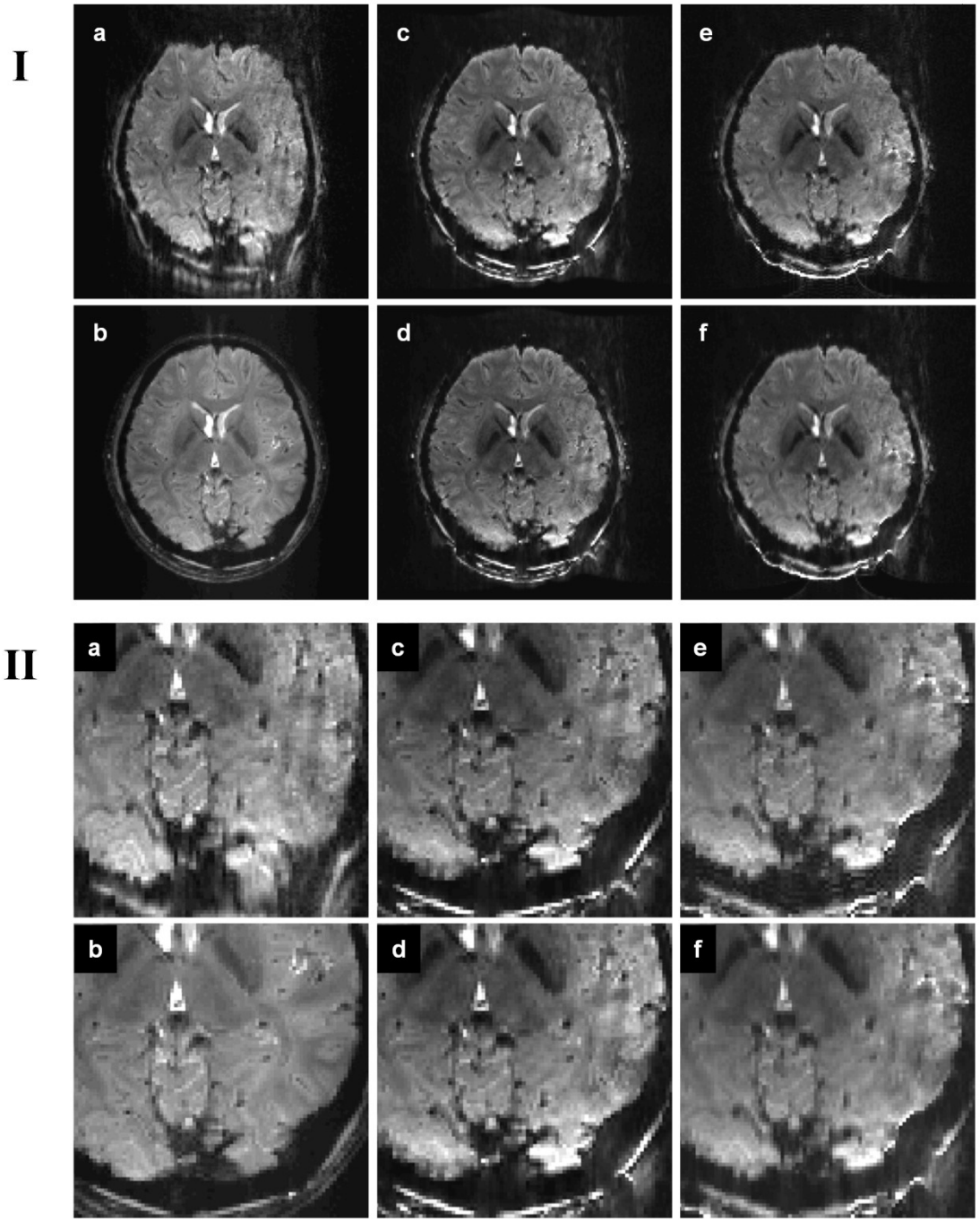

Figure 26: Comparison of the correction quality caused by the interpolation methods, the proposed method, and the proposed method with partial Fourier PSF acquisition in full FOV images (I) and the enlarged images of the small portion of the brain region (II): (a) Distorted EPI image, (b) reference image, two distortion corrected results by the proposed method without (c) and with asymmetric PSF sampling of 6/8 (d), and two distortion corrected images based on the Fourier interpolation method (e) and the b-spline interpolation method (f). A FOV reduction of 16 was applied for the results of (c) and (d). The full PSF data were exploited for (e) and (f).

4.5 Discussion

In this study, it is demonstrated that the correction quality of geometric distortions in EPI can be further improved via the use of the proposed EPI-PSF based convolution kernel. As a convolution kernel for distortion correction, the EPI-PSF in the 3D PSF data, which contains information about all geometric distortions, is collected along the non-distorted spin-warp phase-encoding direction (in the distorted EPI phase-encoding coordinates). Therefore, the proposed method can accurately correct geometric distortions in EPI, even in areas with strong geometric distortions at UHF such as 7T. It has been previously demonstrated that EPI geometric distortions can be recovered via the use of several different interpolation methods based on shift maps in the spin-warp [22-27] and EPI phase-encoding coordinates [45]. However, there are still some limitations to estimating an optimal kernel for distortion correction since a loss of information about distortions is commonly caused by the delta-peak approximation of the PSF (represented as a single shift value for each voxel). As an extension of the single delta approximation, the measured EPI-PSF is considered in this study and can avoid such information loss. However, it is difficult to quantitatively evaluate the remaining distortion errors, due to the absence of an established quantification and gold standard metric. Thus, the contribution of this study depends on a detailed visual examination and comparison of the image appearance.

PSF-FOV variations do not cause a noticeable change in the profile of the EPI-PSF and can thus be reduced to the width of the EPI-PSF. In other words, a significantly reduced scan time for the PSF reference acquisition is possible with the proposed non-equidistant acquisition and processing scheme. Since the PSF-FOV reduction is limited by a factor of 2 due to strong geometric distortions in our experiments at 7T, at least 80 PSF acquisitions were required in order to obtain a shift map without fold-over artifacts and resulted in a 4-min scan time for a TR of 3 sec. In contrast, the proposed method had reduced the scan time down to 42 sec since only 14 PSF acquisitions were required with a PSF-FOV reduction of 16. Only in the strongly compressed areas, the width of the EPI-PSF profile may be larger than the six samples chosen in the proposed method since more than 6 pixels could be compressed into a pixel. However, very minor correction differences are usually caused by the selection in the proposed method due to strong signal losses in such affected areas. In general, if the width of the EPI-PSF profile is wider than the remaining PSF-FOV,

unsolvable fold-over of the EPI-PSF itself can occur.

As an additional benefit, the acceleration of the PSF acquisition allows a faster reconstruction, due to smaller data size. In the PSF mapping method, a three dimensional FFT is required to obtain a 3D PSF data and is generally time consuming. When the phantom dataset used in this study was reconstructed in Matlab on an Intel Core 2 PC, the computation time with a PSF-FOV reduction of 8 was 18 sec compared to 40 sec for a PSF-FOV reduction of 2. No differences in reconstruction quality were found for kernel sized up to 10. Only the calculation time was increased.

Only four densely spaced center *k*-space PSF acquisitions allow a successful unwrapping of the EPI-PSF. Furthermore, the unwrapping is carried out very quickly since only the shifted replica of the EPI-PSF peak is selected correctly using the shift map without fold-over artifacts. Therefore, a robust, fast, and automatic unwrapping performance is maintained by the proposed method. To solve the fold-over artifacts in the shift map, a standard unwrapping algorithm [65-67] could also be applied without any additional PSF acquisitions. However, such algorithms usually perform well only on continuous areas. The unwrapping process often fails in regions with low signal-to-noise ratio (SNR) due to the higher sensitivity to noise, and the unwrapping errors in those regions can propagate into areas with high SNR [68].

A GRAPPA reconstruction [25] may also be applied to the proposed PSF acquisition scheme and would result in the EPI-PSF data without fold-over artifacts. However, noise enhancement in the 3D PSF data could be a problem due to high acceleration factors not supported by the coil geometry. Although such data may not be appropriate to directly correct distortions due to its low SNR, they could be suited for the unwrapping of the EPI-PSF. In contrast, no noise amplification is produced in the measured PSF data even with high PSF-FOV reduction as shown in Fig. 23. Moreover, the proposed method is suitable also for single coil acquisitions that do not support parallel imaging.

The proposed method can avoid collecting PSF-ghost artifacts from the 3D PSF data into the proposed kernel for distortion correction. In general, PSF-ghost artifacts appear as shifted signals along the spin-warp phase-encoding direction of the PSF data. As mentioned the previous chapter, since oscillatory motion, such as with CSF pulsation, cardiac motion, and respiratory motion, can be a dominant source of PSF-ghosting artifacts by combinations of effects, both signal variations and large k_s-shifts (relative to the k_y-

encoding), the artifacts rely on the PSF acquisition time and are independent of the reduction of PSF-FOV. Since only 6 EPI-PSF samples at closest to the EPI-PSF peak are collected and the collection is performed along the spin-warp phase-encoding direction in the EPI phase-encoding coordinate, the artifacts can be reduced in the proposed EPI-PSF collection process. Moreover, the artifacts could be decreased at higher PSF-FOV reduction since the effects of pulsatile flow or motions, which strongly affect the artifacts, are significantly reduced due to relatively short PSF acquisition time.

The sharpness of the distortion corrected image relies on the asymmetric sampling in the PSF dimension and is independent from the PSF-FOV reduction. As shown in Figs. 26c and 26d, blurring effects of the measured PSF data are introduced by an asymmetric sampling in the PSF dimension due to the use of zero-filling. Although asymmetric sampling could accelerate the PSF acquisition further, the reduction would be small in the case of high PSF-FOV reduction. However, the correction quality may be improved by investigating an optimal partial Fourier reconstruction of the 3D PSF data to minimize the blurring effects.

The proposed method can correct distortions very well in stretched areas. In addition, loss of spatial information in compressed areas can be partially recovered, due to the use of the complete EPI-PSF rather than only its peak information. Only in strongly compressed areas where strong signal loss may occur and multiple pixels could collapse, the proposed method couldn't recover the distortions appearing as signal losses (see Fig. 25). However, spatial information cannot be recovered, even by further improved mapping of the PSF since it has already been lost during the EPI acquisition process.

4.6 Conclusion

An EPI-PSF-based convolution kernel for EPI distortion correction has been introduced. Higher acceleration of the PSF acquisition in the PSF dimension is also proposed in order to accelerate the acquisition of the proposed kernel. The PSF-FOV reduction is combined with a non-equidistant PSF sampling pattern. The results demonstrate that EPI geometric distortions can be corrected in a very robust manner and without loss of correction fidelity despite the highly accelerated PSF acquisition. The advantages for the correction of EPI geometric distortions are demonstrated in phantom and human brain experiments at 7 Tesla.

5

SUMMARY AND FUTURE WORK

5.1 Summary

5.1.1 Shift maps in non-distorted and distorted coordinates

To date, many studies [13,15,22,24-28,44,45] have shown that geometric distortions in EPI can be effectively corrected using shift maps in non-distorted or distorted coordinates. In general, shift maps in such non-distorted and distorted coordinates are calculated from different images, such as GE and EPI, and it is not possible to easily compare them under identical conditions. In addition, a reliable shift map calculation is required since errors in the shift map directly affect the correction quality.

Taking the above into consideration, a modified PSF mapping method is proposed. Although the PSF mapping method can reliably detect geometric distortions in EPI, only the shift map in the non-distorted coordinate is calculated by the method [22-27]. In the proposed method, PSF mapping is processed in the distorted (EPI) phase-encoding coordinates instead of the non-distorted (spin-warp) phase-encoding coordinates as suggested previously [22-27]. To measure the PSF peak mapping more accurately, a phase fitting method proposed by Ahn et al. [46] is used for calculating both shift maps in non-distorted and distorted coordinates. This allows peak information to be directly obtained,

without searching the peak position of the magnitude in a subsequent analysis.

PSF and EPI data were acquired at 7 Tesla. From the 3D PSF data the proposed shift map was calculated as described by Zaitsev et al. [25] with four modifications including the phase correction of the 3D PSF data, the shift map calculation scheme, the mask generation, and the distortion correction scheme based on the proposed shift map. An evaluation study is performed by comparing the distortion corrected results determined by the modified and original method in phantom and *in vivo* data at 7T.

The proposed modification allows determination of the local shift with higher spatial accuracy due to the distribution across multiple voxels in case of local stretching and leads to an improved correction quality. In compressed regions, spatial information has already been lost in the EPI acquisition process and cannot be recovered even with higher accuracy mapping as potentially offered by PSF mapping in the non-distorted spin-warp phase-encoding coordinate [22-27]. In addition, flow artifacts can strongly affect the distortion correction in human imaging and only the proposed shift determination can avoid these flows induced PSF-ghost artifacts in the shift map.

The shift map in the distorted coordinate, which can be obtained by the modified PSF mapping method, allows a correction of the geometric and intensity distortions in EPI with high accuracy and reduction of blurring. In addition, the modified shift determination effectively removes flow induced ghost artifacts in the shift map.

5.1.2 Accelerated EPI-PSF-based EPI distortion correction

The single delta approximation of the PSF in the shift map calculation causes a loss of information regarding distortions. In addition, the PSF reference acquisition can be time consuming due to its multi-shot nature. Under the above considerations, this study presents an improved PSF mapping-based distortion correction method, which allows very accurate correction quality as well as highly accelerated PSF acquisition without any loss of correction quality or reliability compared to full PSF acquisition.

In this study, PSF mapping in the distorted EPI phase-encoding coordinate, which is referred as EPI-PSF, is performed and the measured EPI-PSF is used directly as a convolution kernel to correct for distortion instead of shift map-based correction methods,

which are introduced in the chapter 3. It can be seen that the shift map in the distorted coordinates is obtained when only the proposed EPI-PSF peak is considered, and the proposed EPI-PSF contains complete information concerning distortions. Thus, the proposed method allows improved correction fidelity compared to shift map-based correction methods described in chapter 3.

In order to highly accelerate the PSF acquisition, a reduced FOV technique [58] in the PSF dimension (PSF-FOV) is adapted in the proposed method as previously suggested by Zaitsev et al. [25]. In general, a high PSF-FOV reduction causes severe PSF folding artifacts in the reconstructed 3D PSF data and an unfolding process is required. To solve this problem, a non-equidistant PSF acquisition scheme is newly suggested in the proposed method. It is demonstrated that a successful unwrapping of the EPI-PSF is possible by adding four, additional densely spaced center *k*-space PSF samples to the PSF acquisition with a very high PSF-FOV reduction. Since the shape of the EPI-PSF to be used as a convolution kernel for distortion correction is usually maintained despite a very high PSF-FOV reduction, there is no loss of the correction quality in the proposed acceleration scheme.

Conventional gradient-echo EPI and corresponding PSF data with fully sampled PSF data sets of phantoms and healthy volunteers were acquired at 7 Tesla (Siemens Healthcare, Erlangen, Germany) in order to simulate the proposed correction and accelerations. The distortion corrected results with the proposed method were compared to result with full encoding or the reference image. Interpolation methods based on shift maps in the distorted EPI phase-encoding coordinate, non-uniform Fourier transformation [64,63] and a *b*-spline interpolation [45] were compared with the proposed method.

The results demonstrate that the proposed method corrects geometric distortions in EPI with high accuracy and quality despite the high acceleration. Therefore, the proposed EPI-PSF-based distortion correction improves a correction of EPI and accelerates PSF reference data acquisition.

5.2 Suggestions for Future Work

5.2.1 Distortion correction for DTI applications

Diffusion tensor imaging (DTI) is a promising application of diffusion weighted imaging (DWI) which permits molecular diffusion to be directly observed in tissues, and thus probes structures on a microscopic scale. It is frequently applied in neuroscientific studies of brain structure and connectivity as well as in clinical imaging of various pathologies, such as strokes or neurodegenerative diseases. Since single-shot or multi-shot EPI is generally the method of choice for a number of DTI applications, it suffers severely from distortions due to B0 field inhomogeneity, susceptibility, as well as eddy current effects. These artifacts cause geometric and intensity distortions in diffusion image formation. These distortions, furthermore, vary according to the diffusion encoding direction due to eddy current effects. In general, eddy currents are generated by substantial, rapid changes in the magnetic field associated with the switching of magnetic field gradients, and produce unwanted gradients, depending on the direction of diffusion-weighting gradients. While current EPI distortion correction methods can be applied to DTI, they only correct for gross distortions caused by object susceptibility. The direction-dependent distortions, which appear more prominently at higher magnetic field, cause misregistration between DWI images that becomes a major difficulty for reliable analysis and interpretation e.g. of fiber tracks.

Based on previously proposed methods, several modified approaches involving field maps [69-71], two images with reversed phase-encoding directions [72-74] or with reversed diffusion weight directions [75], and coregistration methods with various post-processing algorithms [76-78] have been adapted to correct for distortions in EPI-based DWI. However, the multi-reference scan based field map techniques cannot measure all directional distortions accurately due to the exceedingly long acquisition time, and image-based coregistration methods have a potential difficulty with reference to robust and accurate co-registration, since the contrasts of DWI images are direction dependent. In other words, only general distortions induced by field inhomogeneites, but not the direction dependent distortions, can be accurately corrected by the approaches mentioned above. Furthermore, none of these methods allows a reliable correction of distortions where

several voxels are compressed into one. In general, spatial information in compressed regions has already been lost in the acquisition process. Therefore, even with a well-estimated field map or shift map with an ability to resample the distorted DWI images back to the true voxel locations, this loss of spatial information cannot be recovered with image-based resampling alone. Alternatively, an attempt to combine two images with reversed phase-encoding directions leading to opposite image distortions has been introduced in order to overcome the loss of spatial resolution due to such compression [79]. In this method, a weighted combination between the two distortion corrected images is performed by the Jacobian modulation function based on the underlying concept that information in stretched regions is more reliable than in compressed regions. However, there are still challenges in terms of how to obtain a precise field map and how to combine two images more reliably.

All of the previously proposed methods focus on a single or several distortion inducing factors in EPI-based DWI. Up to date, only few attempts have been made to avoid all distortions in EPI-based DWI, which would allow correction for static and eddy-current induced effects including recovery of information in strongly compressed regions.

Although the PSF mapping method allows an optimal correction of all distortions, the reference data based methods are very time consuming when repeated for every diffusion-encoding direction. As demonstrated in chapter 4, a PSF mapping-based method with further improved correction quality and highly accelerated PSF acquisition has been developed. The results show that the proposed method allows a robust and optimal correction of geometric distortions in EPI without the loss of quality, despite the high acceleration of the PSF data acquisition. Therefore, it opens a possibility for allowing non-distorted DWI if the proposed acceleration scheme is adapted for correcting geometric distortions in DWI images. A first attempt at phantom imaging was undertaken recently to correct distortions in EPI-based DWI and this effort demonstrated the potential advantages of the proposed scheme [80]. However, this has not been demonstrated *in vivo* and further developments and optimizations for phantoms as well as *in vivo* imaging are still required in order to improve the quality and performance of the proposed scheme. In other words, continuous efforts for optimizing the DWI distortion correction scheme focusing on the scan time and reconstruction quality will be required.

5.2.2 Dynamic distortion correction

In practical applications, an important issue regarding distortion correction in EPI is dynamic effects during the scan time. Although global off-resonance effects are generally constant over experimental time series, this assumption fails when sensitive phase data due to small scale changes associated with off-resonance effects caused by the physiological influences are being considered [81-83]. It is well recognized that head motion severely degrades the accuracy of fMRI exams [84,85]. In addition, time varying distortions are caused by the interaction between motion and distortion and these effects may manifest themselves as apparent noise in the fMRI time series as reported by Jezzard and Clare [86]. Therefore, a combined approach including both dynamic motion and distortion correction should be considered for future studies.

To date, several methods have been developed to consider various types of dynamic behavior, which include zero-order field offset correction using navigator echoes [87-90] and 2D field dynamic correction by estimating the field variation map [83,91]. Due to the limited knowledge of additional signals, however, the former methods can correct only simple and reproducible artifacts such as dynamic phase discontinuities [88], magnetic field drift [89], or breathing motion artifacts [90]. In order to correct more complex field variations, a static field map [91] or a reference image [83] was proposed and was used to calculate field variations at each image series. In general, the static field map requires a phase unwrapping process as an additional procedure whereas a reference image for dynamic distortion correction is available after finishing the entire measurement since it is obtained by average over whole measurements.

Prospective motion correction approaches have been added recently in dynamic EPI acquisition scheme to correct linear shims [92] and to allow further accurate motion tracking [93-96]. During the scan time, the measurement coordinate system with a fixed orientation relative to the subject's head is kept to prevent a change in local spin history of magnetization when the head is moved [93]. Combined with retrospective motion correction, which eliminates residual image registration errors, the methods enable optimal real-time motion correction.

Combined with such real-time motion correction, the PSF mapping-based distortion correction scheme may allow optimal dynamic distortion correction during the

measurement time. If the imaging FOV is maintained with the real-time motion correction approach during the scan time, a static EPI-based shift map obtained by the PSF mapping method can be used to robustly calculate field variations of dynamic EPI series at each position. Therefore, a combined approach such as this, has the potential for correcting static and dynamic EPI distortions in real-time and should be considered as a subject for future studies.

BIBLIOGRAPHY

1. Hoffmann MB, Stadler J, Kanowski M, Speck O (2009) Retinotopic mapping of the human visual cortex at a magnetic field strength of 7 T. Clin Neurophysiol 120(1):108-116
2. Mansfield P (1977) Multi-planar image formation using NMR spin-echoes. J Phys C 10:L5-L58
3. Merboldt KD, Frahm J (2000) Reducing inhomogeneity artifacts in functional MRI of human brain activation--thin sections vs gradient compensation. J Magn Reson 145(2):184-191
4. Weiskopf N, Hutton C, Josephs O, Deichmann R (2006) Optimal EPI parameters for reduction of susceptibility-induced BOLD sensitivity losses: a whole-brain analysis at 3 T and 1.5 T. Neuroimage 33(2):493-504
5. Sodickson DK, Manning WJ (1997) Simultaneous acquisition of spatial harmonics (SMASH): fast imaging with radiofrequency coil arrays. Magn Reson Med 38(4):591-603
6. Pruessmann KP, Weiger M, Scheidegger MB, Boesiger P (1999) SENSE: sensitivity encoding for fast MRI. Magn Reson Med 42(5):952-962
7. Griswold MA, Jakob PM, Heidemann RM, Nittka M, Jellus V, Wang J, Kiefer B, Haase A (2002) Generalized autocalibrating partially parallel acquisitions (GRAPPA). Magn Reson Med 47(6):1202-1210
8. Reese TG, Davis TL, Weisskoff RM (1995) Automated shimming at 1.5 t using echo-planar image frequency maps. J Magn Reson Imaging 5(6):739-745
9. Kim DH, Adalsteinsson E, Glover GH, Spielman DM (2002) Regularized higher-order in vivo shimming. Magn Reson Med 48(4):715-722
10. Klassen LM, Menon RS (2004) Robust automated shimming technique using arbitrary mapping acquisition parameters (RASTAMAP). Magn Reson Med 51(5):881-887
11. Shen J, Rycyna RE, Rothman DL (1997) Improvements on an in vivo automatic shimming method (FASTERMAP). Magn Reson Med 38(5):834-839
12. Hennig J, Speck O (2011) High-Field MR Imaging. Springer
13. Jezzard P, Balaban RS (1995) Correction for geometric distortion in echo planar images from B0 field variations. Magn Reson Med 34(1):65-73
14. Weisskoff R, Davis T (1992) Correcting gross distortion on echo planar images. Proc Intl Soc Mag Reson Med 11
15. Reber PJ, Wong EC, Buxton RB, Frank LR (1998) Correction of off resonance-related distortion in echo-planar imaging using EPI-based field maps. Magn Reson Med 39(2):328-330
16. Hutton C, Bork A, Josephs O, Deichmann R, Ashburner J, Turner R (2002) Image distortion correction in fMRI: a quantitative evaluation. Neuroimage 16(1):217-240
17. Xiang QS, Ye FQ (2007) Correction for geometric distortion and N/2 ghosting in EPI by phase labeling for additional coordinate encoding (PLACE). Magn Reson Med 57(4):731-741
18. Wan X, Gullberg GT, Parker DL, Zeng GL (1997) Reduction of geometric and intensity distortions in echo-planar imaging using a multireference scan. Magn Reson Med 37(6):932-942

19. Chen NK, Wyrwicz AM (1999) Correction for EPI distortions using multi-echo gradient-echo imaging. Magn Reson Med 41(6):1206-1213
20. Chen NK, Wyrwicz AM (2001) Optimized distortion correction technique for echo planar imaging. Magn Reson Med 45(3):525-528
21. Zeng H, Gatenby JC, Zhao Y, Gore JC (2004) New approach for correcting distortions in echo planar imaging. Magn Reson Med 52(6):1373-1378
22. Robson MD, Gore JC, Constable RT (1997) Measurement of the point spread function in MRI using constant time imaging. Magn Reson Med 38(5):733-740
23. Zeng H, Constable RT (2002) Image distortion correction in EPI: comparison of field mapping with point spread function mapping. Magn Reson Med 48(1):137-146
24. Zaitsev M, Hennig J, Speck O (2004) PSF mapping with parallel imaging with high accelerations factors: fast, robust and flexible method for EPI distortion correction. Proc Intl Soc Mag Reson Med 12
25. Zaitsev M, Hennig J, Speck O (2004) Point spread function mapping with parallel imaging techniques and high acceleration factors: Fast, robust, and flexible method for echo planar imaging distortion correction. Magn Reson Med 52(5):1156-1166
26. Stevick JW, Harding SG, Paquet U, Ansorge RE, Carpenter TA, Williams GB (2008) Gaussian process modeling for image distortion correction in echo planar imaging. Magn Reson Med 59(3):598-606
27. Hsu YC, Hsu CH, Tseng WYI (2009) Correction for susceptibility-induced distortion in echo-planar imaging using field maps and model-based point spread function. IEEE Trans Med Imag 28(11):1850-1857
28. Paul D, Zaitsev M, Harsan L, Kurutsch A, Splitthoff DN, Hennel F, Choli M, Von Elverfeldt D (2009) Implementation and application of PSF-based EPI distortion correction to high field animal imaging. Int J Biomed Imaging:27
29. Ljunggren S (1983) A simple graphical representation of Fourier-based imaging methods. J Magn Reson 54(2):338-343
30. Bracewell RN (ed) (1978) The Fourier transform and its applications, 2nd edn. MaGraw-Hill, New York
31. Twieg DB (1983) The k-trajectory formulation of the NMR imaging process with applications in analysis and synthesis of imaging methods. Med Phys 10:610-621
32. King KF, Moran PR (1984) A unified description of NMR imaging, data-collection strategies, and reconstruction. Med Phys 11:1-14
33. Schmitt F, Stehling MK, Turner R (1998) Echo-planar imaging: theory, technique and application. Springer
34. Noll DC, Fessler JA, Sutton BP (2005) Conjugate phase MRI reconstruction with spatially variant sample density correction. IEEE Trans Med Imag 24(3):325-336
35. Stehling MK, Turner R, Mansfield P (1991) Echo-planar imaging: magnetic resonance imaging in a fraction of a second. Science 254(5028):43
36. Turner R, Le Bihan D, Scott Chesnicks A (1991) Echo-planar imaging of diffusion and perfusion. Magn Reson Med 19(2):247-253
37. Windischberger C, Robinson S, Rauscher A, Barth M, Moser E (2004) Robust field map generation using a triple-echo acquisition. Magn Reson Med 20(4):730-734
38. Cusack R, Brett M, Osswald K (2003) An evaluation of the use of magnetic field maps to undistort echo-planar images. Neuroimage 18(1):127-142
39. Valkovic L, Windischberger C (2010) Method for geometric distortion correction in fMRI based on three echo planar phase images. Measurement Science Review 10(4):116-119

40. Morgan PS, Bowtell RW, McIntyre DJO, Worthington BS (2004) Correction of spatial distortion in EPI due to inhomogeneous static magnetic fields using the reversed gradient method. J Magn Reson Imaging 19(4):499-507
41. Chang H, Fitzpatrick JM (1992) A technique for accurate magnetic resonance imaging in the presence of field inhomogeneities. IEEE Trans Med Imag 11(3):319-329
42. Meara SJP, Embleton KV, Parker GJM (2008) Distortion correction for a double inversion-recovery sequence with an echo-planar imaging readout. Magn Reson Imaging 26(7):943-953
43. Edelstein WA, Hutchison JMS, Johnson G, Redpath TW (1980) Spin wrap NMR imaging and applications to human whole body imaging. Phys Med Biol 25:751-756
44. Speck O, Stadler J, Zaitsev M (2008) High resolution single-shot EPI at 7T. Magn Reson Mater Phy 21(1):73-86
45. In MH, Speck O (2011) Improved PSF mapping acceleration technique for EPI geometric distortion correction at 7 Tesla. Proc Intl Soc Mag Reson Med 19
46. Ahn CB, Cho ZH (1987) A new phase correction method in NMR imaging based on autocorrelation and histogram analysis. IEEE Trans Med Imag 6(1):32-36
47. Unser M, Aldroubi A, Eden M (1993) B-spline signal processing: part I theory. IEEE Trans Med Imag 41(2):821–833
48. Unser M, Aldroubi A, Eden M (1993) B-spline signal processing. II. Efficiency design and applications. IEEE Trans Med Imag 41(2):834-848
49. Brett M, Johnsrude IS, Owen AM (1996) The problem of functional localization in the human brain. Dementia 383:707-710
50. Ashburner J, Friston K (1997) Multimodal image coregistration and partitioning--a unified framework. Neuroimage 6(3):209-217
51. Brett M, Johnsrude I, Owen A (2002) The problem of functional localization in the human brain. Nat Rev Neurosci 3(3):243
52. Toga AW, Thompson PM, Mori S, Amunts K, Zilles K (2006) Towards multimodal atlases of the human brain. Nat Rev Neurosci 7(12):952-966
53. Chung JY, In MH, Oh SH, Zaitsev M, Speck O, Cho ZH (2011) An improved PSF mapping method for EPI distortion correction in human brain at ultra high field (7.0 T) Magn Reson Mater Phy 24(3):179-190
54. Georgy BA, Hesselink JR (1994) MR imaging of the spine: recent advances in pulse sequences and special techniques. AJR AM J Roentgenol 162(4):923-934
55. Enzmann D, Pelc N (1991) Normal flow patterns of intracranial and spinal cerebrospinal fluid defined with phase-contrast cine MR imaging. Radiology 178(2):467-474
56. Levy L, Chiro G (1990) MR phase imaging and cerebrospinal fluid flow in the head and spine. Neuroradiology 32(5):399-406
57. Nitz W, Bradley W, Watanabe A, Lee R, Burgoyne B, O'Sullivan R, Herbst M (1992) Flow dynamics of cerebrospinal fluid: assessment with phase-contrast velocity MR imaging performed with retrospective cardiac gating. Radiology 183(2):395-405
58. Hu X, Parrish T (1994) Reduction of field of view for dynamic imaging. Magn Reson Med 31(6):691-694
59. Deichmann R, Gottfried J, Hutton C, Turner R (2003) Optimized EPI for fMRI studies of the orbitofrontal cortex. Neuroimage 19(2):430-441
60. Weiskopf N, Hutton C, Josephs O, Turner R, Deichmann R (2007) Optimized EPI for fMRI studies of the orbitofrontal cortex: compensation of susceptibility-induced gradients in the readout direction. Magn Reson Mater Phy 20(1):39-49

61. Oh S-H, Chung J-Y, In M-H, Zaitsev M, Kim Y-B, Speck O, Cho Z-H (2011) Distortion correction in EPI at ultra-high-field MRI using PSF mapping with optimal combination of shift detection dimension. Magn Reson Med DOI:10.1002/mrm.23317
62. In MH, Speck O (2011) Highly accelerated PSF-mapping for EPI distortion correction with improved fidelity Magn Reson Mater Phy DOI: 10.1007/s10334-011-0275-6
63. Greengard L, Lee JY (2004) Accelerating the nonuniform fast Fourier transform. SIAM review 46(3):443-454
64. Ferrara M, Nachman A (2009) www.mathworks.com/matlabcentral/fileexchange/25135-nufft-nfft-usff.
65. Jenkinson M (2003) Fast, automated, N-dimensional phase-unwrapping algorithm. Magn Reson Med 49(1):193-197
66. Hedley M, Rosenfeld D (1992) A new two-dimensional phase unwrapping algorithm for MRI images. Magn Reson Med 24(1):177-181
67. Liang ZP (1996) A model-based method for phase unwrapping. IEEE Trans Med Imag 15(6):893-897
68. Cusack R, Papadakis N (2002) New robust 3-D phase unwrapping algorithms: application to magnetic field mapping and undistorting echoplanar Images. Neuroimage 16(3):754-764
69. Jezzard P, Barnett AS, Pierpaoli C (1998) Characterization of and correction for eddy current artifacts in echo planar diffusion imaging. Magn Reson Med 39(5):801-812
70. Chen B, Guo H, Song AW (2006) Correction for direction-dependent distortions in diffusion tensor imaging using matched magnetic field maps. Neuroimage 30(1):121-129
71. Truong TK, Chen B, Song AW (2008) Integrated SENSE DTI with correction of susceptibility-and eddy current-induced geometric distortions. Neuroimage 40(1):53-58
72. Andersson JL, Skare S (2003) Distortions in diffusion tensor imaging (DTI): putting it all together. Proc Intl Soc Mag Reson Med 11
73. Embleton KV, Haroon HA, Morris DM, Ralph MAL, Parker GJM (2010) Distortion correction for diffusion weighted MRI tractography and fMRI in the temporal lobes. Hum Brain Mapp 31(10):1570-1587
74. Gallichan D, Andersson JLR, Jenkinson M, Robson MD, Miller KL (2010) Reducing distortions in diffusion weighted echo planar imaging with a dual echo blip reversed sequence. Magn Reson Med 64(2):382-390
75. Bodammer N, Kaufmann J, Kanowski M, Tempelmann C (2004) Eddy current correction in diffusion-weighted imaging using pairs of images acquired with opposite diffusion gradient polarity. Magn Reson Med 51(1):188-193
76. Bastin ME (1999) Correction of eddy current-induced artefacts in diffusion tensor imaging using iterative cross-correlation. Magn Reson Imaging 17(7):1011-1024
77. Rohde GK, Barnett AS, Basser PJ, Marenco S, Pierpaoli C (2004) Comprehensive approach for correction of motion and distortion in diffusion-weighted MRI. Magn Reson Med 51(1):103-114
78. Zhuang J, Hrabe J, Kangarlu A, Xu D, Bansal R, Branch CA, Peterson BS (2006) Correction of eddy current distortions in diffusion tensor images using the known directions and strengths of diffusion gradients. Magn Reson Imaging 24(5):1188-1193
79. Bammer SSR (2010) Jacobian weighting of distortion corrected EPI data Proc Intl Soc Mag Reson Med 18
80. In MH, Speck O (2011) Geometric distortion correction of DTI using accelerated PSF mapping based reconstruction at 7 Tesla. Proc Intl Soc Mag Reson Med 19

81. de Moortele V, Pfeuffer J, Glover GH, Ugurbil K, Hu X (2002) Respiration-induced B0 fluctuations and their spatial distribution in the human brain at 7 Tesla. Magn Reson Med 47(5):888-895
82. Barry RL, Menon RS (2005) Modeling and suppression of respiration-related physiological noise in echo-planar functional magnetic resonance imaging using global and one-dimensional navigator echo correction. Magn Reson Med 54(2):411-418
83. Hahn AD, Nencka AS, Rowe DB (2009) Improving robustness and reliability of phase-sensitive fMRI analysis using temporal off-resonance alignment of single-echo timeseries (TOAST). Neuroimage 44(3):742-752
84. Hajnal JV, Myers R, Oatridge A, Schwieso JE, Young IR, Bydder GM (1994) Artifacts due to stimulus correlated motion in functional imaging of the brain. Magn Reson Med 31(3):283-291
85. Friston KJ, Williams S, Howard R, Frackowiak RSJ, Turner R (1996) Movement-related effects in fMRI time-series. Magn Reson Med 35(3):346-355
86. Jezzard P, Clare S (1999) Sources of distortion in functional MRI data. Hum Brain Mapp 8(2-3):80-85
87. Splitthoff D, Testud F, Hennig J, Speck O, Zaitsev M (2007) Real-time prospective shim correction using self-referencing navigators. Proc Intl Soc Mag Reson Med 15:985
88. Kim SG, Hu X, Adriany G, Uğurbil K (1996) Fast interleaved echo-planar imaging with navigator: High resolution anatomic and functional images at 4 tesla. Magn Reson Med 35(6):895-902
89. Liu HL, Kochunov P, Lancaster JL, Fox PT, Gao JH (2001) Comparison of navigator echo and centroid corrections of image displacement induced by static magnetic field drift on echo planar functional MRI. J Magn Reson Imaging 13(2):308-312
90. Hu X, Kim SG (1994) Reduction of signal fluctuation in functional MRI using navigator echoes. Magn Reson Med 31(5):495-503
91. Lamberton F, Delcroix N, Grenier D, Mazoyer B, Joliot M (2007) A new EPI-based dynamic field mapping method: Application to retrospective geometrical distortion corrections. J Magn Reson Imaging 26(3):747-755
92. Ward HA, Riederer SJ, Jack Jr CR (2002) Real-time autoshimming for echo planar timecourse imaging. Magn Reson Med 48(5):771-780
93. Thesen S, Heid O, Mueller E, Schad LR (2000) Prospective acquisition correction for head motion with image-based tracking for real-time fMRI. Magn Reson Med 44(3):457-465
94. Zaitsev M, Dold C, Sakas G, Hennig J, Speck O (2006) Magnetic resonance imaging of freely moving objects: prospective real-time motion correction using an external optical motion tracking system. Neuroimage 31(3):1038-1050
95. Speck O, Hennig J, Zaitsev M (2006) Prospective real-time slice-by-slice motion correction for fMRI in freely moving subjects. Magn Reson Mater Phy 19(2):55-61
96. White N, Roddey C, Shankaranarayanan A, Han E, Rettmann D, Santos J, Kuperman J, Dale A (2010) PROMO: Real-time prospective motion correction in MRI using image-based tracking. Magn Reson Med 63(1):91-105

OWN PUBLICATIONS

Journal Articles

1. **MH In**, O Speck (2011) Highly accelerated PSF-mapping for EPI distortion correction with improved fidelity", Magn Reson Mater Phy, DOI: 10.1007/s10334-011-0275-6 (E-pub)
2. JY Chung, **MH In** (**co-first**), SH Oh, M Zaitsev, ZH Cho, O Speck (2011) An improved PSF mapping method for EPI distortion correction in human brain at ultra high field (7T). Magn Reson Mater Phy vol. 24(3) pp. 179-190
3. SH Oh, JY Chung, **MH In** , M Zaitsev, O Speck, ZH Cho (2011) Distortion correction in EPI at ultra high field MRI using PSF mapping with optimal combination of shift detection dimension. Mag Reson Med, DOI: 10.1002/mrm.23317 (E-pub)
4. SH Ahn, WH Lee, **MH In**, T-S Kim, SY Lee (2007) Extraction and localization of alpha activity of the brain in EEG and fMRI using constrained ICA. IEEE EMBS, pp. 5493-5496
5. **MH In**, SY Lee, TS Park, T-S Kim, MH Cho, YB Ahn (2006) Ballistocardiogram artifact removal from EEG signals using adaptive filtering of EOG signals. Physiol Meas, vol. 27, pp. 1227-1240
6. T Rasheed, **MH In**, Y-K Lee, SY Lee, SY Lee, T-S Kim, (2006) Constrained ICA based ballistocardiogram and electro-oculogram artifacts removal from visual evoked potential EEG signals measured Inside MRI. LNCS, vol. 4232, pp. 1088-1097

International Conferences

1. **MH In**, O Speck (2011) Highly accelerated PSF-mapping for EPI distortion correction with improved fidelity. 28th scientific meeting of ESMRMB, Leipzig, Germany (Oral)
2. F Godenschweger, **MH In**, O Speck (2011) Distortion correction for slice multiplexed EPI (CAIPIRINHA) at 7 Tesla. 28th scientific meeting of ESMRMB, Leipzig, Germany (Oral)
3. **MH In**, O Speck (2011) Improved PSF mapping acceleration technique for EPI geometric distortion correction at 7 Tesla. 19th scientific meeting of ISMRM, Montréal, Canada (e-Poster)
4. **MH In**, O Speck (2011) Geometric distortion correction of DTI using accelerated PSF mapping based reconstruction at 7 Tesla. 19th scientific meeting of ISMRM, Montréal, Canada (e-Poster)
5. SH Oh, JY Chung, **MH In**, M Zaitsev, O Speck, YB Kim, ZH Cho (2011) A novel correction method for distortion correction in EPI at ultra high field MRI using PSF mapping technique. 19th scientific meeting of ISMRM, Montréal, Canada (Poster)

6. SH Oh, JY Chung, SY Park, JH Park, DH Kang, **MH In**, M Zaitsev, O Speck, YB Kim, ZH Cho (2011) Distortion free high resolution in vivo whole brain diffusion tensor image on 7.0T MRI. 19th scientific meeting of ISMRM, Montréal, Canada (Poster)
7. SH Oh, JY Chung, SY Park, **MH In**, M Zaitsev, O Speck, HW Yoon, DS Kim, YB Kim, ZH Cho (2010) Distortion free in-vivo human whole brain DTI using combined dimensional PSF mapping method on 7T. 16th annual meeting of HBM, Barcelona, Spain (Poster)
8. SH Oh, JY Chung, **MH In**, M Zaitsev, O Speck, HW Kim, YB Kim, ZH Cho (2010) New calculation method of pixel shift map on PSF mapping technique: a study on 7T MRI. 16th annual meeting of HBM, Barcelona, Spain (Poster)
9. **MH In**, JY Chung, M Zaitsev, ZH Cho, O Speck (2010) Improved PSF-based EPI distortion correction in human imaging at 7 Tesla. The joint scientific meeting of ISMRM-ESMRMB, Stockholm, Sweden (e-Poster)
10. F Godenschweger, **MH In**, O Speck (2010) Robust method for EPI ghost correction. The joint scientific meeting of ISMRM-ESMRMB, Stockholm, Sweden (e-Poster)
11. SH Oh, JY Chung, **MH In**, M Zaitsev, O Speck, YB Kim, ZH Cho (2010) New calculation method of pixel shift map on PSF mapping technique: a study on 7T MRI. The joint scientific meeting of ISMRM-ESMRMB, Stockholm, Sweden (e-Poster)
12. SH Oh, JY Chung, SY Park, DS Kim, **MH In**, M Zaitsev, O Speck, YB Kim, ZH Cho (2010) Distortion correction method for single echo DTI at 7T MRI using non-distortion and distortion dimension combined PSF mapping technique. The joint scientific meeting of ISMRM-ESMRMB, Stockholm, Sweden (Poster)
13. **MH In**, JY Chung, ZH Cho, O Speck (2009) Improved PSF-based EPI distortion correction at 7 Tesla. 26th scientific meeting of ESMRMB, Antalya, Turkey (Poster)
14. **MH In**, HJ Kim, TS Park, T-S Kim, MH Cho, SY Lee, "Ballistocardiogram artifact removal from EEG signals using the real-time Kalman filter", 15th scientific meeting of ISMRM, Toronto, Canada, 2007 (Poster)
15. **MH In**, SY Lee, MH Cho, BH Han, T-S Kim, JY Han, "Simultaneous fMRI and EEG source localization with visual motion stimuli", 14th scientific meeting of ISMRM, Seattle, USA, 2006 (Poster)
16. T Rasheed, T-S Kim, Y-K Lee, **MH In**, WH Lee, SY Lee, "Constrained ICA-based ballistocardiogram and electro-oculogram artifacts removal from EEG signals acquired inside MRI", 14th scientific meeting of ISMRM, Seattle, USA, 2006 (Poster)
17. **MH In**, BH Han, JY Han, T-S Kim, MH Cho, SY Lee, "Spatiotemporal source mapping on visual motion via simultaneous fMRI-EEG", 12th annual meeting HBM, Florence, Italy, 2006 (Poster)
18. **MH In**, SY Lee, MH Cho, T-S Kim, BH Han, JY Han, "Brain source analysis of visual motion stimulus with simultaneous fMRI-EEG", WC2006, Seoul, Korea, 2006 (Poster)

ACKNOWLEDGMENTS

I wish to express my thanks to the many people who have helped and inspired me during my doctoral studies.

I especially wish to express my sincere appreciation to my supervisor, Prof. Dr. Oliver Speck, head of the Department of Biomedical Magnetic Resonance (BMMR), Otto-von-Guericke University of Magdeburg, for his excellent guidance, caring, patience, friendship, and wisdom. He provided me with an excellent atmosphere, encouragement, inspiration, and motivation for doing research and enabled me to complete this research work smoothly and successfully.

I also wish to express my deep appreciation to Prof. Dr. Zang-Hee Cho and Dr. Jun-Young Chung at the Neuroscience Research Institute (NRI), Gachon University of Medicine and Sciences, Korea. I had the honor to serve as Prof. Cho's research assistant at NRI, and Dr. Jung provided guidance and advice during that period.

In addition, special thanks to Dr. Frank Godenschweger for his valuable advice and generous help. My extensive discussions with him about my work were very helpful for this study. Thanks also to our BMMR team members for their valuable input in research and life through our interactions during the long hours in the lab.

I am very grateful to my parents, younger brother, older sister, and parents in law. They were always supporting and encouraging me with their best wishes.

Last but not least, I am greatly indebted to my devoted wife Hyemi and my son Sunghwan. Their love and support without any complaints or regrets have allowed me complete this doctoral study.

Magdeburg, Germany Myung-Ho In
June 2012

ERKLÄRUNG

Hiermit erkläre ich, dass ich die von mir eingereichte Dissertation zum dem Thema

“Geometric Distortion Correction in EPI at Ultra High Field”

selbständig verfasst, nicht schon als Dissertation verwendet habe und die benutzten Hilfsmittel und Quellen vollständig angegeben wurden.

Weiterhin erkläre ich, dass ich weder diese noch eine andere Arbeit zur Erlangung des akademischen Grades doctor rerum naturalium (Dr. rer. nat.) an einer anderen Einrichtungen eingereicht habe.

Magdeburg, June 2012 Myung-Ho In